Trapping of 1 μ_B atoms using buffer gas loading

A dissertation presented
by

Nathaniel Charles Brahms

to
The Department of Physics
in partial fulfillment of the requirements
for the degree of
Doctor of Philosophy
in the subject of

Physics

Harvard University
Cambridge, Massachusetts
May 2008

Thesis advisor

Professor John Morrissey Doyle

Author

Nathaniel Charles Brahms

Trapping of 1 μ_B atoms using buffer gas loading

Abstract

Buffer gas cooling is applied to load magnetic traps with atoms having a 1 μ_B magnetic dipole moment. Large numbers, up to 4×10^{13}, of lithium, copper, and silver, are trapped with lifetimes as long as 200 s. For lithium, the buffer gas can be removed from the trap, leaving a background gas density of $\sim 10^{11}$ cm^{-3}. Further improvements are suggested that could be used to reduce this number far enough to achieve thermal isolation of the trapped atoms. The collisional properties of copper and silver with helium-3 are studied. An anomalous temperature dependence for the relaxation cross-section is discovered in the silver–helium-3 system. This is compared to a theoretical prediction based on the canonical spin-rotation interaction. The measurement and theory disagree, suggesting that the relaxation is due to a typically neglected mechanism.

Contents

List of Figures

List of Tables

Citations to Previously Published Work

Portions of Chap. 3 were published in R. deCarvalho, N. Brahms, B. Newman, J. M. Doyle, D. Kleppner, and T. Greytak, "A New Path to Ultracold Hydrogen", Can. J. Phys., **83** 293 (2005) [1].

Portions of Chap. 4 have been submitted for publication. This publication is available as N. Brahms, B. Newman, C. Johnson, T. Greytak, D. Kleppner, and J. Doyle, "Magnetic trapping of silver and copper and anomolous spin relaxation in the Ag-He system", arXiv:0804.0766v1, submitted to Phys. Rev. Lett. [2].

In §C.1, the spin-rotation interaction is calculated according to the method given by Walker, Thywissen, and Happer in [3]. This section includes a recapitulation of that method.

Acknowledgments

This experiment was a collaborative effort, and none of this work would have been possible without the hard work of my labmates. Bonna Newman and Cort Johnson have worked with me almost since I first started on the experiment. We have shared in every aspect of the experiment — from late nights taking data, to hours at the whiteboard designing the apparatus, to fixing broken pumps arm-deep in oil, to finally finding the right parameters for seeing trapped atoms. The results presented here are equally their accomplishment. It was my pleasure to work with Rob deCarvalho on the experiment, and he served as a great role model for me during my graduate school career. Our styles of thought complemented each other perfectly, and much of my understanding of the physics involved in these experiments, much of it presented in this thesis, is due to conversations with Rob. Furthermore, Rob's positive attitude was a boon whenever our experiment refused to work. Chih-Hao Li was a postdoc on our experiment and a great joy to work with. In addition to helping in operating and designing the experiment, Chih-Hao was always there to answer any question one might have with atomic physics.

Graduate school is more than just learning some physics and running an experiment. My advisor, John Doyle, has certainly taught me a great deal in these areas, but also much more: how to present ideas, how to be a professional physicist, and how to simply get things done. John has made his group a family, and I have gained not only outstanding colleagues, but good friends, by joining his group.

I have also had the pleasure and fortune to work with Profs. Tom Greytak and Daniel Kleppner, two additional PIs on the experiment. Tom has a knack for asking the probing question that can help solve a problem. He has often generously invited us to relax at his retreat in New Hampshire, helping to keep graduate school enjoyable. Dan has an incredible knowledge of atomic physics, even including its 18th Century history, and he is always willing to share this knowledge, in a clear and pedagogical manner. Dan is truly a kind man, and his suggestions and his encouragement have been indispensable.

I am grateful to Kate Kirby, Jim Babb, Alex Dalgarno, and Hossein Sadeghpour of the Harvard/Smithsonian CFA, and Roman Krems of UBC, for many productive discussions in helping me to understand the spin-rotation process and how to calculate it.

Thanks are due to the administrative staffs at Harvard Physics and the RLE at MIT, without whom we'd have an empty lab. I am especially grateful to Vickie Greene, Sheila Ferguson, and Stan Cotreau. The members of John Doyle's group have helped in innumerable ways throughout the years. Special thanks go to Steve, Colin, Wes, Charlie and Matt.

And finally, I am eternally grateful to my wife, Courtney. Her love, patience, and support have been a constant comfort while writing this thesis.

To my mother

Chapter 1

Introduction

The first magnetic trapping of neutral atoms occurred nearly 23 years ago [4–6]. Since then, the trapping of neutral atoms has allowed for a revolution in atomic physics, making possible the observation of novel states of matter, including quantum degeneracy [7–10] and superfluidity [11] of dilute atomic and molecular [12, 13] gases, and the realization of quantum gas insulators [14, 15]. Ultracold samples of trapped atoms could allow for more precise measurements [5], leading, for example, to better optical clocks [16]. Trapped atoms can also show very strong interactions with light, resulting in very large refractive group indices [17] and the ability to store quantum information [18, 19].

Despite the incredible number of advances bestowed by the advent of atom trapping, only a small subset of magnetic species has thus far been trapped. Because magnetic traps are shallow, with the deepest trap depths only a few K [20], a significant degree of cooling must be performed to load magnetic traps. Cooling these species in a trappable internal state, while maintaining their dilute gas phase, poses a serious experimental challenge. With some notable exceptions [9, 21, 22], trapping experiments have used laser cooling [23–25] of thermal beams. In order to be successful, laser cooling requires a "closed"

cooling cycle: After absorbing a photon from the cooling laser, the atom must decay to its original trapped state. If the atom can decay to some other state after absorbing the cooling photon, an additional laser must be added to "repump" the atom back into the trapping state. For simple atoms (notably the alkali metals) these concerns are minimal. For atoms with more complex atomic structure, or for molecules, with their rotational and vibrational manifolds, the technical challenges associated with these extra states multiply [26]. In addition, because high laser powers are required for the cooling and repump beams, laser cooling is generally limited to species with strong cooling transitions at visible wavelengths. Finally, because atoms typically begin as thermal beams, the technique is most successful with species with significant vapor pressures at temperatures between 0 °C and a few hundred °C. Laser cooling, therefore, has been restricted to atoms, and to a few specialized groups of atoms at that. The alkali atoms have been most extensively studied, and have been laser cooled and trapped in their ground state. The alkali earths and the noble gases are also amenable to laser cooling; however, they experience no magnetic interaction in their ground state, and can therefore only be trapped in metastable excited states. With specialized effort, laser cooling has also been used to cool and trap neutral chromium, silver, erbium, and ytterbium (in magneto-optical traps).

While a large and important body of work can and has been pursued with laser cooling, there is a natural desire to pursue alternate cooling strategies for the loading of magnetic traps. Such pursuits seek both to extend the class of species that can be trapped, and to increase the density of atoms or molecules in the trapped clouds. This thesis is concerned with buffer gas cooling [21, 27], one of these alternate strategies. Buffer gas cooling has been successful at adding to the list of species trapped in magnetic traps: To date, buffer gas loading of magnetic traps has been demonstrated for 17 atoms and 4 molecules[1]

[1]Including three atoms studied in this thesis work. Note that multiple isotopes have been trapped for

[1, 28–35]. Despite its success, buffer gas cooling, as a method for loading magnetic traps, has generally been restricted to species with strong magnetic field interactions. The work in this thesis seeks to extend buffer gas cooling, as a technique for loading magnetic traps for further evaporative cooling [36], to atoms and molecules with the weakest magnetic field interactions — the 1 μ_B species.

1.1 1 μ_B species

The potential energy of interaction of a magnetic atom or molecule with a magnetic field $\vec{B}$ is

$$U = \vec{\mu} \cdot \vec{B}, \tag{1.1}$$

where $\vec{\mu}$ is the magnetic dipole moment of the atom or molecule. The strength of $\vec{\mu}$ is quoted in terms of the dipole moment of hydrogen, $\mu_B = \frac{q_e \hbar}{2 m_e c}$. Here we are concerned with atoms and molecules whose dipole moment is the same as that of hydrogen — these are the most weakly magnetic species that can be trapped in magnetic traps.

These "1 μ_B" atoms and molecules form an important class of species. They include all atoms having a single valence s electron. These atoms undergo inelastic collisions only very rarely. Since inelastic collisions generally cause atom loss from magnetic traps, this means that these atoms are well suited to magnetic trapping. In particular, the efficiency of evaporative cooling depends on the ratio of the rate of elastic atom-atom collisions to the rate of inelastic atom-atom collisions. If evaporative cooling is to be successful at reducing the temperature of trapped atoms into the nano- or micro-Kelvin regime, this ratio must be very high, on the order of 10^4 or larger. While we would expect atoms with two valence s electrons to also have high elastic-inelastic collision ratios, they have no magnetic interaction

---

many of the atoms and at least one of the molecules (NH).

in their ground state. The double s valence atoms are therefore typically trapped in a spin-triplet 2 μ_B metastable excited state.

1.1.1 Hydrogen and its isotopes

Hydrogen (H) is a 1 μ_B atom worth special mention. It is not amenable to laser cooling because its primary transition is deep in the UV: 122 nm [37]. Because it is such a simple atom, it is an important theoretical test ground. By making precise measurements of the narrow line $1s \rightarrow 2s$ transitions, QED can be tested to high orders [38].

H has previously been cooled and magnetically trapped using a specialized method [39]. In this method, H is cooled to 120 mK by collisions with a ^{4}He film. Because of the unique collisional properties of H with this film, the H does not stick to the film surface — instead the H cools while remaining in its gas phase. This cooling mechanism is, however, only successful with H. The cold film method has been used to load magnetic traps with H as a starting point for evaporative cooling. Because the H-H elastic collision rate is very weak, this evaporative cooling is inefficient. In Chapt. 3, I will discuss how buffer gas cooling can be used to increase the efficiency of H evaporative cooling, by co-trapping an alkali gas for use as a sympathetic cooler.

This unique film cooling method is moreover restricted to the protium isotope (^{1}H) of hydrogen [40]. The ability to trap the hydrogen isotopes deuterium (D) and tritium (T) would open the way to even more experiments. By trapping ^{1}H and D simultaneously, a precise measurement of the hydrogen isotope shift could be taken. This leads to a measurement of nuclear structure: The proton and neutron charge radii, and the deuteron structure radius [41]. Trapping of tritium would allow for a more sensitive measurement of the electron antineutrino rest mass by measure of the endpoint energy of the tritium β-decay spectrum [42].

1.1.2 Noble metals

Like the alkalis, the noble metals copper (Cu), silver (Ag), and gold (Au), are single s valence atoms. These atoms are differentiated by possessing an underlying filled d shell. This filled d shell gives rise to narrow two-photon transitions between the ground S configuration and an excited metastable D configuration (in which one d electron is excited to the s shell). These narrow lines have been proposed as optical frequency standards [43]. In addition, as gold is one of the heaviest atoms, it is an ideal test ground for relativistic atomic theories [44].

Unlike the alkalis, however, the primary transitions are UV, not visible. Because obtaining high laser powers in the UV is difficult, laser cooling of the noble metals faces serious experimental challenges [45]; whereas for buffer gas cooling the large energy spacing between ground and excited states is useful, as it suppresses inelastic losses dependent on S-P mixing.

1.1.3 $^2\Sigma$ molecules

To obtain trapped molecules using laser cooling requires that atoms first be cooled and trapped. While trapped, these atoms are then bound into molecules via a Feshbach resonance [46] or laser-induced photoassociation [47]. After creation, these molecules lie in a highly excited vibrational state, requiring complex optical manipulation to yield trapped ground state molecules. Furthermore, molecules created by this method are restricted to dimers of those species amenable to laser cooling and trapping, i.e., the alkalis.

An alternate approach to trapping molecules is to first produce ground state molecules and then cool them[2] — the approach taken by buffer gas cooling.

[2] At the 300 K to 1000 K temperatures at which these molecules are produced, they will have a significant distribution over rotational states. In buffer gas cooling, the rotational degree of freedom is collisionally cooled to the buffer gas temperature.

$^2\Sigma$ molecules are 1 μ_B molecules, and include the alkaline earth monohydrides and monohalides. They are a molecular analogue to the ^2S single s electron atoms. In their ground state they are predicted to suffer inelastic collisions only rarely [48, §2.3], making them good candidates for evaporative cooling.

1.2 Magnetic trapping

In order to trap atoms or molecules using their magnetic dipole interaction (1.1), we must create a region in (free) space where the interaction energy has a minimum. For species whose dipole moment is aligned with the magnetic field (low-field seekers), this corresponds to creating a region whose magnetic field norm has a minimum. The converse case, when the dipole moment is counteraligned to the magnetic field (high-field seekers), would require a local maximum in the magnetic field. Since a magnetic field maximum can not be created in a source-free region [5], only low-field seekers can be trapped using solely magnetic fields.[3]

The simplest geometry for producing such a magnetic trap is the magnetic quadrupole trap. It is generated using an anti-Helmholtz magnet, consisting of two coils, with the currents in the coils running in opposite directions. Such a magnet, and the field it generates, are shown in Fig. 1.1. The magnetic field strength at a point close to the trap center, with z chosen to be the axis of cylindrical symmetry, is

$$B(r,z) = \frac{\partial B}{\partial r}\sqrt{r^2 + 4z^2}, \tag{1.2}$$

where $\frac{\partial B}{\partial r}$ is a constant depending on the coil currents and geometry. The equipotential surfaces of the magnetic field interaction are ellipsoidal shells.

[3] By using magnetic fields together with a light field, the high-field seeking states can be trapped.

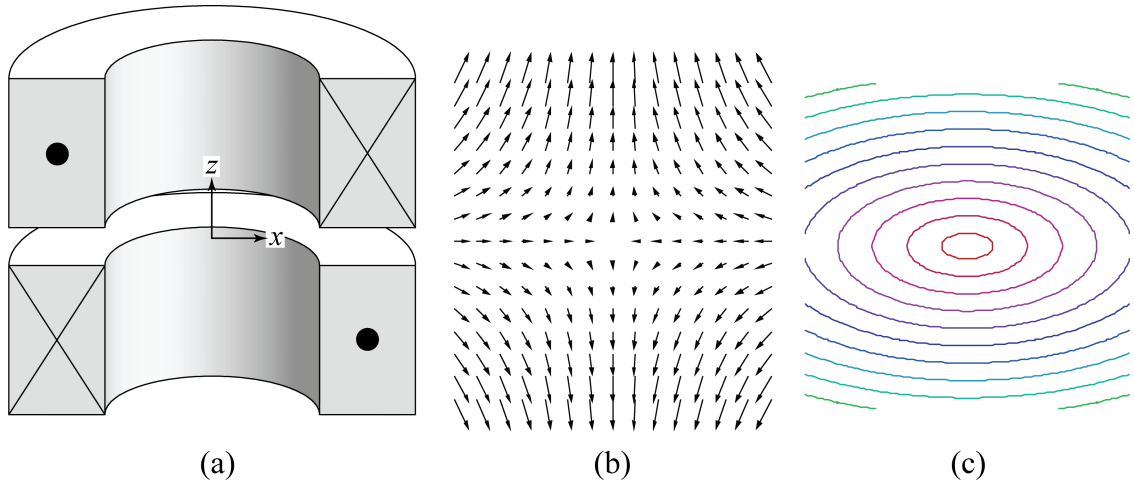

Figure 1.1: A quadrupole trap. (a) shows the anti-Helmholtz coil configuration used, with the circles and crosses indicating the direction of field flow. (b) shows the magnetic field in the x-z plane near the center of the trap. (c) shows the equipotential contours of the magnetic dipole interaction in the x-z plane, near the center of the trap.

Species will remain in this trap as long as their total energy is less than the magnetic field interaction strength at the closest physical surface. This energy is called the "trap depth", U_{trap}. If the average kinetic energy of the trapped gas is large compared to U_{trap}, the species will collide with this physical surface and stick, and thereby be lost from the trap. If the average kinetic energy is small, only those particles at the tail of the Boltzmann distribution will have enough energy to leave the trap, and the great majority of the atoms will remain trapped. It is useful to define a ratio of these two energies:

$$\eta \equiv \frac{U_{\text{trap}}}{k_B T}. \tag{1.3}$$

Then the condition for trapping becomes:

$$\eta \gg 1. \tag{1.4}$$

In Chapt. 2, the η dependence of species' lifetime within the trap will be derived. In general, (1.4) sets a requirement on the cooling method used to load a magnetic trap: the cooling method must cool the species to a temperature well below the trap depth.

1.3 Buffer gas cooling

Whereas laser cooling removes thermal energy from the species by coupling their thermal motion to a low-entropy photon reservoir (the laser), buffer gas cooling operates by coupling them to a low-entropy reservoir of atoms — the buffer gas. In buffer gas cooling this coupling is accomplished by allowing the species to collide elastically with the buffer gas [49]. Each collision, on average[4], removes an energy

$$\overline{dE} = (E_a - E_b)\,\frac{2\,M\,m}{(M+m)^2} \tag{1.5}$$

from the atom or molecule, where E_a and E_b are the species and buffer gas kinetic energies, respectively, and M and m are the species and buffer gas masses, respectively. The species is therefore cooled exponentially to the buffer gas temperature. The species temperature comes to within 100 mK of the buffer gas temperature after 30 to 300 collisions, depending on the species and buffer gas masses. Typically the same volume is used to cool the atoms and trap the atoms. Therefore, once the atoms reach the buffer gas temperature they are trapped.

This minimum number of collisions sets a requirement on the density of buffer gas within the cooling volume. The species must cool before it can reach a wall of the cooling volume (where it sticks); therefore the mean free path for elastic collisions must be 30 to 300 times smaller than the size of the cooling volume [50]. For typical cell sizes on the order of 10 cm and elastic collision cross-sections [51] of 3×10^{-15} cm^2, this sets a minimum buffer gas density of 1×10^{15} to 1×10^{16} cm^{-3}.

Any buffer gas will have a maximum density at any given temperature. The vapor density – temperature curve for some low-temperature gases is shown in Fig. 1.2. To achieve a given density in the cooling volume, the temperature must be raised to a minimum value

[4]The average is over incoming and outgoing collision angles.

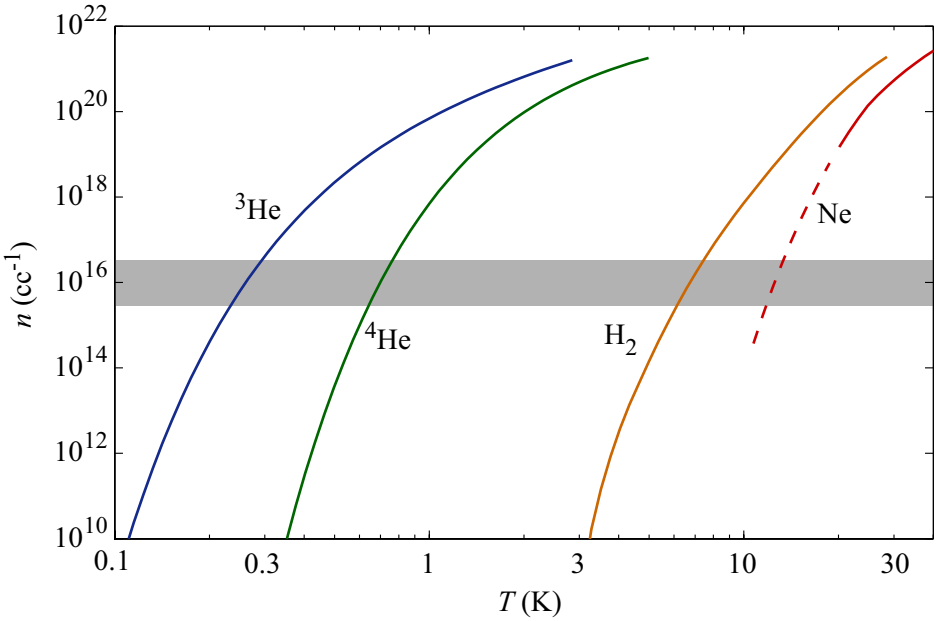

Figure 1.2: Vapor densities of various cryogenic gases [52–54]. The shaded region indicates typical densities used in buffer gas experiments. The H_2 curve is approximate. The dashed portion of the Ne curve is an extrapolation.

— the temperature at which the buffer gas vapor density equals the desired buffer gas density. We use ^{3}He buffer gas to obtain the smallest possible buffer gas temperature, between 200 mK and 300 mK.

In order to cool the species below the buffer gas temperature, we must break the thermal coupling between the species and the buffer gas. Once this is done, evaporative cooling [36] can be attempted, to further cool the species. To break this thermal coupling, we must either "turn off" the elastic collision cross-section, perhaps by manipulating electric and magnetic fields, or we must remove the buffer gas from the trapping volume. Only the latter of these options has been shown to be feasible. This "thermal isolation" of the species from the buffer gas is discussed in depth in §2.3.

1.3.1 Additional advantages of buffer gas cooling

So far we have discussed buffer gas cooling in the context of opening new species to magnetic trapping. There are, however, additional motivations for pursuing buffer gas cooling as a method of trapping 1 μ_B species.

Because a large amount of buffer gas, $\sim 10^{19}$ atoms, is typically used in a buffer gas cooling experiment, a correspondingly large species numbers, up to 10^{14} [55], can be cooled by the buffer gas. Because buffer gas cooling loads species in the few hundred milliKelvin temperature range, the technique is well-suited to studies of cold collisions. Whereas collisional behavior is simple in the classical and ultracold temperature limits, the behavior of collisions and chemical reactions in the cold (100 mK to few K) regime can be very rich, and can lead to new theoretical understanding of atomic and molecular collisions [28, 56].

1.3.2 Buffer gas cooling of 1 μ_B species

Because the minimum temperature achieved by buffer gas cooling is around 250 mK, a very strong magnetic interaction is required for buffer gas cooling. This is much easier to achieve for strongly magnetic atoms. Prior to this thesis two 1 μ_B species, CaH and Na, had been successfully trapped using buffer gas cooling [29, 57, 58]. However, removal of the buffer gas could not be achieved.

In this thesis, I show how 1 μ_B species can be trapped for up to 10 s in the presence of the buffer gas. By minimizing the atom temperature and carefully controlling the buffer gas removal process, the majority of the buffer gas can be removed, leading to observed lifetimes as long as 200 s. In order to achieve true thermal isolation of the trapped species, a remnant quantity of buffer gas must still be removed; suggestions are given for how this may be achieved in a 1 μ_B buffer gas trapping experiment.

In Chapt. 2, a theoretical background for 1 μ_B trapping in buffer gas loaded traps is given. This includes a description of the lifetime of trapped species as a function of trap parameters, including temperature, trap depth, and density of buffer gas. Also included is a discussion of buffer gas removal and thermal isolation.

In Chapt. 3, I discuss buffer gas loading experiments performed with lithium (Li), in which we demonstrated trapping of large samples of Li (up to 10^{13} atoms) at lifetimes up to 200 s after buffer gas removal. Thermal isolation could not be demonstrated.

In Chapt. 4, I discuss experiments performed with the noble metals copper (Cu), silver (Ag), and gold (Au). We were able to trap Cu and Ag with lifetimes up to 8 s. Because of the large amount of heat introduced to the system by our noble metal production method, we were not able to remove the buffer gas. Possible improvements to the experimental apparatus are suggested which may allow for future buffer gas removal in a trapped noble metal experiment. We also studied the collisional properties of Cu and Ag with the ^{3}He buffer gas, discovering an anomalous thermal dependence of the Ag-^{3}He inelastic relaxation rate.

Finally, in Chapt. 5, I discuss future directions for experiments, including improvements that may allow for evaporative cooling to degeneracy or for precision metrology.

Chapter 2

Trapped atom loss and thermal isolation

An understanding of the loss rates of species from magnetic traps is crucial to any trapping experiment. In order for an experiment to succeed, these loss rates must be reduced such that the species remain trapped for the duration of the experiment. Moreover, loss rates are one of the best probes available for measuring physical interactions in the cold and ultracold regimes. To both glean physical information from loss rates and to design experiments such that atoms are trapped for long times, we should understand how various loss processes depend on species density, temperature, and internal states, as well as how they depend on environmental variables such as fields or background gas density and temperature.

Because 1 μ_B atoms are so weakly trapped, loss rates for these atoms can be very high. If we are to obtain a dense sample of thermally isolated 1 μ_B atoms, we must carefully manage the experimental parameters to minimize atom loss during our experiments.

I will enumerate some of the various loss processes that can occur in buffer gas loaded traps, identify the regimes in which they dominate, and examine their dependence

on experimental parameters. I will then discuss how these loss processes affect loading and thermal isolation of 1 μ_B species in buffer gas cooling experiments. I will use the phrase "trapped atom" here to describe the trapped species of interest, even though the loss rates listed here will also occur with trapped molecules. However, trapped molecules may display additional loss processes beyond those occurring in atoms.

2.1 General loss behavior

Loss processes may be categorized based on the number p of trapped atoms involved in one loss event. If loss is caused by trapped atoms colliding with untrapped bodies (photons, background gas, walls, etc.), $p = 1$. If loss is caused by atom-atom collisions $p = 2$, and so forth to higher orders. Each loss process may be described by a local rate equation:

$$\frac{dn(\vec{r})}{dt} = -G_p(\vec{r})\, n^p(\vec{r}). \tag{2.1}$$

Here $n(\vec{r})$ is the local atom density at spatial coordinate $\vec{r}$. G_p is a generalized rate coefficient that describes the frequency of loss for a given n^p. If a set of loss processes are independent, the total local loss can be found by summing the rate equations for each process.[1]

For $p = 1$, we call the loss "1-body" and use Γ to denote G_1. When $p = 2$, we call the loss "2-body" and use g in place of G_2. Without significant evaporative cooling, trap densities in buffer gas cooling experiments will generally be low enough that we may neglect higher order loss processes [59].

To find the dependence of the trapped population versus time, we use (2.1) to obtain an equation for the total atom number:

$$\left.\frac{dN}{dt}\right|_p = -\int G_p(\vec{r})\, n^p(\vec{r}) d^3\vec{r}. \tag{2.2}$$

[1] Notably, diffusive trap loss is *not* independent of background-driven atom evaporation.

If the loss rate coefficients G_p do not depend on $\vec{r}$, and also do not depend on time[2], we can solve this equation generally for any loss order.

To solve (2.2) in general, we must know the $\vec{r}$-dependence of the atom density n. If the atoms remain in thermal equilibrium under the presence of the loss process — that is, atom-atom or atom-background collisions occur more frequently than the atom loss rate, for all $\vec{r}$ — then $n(\vec{r})$ is described by the Maxwell-Boltzmann distribution function:

$$n(\vec{r},t) = n(\vec{0},t)\, e^{-U(\vec{r})/k_B T}, \tag{2.3}$$

$$U(\vec{r}) = \vec{\mu}(B,J,m_J)\cdot \vec{B}(\vec{r}). \tag{2.4}$$

Here $\vec{B}(\vec{r})$ is the local magnetic field and $\vec{\mu}(B,J,m_J)$ is the atom magnetic dipole moment. In general $\vec{\mu}$ is a function of the local magnetic field strength B and the internal state of the atom $|J\, m_J\rangle$. For most atoms $\vec{\mu}$ is a linear function of magnetic field and the projection quantum number m_J. This is true for all but the lightest atoms,[3] as long as the magnetic field is strong enough such that the Zeeman effect dominates over the hyperfine interaction. In this case we have

$$\vec{\mu}(B,J,m_J)\cdot \vec{B}(\vec{r}) = \mu\, B(\vec{r}) = g_J\, m_J\, \mu_B\, B(\vec{r}), \tag{2.5}$$

where g_J is the Landé g-factor [25, p. 42] and μ_B is the Bohr magneton. $B(\vec{r})$ is the local magnetic field strength.

2.1.1 Trap depth

It is convenient to introduce the concept of trap depth. This can be done for any given trapping field, and for any given surface at which trapped atoms are lost from the

[2]We require specifically that the relative time variation of G_p be much slower than the slowest instantaneous relative time variation of N in the time range of interest.

[3]For atoms with atomic number lower than 4 or so, the $\vec{\mathbf{L}}\cdot\vec{\mathbf{S}}$ interaction modifies the magnetic interaction at realistic laboratory fields. For these atoms m_J is not a good quantum number at low field. See App. A.1.

trap. Usually this surface will be the closest cell wall to the trap center. Let $\vec{R}$ be the point on this loss surface at which $U(\vec{r})$ is minimized. Then the trap depth $U_{\text{trap}} \equiv U(\vec{R})$.

We will also find it useful to define a dimensionless parameter η:

$$\eta \equiv \frac{U_{\text{trap}}}{k_B T}, \tag{2.6}$$

where T is the temperature of the atom cloud.

2.1.2 Atom distributions and effective volumes

We have shown, assuming the trapped atoms remain in thermal equilibrium and the Zeeman interaction is linear in magnetic field, that the atoms obey the Maxwell-Boltzmann distribution function:

$$n(\vec{r}, t) = n_0(t) e^{-\mu B(\vec{r})/k_B T}. \tag{2.7}$$

Depending on the magnetic trap and the form of the loss surface, this distribution will have a different dependence on $\vec{r}$. Distributions for some traps and loss surfaces frequently encountered in buffer gas trapping are tabulated in Table 2.1.

In order to calculate $N(t)$ from (2.2), we need to integrate powers of n over all $\vec{r}$. We define a quantity V_p, which is a function depending on the trap, loss surface, and trap depth. It is called the (p-body) effective volume.

$$\int n^p(\vec{r})\, d^3\vec{r} \equiv n_0^p\, V_p(\vec{R}, \eta). \tag{2.8}$$

V_p for various traps and loss surfaces, in the limit of large η, are tabulated along with the atom distributions in Table 2.1.

The 1-body effective volume can be used to relate the total atom number N to the peak density n_0:

$$N = n_0 V_1(\vec{R}, \eta). \tag{2.9}$$

Atom distributions and effective volumes			
Trap	Loss surface	$n(\vec{r})/n_0$	V_p
Spherical harmonic	Spherical shell	$e^{-\eta\, r^2/R^2}$	$\sqrt{\frac{\pi^3}{p^3\eta^3}}\, R^3$
Spherical quadrupole	Spherical shell	$e^{-\eta\, r/R}$	$\frac{8\pi R^3}{p^3\eta^3}$
Ellipsoidal quadrupole	Cylindrical radius	$e^{-\eta\sqrt{r^2+4z^2}/R}$	$\frac{4\pi R^3}{p^3\eta^3}$
Ellipsoidal quadrupole	1 axial surface	$e^{-\eta\sqrt{r^2/4+z^2}/L}$	$\frac{32\pi L^3}{p^3\eta^3}$

Table 2.1: $n(\vec{r})$ is the atomic distribution function. V_p is the effective volume for a p-order loss process. Large η is assumed in all expressions for V_p. Note that η as used here is defined using the minimum trap depth at the loss surface. R is the cell radius and L is the distance from the trap center to the closest axial surface.

Armed with the atomic distribution function and effective volume, we can now solve the loss equation (2.2) for $N(t)$ for all loss orders, when G_p is independent of $\vec{r}$ and t. The result is:

$$N(t) = N_0 e^{-\Gamma t} \qquad p = 1 \tag{2.10}$$

$$= N_0 \frac{1}{n_0(0)\, g\, t/8 + 1} \qquad p = 2, \text{ quadrupole trap} \tag{2.11}$$

$$= \frac{1}{\sqrt[p-1]{(p-1)\,\frac{V_p}{V_1^p}\, G_p\, t + N_0^{1-p}}} \qquad p > 1, \text{ general} \tag{2.12}$$

Here N_0 is the total number of trapped atoms at time 0.

These functions may be fit to an observed $N(t)$ profile to extract G_p. If the loss order p is unknown, χ^2 values for the various fits may be compared to determine p. For signal-to-noise ratios in a typical experiment, an order of magnitude of loss must be observed

to differentiate between $p = 1$ and $p = 2$.

2.2 Common loss processes

Most of the loss processes frequently encountered in buffer gas cooling and trapping have been thoroughly investigated in previous buffer gas trapping theses. Table 2.2 provides a list of these loss processes, along with references to more in-depth discussions of each process.

1-body losses due to background gas collisions are dominant when anything larger than trace amounts of background gas are present in the trap. In buffer gas cooling experiments, the buffer gas functions as a loss-inducing background gas once the buffer gas cooling is completed. As such, background gas processes deserve special attention here. As background gas density changes, various mechanisms will limit the trapped atom lifetime. We can characterize the domain of background gas density in which a loss process is dominant by the mean free path for atom-background gas collisions:

$$\lambda = \frac{1}{n_b \bar{\sigma}_E}. \tag{2.13}$$

Here n_b is the density of the background gas and $\bar{\sigma}_E$ is the thermally averaged cross-section for elastic collisions.

At low background gas densities, when λ is larger than the dimension of the cell R_{cell}, elastic collisions with background gas atoms can promote trapped atoms to energetic orbits that leave the cell. In this thesis I call this process "background gas evaporation". If the background gas thermal energy is lower than the trap depth, most background gas collisions will not cause loss. Only rarely will collisions promote an atom to an orbit with energy greater than the trap depth. This differs from the situation in room temperature trapping experiments, where virtually every collision with a background gas atom causes

Table 2.2: Common trapped atom loss processes. The regime listed is where each process is typically dominant. This list is not exhaustive.

Symbols:

λ_b:	mean free path for elastic background collisions
R_{cell}:	the cell radius
η:	ratio of trap depth to trapped atom thermal energy
κ:	ratio of trap depth to background gas thermal energy
n_b:	density of background gas
$\bar{\sigma}_{Xx}$:	thermally averaged cross-section, where X is E (elastic), D (transport), or R (m_J relaxation); x is a (trapped atom-trapped molecule) or b (trapped atom-background gas)
$\bar{v}_x$:	average collision velocity, $\bar{v}_a$ is atom-atom, $\bar{v}_b$ is atom-background gas
f_x:	distribution-averaged fraction of (100% efficient) collisions that cause evaporation, where x is a (atom-atom collisions) or b (atom-background gas collisions)
g_D:	a geometrical factor (2.29)
$c_D(\eta)$:	trap enhancement of diffusion lifetime = $\exp(0.31\eta + 0.018\eta^2)$ for ellipsoidal traps in cylindrical cells
ϵ_{ab}:	efficiency of energy transfer in atom-background gas collisions
γ_b:	ratio of elastic to inelastic background collision cross-sections
m:	atom mass
μ:	trapped atom magnetic dipole moment
R_0:	minimum atom-atom collision radius
†:	this work

1-body loss processes			
Process	Loss coefficient Γ	Regime	Ref.
Background evaporation	$\approx 2\, n_b\, \epsilon_{ab}\, \bar{\sigma}_{Eb}\, \bar{v}_b\, f_b(\kappa)$	$R_{\text{cell}}/\lambda_b < 1$	†
Valley of death	from simulations	$1 < R_{\text{cell}}/\lambda_b < 10$	†, [58]
Drift-diffusion	$\frac{g_D\, \bar{v}_b}{n_b\, \bar{\sigma}_D}\, c_D(\eta)$	$R_{\text{cell}}/\lambda_b \gtrsim 100$	†, [57]
Zeeman relaxation	$n_b\, \bar{\sigma}_{Rb}\, \bar{v}_b$	$\lambda_b < \frac{1}{\sqrt{\gamma_b\, g_D\, c_D}}$	†, [60]
Majorana	$\sim \frac{\hbar}{M} \frac{\eta^2}{R_{\text{cell}}^2} \frac{\mu}{\Delta\mu}$	large η, small M	[57, p. 167]
2-body loss processes			
Process	Loss coefficient g	Regime	Ref.
Evaporation	$\bar{\sigma}_{Ea}\, \bar{v}_a\, f_a(\eta)$	low η	[61, ch. 5],[62]
Dipolar relaxation	$\sim \frac{\mu_0^2\, \mu^4}{16\pi^2 \hbar^2 \bar{v}_a R_0^2}$	large μ	[63, in cgs]

Table 2.2 (continued)

trap loss. Because this loss rate is directly proportional to the rate of atom-background gas collisions, the background gas evaporation rate increases linearly with the density of background gas n_b.

When λ becomes comparable to R_{cell}, the atoms promoted to untrapped energies by these rare atom-background gas collisions are likely to experience additional elastic collisions before they can travel to the trap edge. If λ is very small ($\lambda < R_{\text{cell}}/100$) atoms must diffuse through the background gas before escaping from the trap. In this regime, the loss rate decreases linearly with n_b. This process is called "drift-diffusion" here, after the equation that describes the process.

For λ between these two extremes, the loss rate has a maximum. Conversely, the lifetime of trapped atoms has a minimum in λ. This regime is called the "valley of death", named for the rapid loss of atoms in this background gas regime.[4]

At very high background gas densities (very small λ), inelastic collisions between the atoms and the background gas can cause trap loss. Because atoms are trapped in metastable low-field seeking states, background gas collisions that reorient the $\vec{B}$-projection of the atom's $\vec{\mathbf{J}}$ vector will cause transitions to untrapped high-field seeking states (or to less-trapped low-field seeking states). This loss process is therefore termed "Zeeman relaxation". The n_b at which this loss process becomes dominant depends on the ratio γ_R of the elastic cross-section to the m_J-changing inelastic cross-section. Zeeman relaxation will dominate at lower n_b when γ_R is small. γ_R can be very large for atoms with S electronic configurations, with $\gamma_R > 10^6$. For most non-S-state atoms, γ_R will be quite small, even approaching unity. However, some classes of non S-state atoms have large γ_R, most notably the rare earth atoms, with $\gamma_R > 3 \times 10^4$. This is due to shielding of the non S valence shells by outlying closed shells having no net angular momentum [64]. The Zeeman relaxation

[4] Any resemblance between this loss process and the topography of the Crimea is purely accidental.

loss rate increases linearly with n_b.

2.2.1 Background evaporation

Any atoms in trap orbits that cross the cell's loss surfaces are lost from the trap. If we begin at $t = 0$ with a cloud in thermal equilibrium, atoms will start in a Maxwell-Boltzmann distribution. However, the Maxwell-Boltzmann distribution contains orbits that cross the cell's loss surfaces. Within roughly an orbital period $t_{\rm orbit}$, atoms in these orbits will be lost from the trap. After these atoms are removed, the remaining atom cloud will no longer reside in a Maxwell-Boltzmann distribution. Because each lost atom removes an energy $\gtrsim (\eta + 3/2)\, k_B\, T$ from the atom cloud, the average energy of the atom cloud after these atoms are lost will be lower than the average energy of the original distribution.[5]

If the atomic orbits are ergotic,[6] then all orbits with total energy greater than $U_{\rm trap}$ will be lost from the trap. We can then write an expression for this new out-of-equilibrium distribution. We do this by requiring, at every position $\vec{r}$, that the potential energy plus the kinetic energy is less than $U_{\rm trap}$. The resulting distribution is

$$n(\vec{r}) = n_0\, e^{-U(\vec{r})/k_B T}\, \frac{\int_0^{\eta\, k_B T - U(\vec{r})} \sqrt{K}\, e^{-K/k_B\, T}\, dK}{\int_0^{\eta\, k_B T - U(\vec{0})} \sqrt{K}\, e^{-K/k_B\, T}\, dK}. \tag{2.14}$$

Here K is the kinetic energy of the orbit at location $\vec{r}$. This distribution is compared to the Maxwell-Boltzmann distribution in Fig. 2.1, for $\eta = 3$, at $z = 0$.

If the atoms do not experience any collisions (with themselves, background gas, photons, etc.), the atoms will remain in this out-of-equilibrium distribution indefinitely. If the atoms do experience collisions, these collisions will return the atom distribution to a Maxwell-Boltzmann distribution. The average energy of this new distribution will depend

[5] This assumes that η is larger than the average potential energy in the trap. For a quadrupole trap, $\langle U \rangle = 3\, k_B T$.

[6] Monte-Carlo simulations show that, in general, atomic orbits achieve almost 0 kinetic energy once per revolution, at a location near the largest radial extent of the orbit.

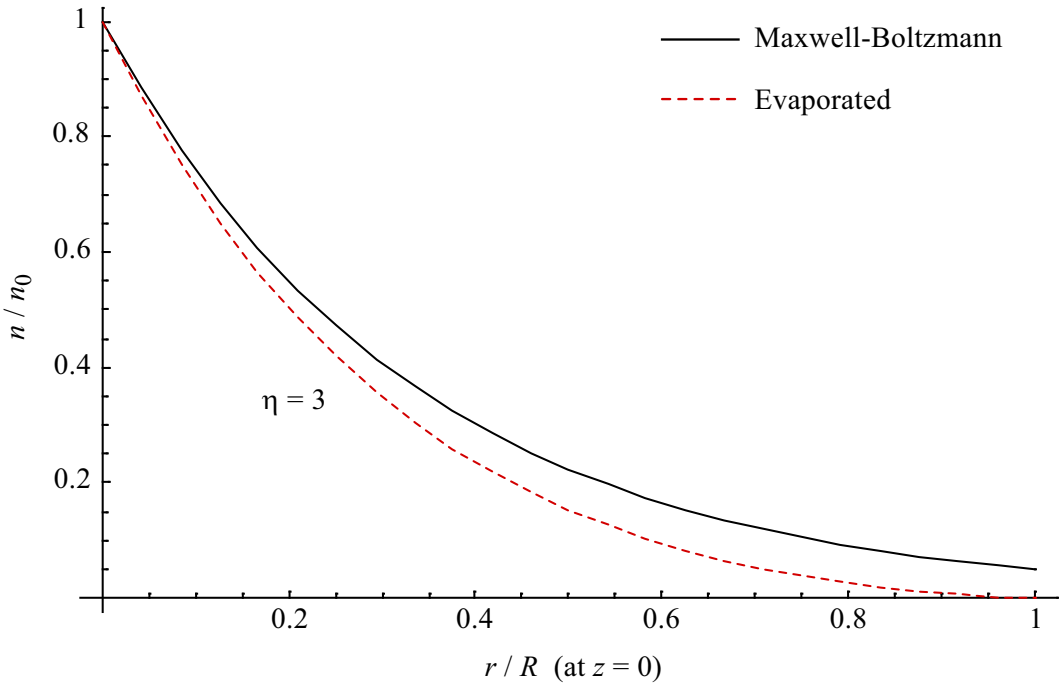

Figure 2.1: The Maxwell-Boltzmann distribution (solid line) and out-of-equilibrium post-evaporation distribution (dashed line), for atoms at $\eta = 3$. The plot is for atoms in an ellipsoidal quadrupole trap at $z = 0$.

on the atoms' collisional partner. If the collisions are elastic atom-atom collisions, this new average energy will be the average energy of the out-of-equilibrium distribution. This new energy will be lower than the energy of the original Maxwell-Boltzmann distribution. The resulting energy loss is the basis of evaporative cooling.

However, if the thermalizing elastic collisions are with some environmental reservoir, such as background gas, the new average energy will be the temperature of the reservoir. Within this new reservoir-temperature Maxwell-Boltzmann distribution, we will again lose any atoms in orbits that cross the cell's loss surfaces. We shall use $f_b(\eta)$ to represent the fraction of atoms in the Maxwell-Boltzmann distribution in the loss surface-crossing orbits.

Imagine we watch one atom as it undergoes many collisions with the background gas. After some time t_f it will undergo a background gas collision that will cause it to enter an untrapped orbit. After an additional time t_o, on the order of the orbital period, it will cross the loss surface and disappear from the trap. At background gas densities such that $\lambda > R_{\text{cell}}$, we have $t_f \gg t_o$, and we can ignore the additional orbit time t_0.

In her thesis, Kim [49, Chapt. 3] demonstrated that atoms are thermalized to the temperature of the buffer gas T_b at a rate

$$\Gamma_{\text{therm}} = n_b \, \bar{\sigma}_E \, \bar{v}_\mu \, \epsilon(M, m). \tag{2.15}$$

Here n_b is the density of background gas, $\bar{\sigma}_E$ is the elastic collision cross-section, $\bar{v}_\mu$ is the average relative atom-background gas velocity, and ϵ describes the efficiency of energy transfer between atoms of mass M and background gas of mass m:

$$\epsilon(M, m) = \frac{2\,M\,m}{(M+m)^2}. \tag{2.16}$$

After a time on the order $\tau_{\text{therm}} = 1/\Gamma_{\text{therm}}$, a trapped atom will be randomly distributed in a Maxwell Boltzmann distribution with temperature T_b. At this time, there is a $f_b(\kappa)$

chance that the atom will be in an untrapped orbit; where κ is the ratio of trap depth to background gas temperature T_b. Note that unless an additional cooling or heating process operates on the atoms, this thermalization process will force $\eta = \kappa$.

We can calculate the rate of evaporative atom loss by taking the product of the thermalization rate Γ_{therm} with the chance for thermalized atoms to be lost $f_b(\kappa)$. Combining these expressions, we find an expression for the loss rate due to background evaporation:

$$\Gamma_{\text{bg evap}} = \frac{1}{t_f} \tag{2.17}$$

$$\approx \Gamma_{\text{therm}}\, f_b(\kappa) \tag{2.18}$$

$$\approx n_b\, \sigma_E\, \bar{v}_\mu\, \epsilon(M,m)\, f_b(\kappa). \tag{2.19}$$

In order to fully describe the background loss, we must calculate $f_b(\kappa)$. This is done by assuming that all atoms with total energy greater than U_{trap} are lost from the trap. We then integrate over the trap distribution, calculating the fraction of atoms, at point $\vec{r}$ and in the background gas kinetic energy distribution, that have total energy greater than U_{trap}. In the cylindrical case, with an ellipsoidal quadrupole field and assuming large κ, f_b is:

$$f_b(\kappa) = \frac{\int_0^\infty \int_0^\infty r e^{-\kappa\sqrt{r^2+4z^2}} \int_{\kappa(1-\sqrt{r^2+4z^2})}^\infty \sqrt{K_b} e^{-K_b} dK_b\, dr\, dz}{\int_0^\infty \int_0^\infty r e^{-\kappa\sqrt{r^2+4z^2}} \int_0^\infty \sqrt{K_b} e^{-K_b} dK_b\, dr\, dz}, \tag{2.20}$$

where r and z are normalized to R, and K_b is the background gas kinetic energy normalized to the background gas temperature. This integral can be performed numerically; the result fits (to within 14% for $\kappa > 3$) to

$$f_b(\kappa) = \left(\frac{1}{2}\,\kappa^{3/2} + \frac{1}{4}\,\kappa^{5/2}\right) e^{-\kappa}. \tag{2.21}$$

We can use Monte Carlo simulations of atoms trapped at low background gas density to verify the analytic results of this section. The Monte Carlo simulation used

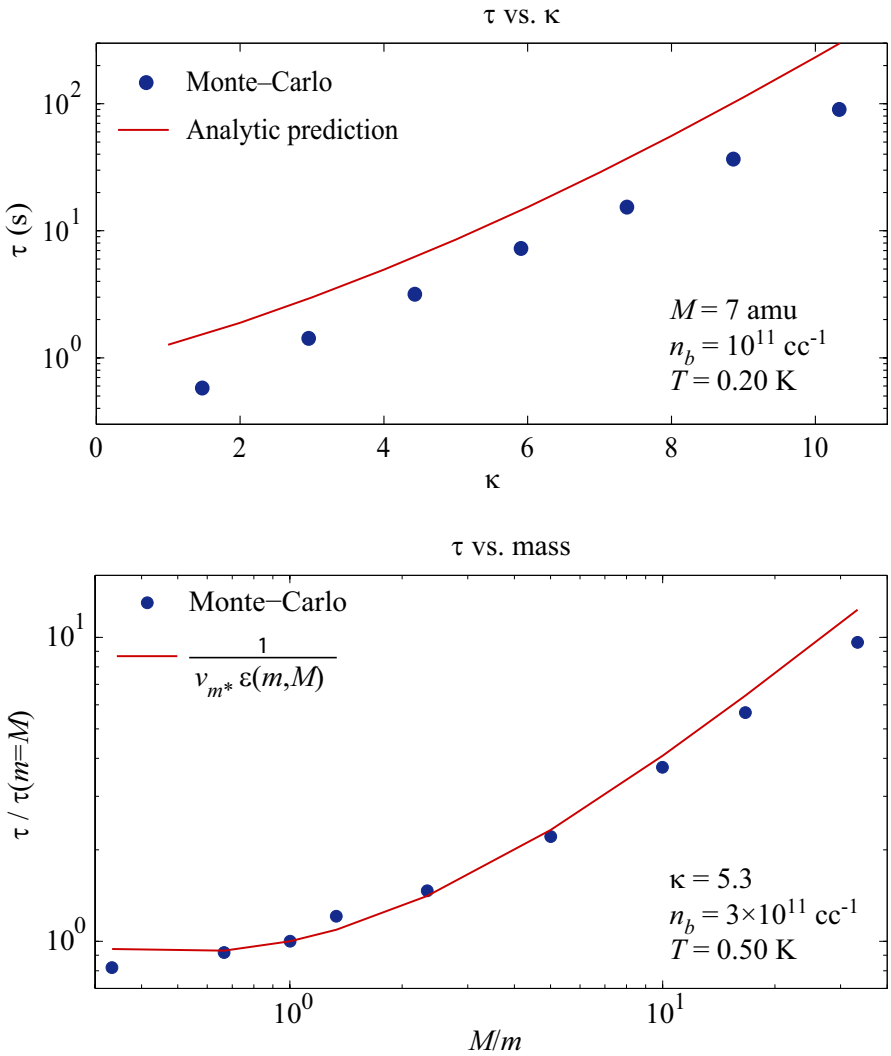

Figure 2.2: The upper plot shows background evaporation lifetimes vs. κ. The results are for a cylindrical trapping volume with an ellipsoidal quadrupole field. The analytic expression overestimates the lifetime by a factor of 2. The lower plot shows the dependence of background evaporation lifetime vs. the ratio of atom mass to background gas mass.

was almost identical[7] in operation to the algorithm developed by Michniak in his thesis [58]. Briefly, this algorithm works as follows: A number of atoms are chosen from the Maxwell-Boltzmann trap distribution. Each atom is evolved under the equation of motion for a trapped dipole using an adaptive Runge-Kutta routine. Each atom is collided with background gas atoms, pulled from a Maxwell-Boltzmann velocity distribution. Times between collisions are taken from an exponential distribution; this distribution has a mean collision time equal to the mean atom-background gas collision time $t_{\rm col} = 1/n_b\sigma_E\bar{v}_\mu$. These collisions are repeated for each atom until the atom exits the trap. After performing this simulation, we create a histogram of the number of Monte Carlo atoms in the trap vs. time, and then fit for the lifetime of the simulated atoms. For a detailed description of the Monte Carlo simulation algorithm, see [58]. A comparison of Monte Carlo simulations of atom lifetime in the large λ regime to the background gas prediction is given in Fig. 2.2. We find that the analytic prediction derived here agrees to within a factor of 2 of the Monte-Carlo result, for the mass and κ ranges shown. The discrepancy might be dealt with by integrating the atom loss after every background gas collision, instead of every $1/\epsilon$ collisions; however, doing so would hide the analytic mass dependence of the evaporation rate.

2.2.2 Drift-diffusion

In the short mean free path regime, when $\lambda < R_{\rm cell}/100$, atoms must diffuse through the background gas to reach the cell wall. The magnetic field causes a drift velocity returning atoms to the center of the trap. The equation governing this behavior is the drift-diffusion equation [65]. With $n(\vec{r}, t)$ representing the (non-equilibrium) atom distribution

[7]The algorithm used here differs in three ways from that described in [58]. Firstly, atom initial positions are taken from a trap Maxwell-Boltzmann distribution instead of a uniform distribution. This minimizes the portion of the atom histogram at early times that is not useful for calculating long-time behavior. Secondly, the Runge-Kutta minimum step size is adjusted to give accurate results at low background gas densities. Finally, the transformation to the center of mass frame for elastic collisions is handled in one step instead of the two-step transformation used in [58].

at time t, the equation is:

$$\frac{\partial n}{\partial t} = D\,\nabla^2 n - \vec{\nabla}\cdot(n\,\vec{v}_{\rm drift}). \tag{2.22}$$

The constant D is called the diffusion constant; it is the average square displacement of a freely diffusing particle per time. It has been calculated [66] to be

$$D = \frac{3\pi}{32}\frac{\bar{v}_\mu}{n_b \bar{\sigma}_D}. \tag{2.23}$$

for particles undergoing ballistic hard-sphere elastic collisions, where $\bar{\sigma}_D$ is the thermally averaged transport cross-section. The drift velocity $\vec{v}_{\rm drift}$ can be related to the potential U experienced by the diffusing particles using the particle mobility and the Einstein-Smoluchowski relation [65]:

$$\vec{v}_{\rm drift} = -\frac{D}{k_B T}\vec{\nabla}U(\vec{r}). \tag{2.24}$$

The diffusion equation is a separable parabolic-elliptic partial differential equation. As such, the solution can be expanded in a set of eigenmodes. For each eigenmode, each side of equation (2.22) is equal to a constant κ_i, where i indexes the eigenmode. If we separate variables, we can easily solve for the time dependence of $n(\vec{r},t)$. We find

$$n(\vec{r},t) = \sum_i n_i(\vec{r})\,e^{-t/\tau_i}. \tag{2.25}$$

Each $n_i(\vec{r})$ is an eigenfunction of the spatial equation, with eigenvalue $\kappa_i = 1/D\tau_i$. The eigenfunctions are determined by setting $n_i(\vec{r}) = 0$ at the surfaces of the trapping cell.

In general there will be a minimum $\kappa_i = \kappa_0$, associated with the eigenfunction with the weakest spatial variation. If we observe the atom cloud for long enough, the only remaining eigenmode will be this lowest order eigenmode, decaying with a lifetime $\tau_0 = 1/\kappa_0 D$.

Free diffusion

When the trapping field is off, the drift term in the diffusion equation is zero, and the particles within the cell diffuse according to the free diffusion equation

$$\frac{1}{D}\frac{\partial n}{\partial t} = \nabla^2 n. \tag{2.26}$$

This equation is easily solved for cells with simple geometric shapes. For a cylindrical cell of radius R and top-to-bottom length L, we find

$$n_0(\vec{r}) = n_0(0)\, J_0\left(\frac{j_{01}\, r}{R}\right) \cos\left(\frac{\pi z}{L}\right), \tag{2.27}$$

$$\tau_0 = \frac{n_b\, \bar{\sigma}_D}{g_{\mathrm{cyl}}\, \bar{v}_\mu}, \tag{2.28}$$

$$g_{\mathrm{cyl}} = \frac{3\pi}{32}\left(\frac{j_{01}^2}{R^2} + \frac{\pi^2}{L^2}\right). \tag{2.29}$$

$J_0(r)$ is the zeroth-order Bessel function of the first kind [67], and $j_{01} = 2.40483\ldots$ is the first zero of this function.

Trap diffusion

When the trapping field is on, the eigenfunction equation can become quite complex. Weinstein solved the drift-diffusion equation in his thesis for the special case of atoms in a spherical quadrupole trap within a spherical cell [57, p. 24]. The lowest order solution is a rather opaque special function. This special function solution can be evaluated numerically. When this is done, we find that the exact solution is remarkably close to the the free-diffusion solution n_{free} multiplied by the Maxwell-Boltzmann trap distribution:

$$n_0(\vec{r}) \approx n_{\mathrm{free}}(\vec{r})\, e^{-U(\vec{r})/k_B T}. \tag{2.30}$$

When η is greater than 4 or so, this reduces purely to the Maxwell-Boltzmann trap distribution, as n_{free} is constant near $\vec{r} = 0$. This means that the simple Maxwell-Boltzmann trap distribution may be used to model trapped atoms even when a large amount of background gas is present. This is important when we seek to investigate the atoms spectroscopically: In order to understand the absorption spectrum of the trapped atoms and use the spectrum to extract physical parameters, we must have a good model of the trapped atom distribution.

We can also ask how the spherical eigenvalues depend on the strength of the trapping field. As η is increased, we find that the κ_i become exponentially smaller. If we solve for the eigenvalues using numerical methods[8] we find that for $\eta < 16$, the diffusion lifetime is

$$\tau_{\text{sph}}(\eta) = \frac{32}{3\pi^3} \frac{R^2\, n_b\, \bar{\sigma}_D}{\bar{v}_\mu}\, e^{0.228\eta + 0.017\eta^2}. \tag{2.31}$$

Of course, we never have a spherical cell with a spherical quadrupole trap. Unfortunately, solving the drift-diffusion equation in the cylindrical case becomes quite difficult. The trap potential energy, for an ellipsoidal quadrupole trap in cylindrical coordinates, is

$$U_{\text{ellip.}} = \frac{\eta\, k_B T}{R} \sqrt{r^2 + 4z^2}. \tag{2.32}$$

This form inextricably couples the r and z dimensions of the equation, meaning that the spatial equation can not be separated into a pair of one-dimensional equations. The resulting unseparable elliptical equation resists treatment by the lion's share of numerical methods.

Two approaches were used to attack the problem here. First, the equation was solved by making a rather crude approximation to U. Under this approximation, we let

$$U_{\text{ellip.}} \sim U_{\text{biconic}} = \frac{\eta\, k_B T}{R} (r + 2|z|). \tag{2.33}$$

[8] MATLAB's 1-d boundary value ODE solver was used here.

Instead of ellipsoidal equipotentials, this potential has biconic equipotentials (two conic surfaces placed base-to-base at $z = 0$). Nevertheless, the local magnetic field norm of this approximate potential agrees with that of the ellipsoidal potential over all space to within a factor of $\sqrt{2}$. Using this approximate potential, we can separate the problem into the r and z dimensions. When we solve these equations, we again find remarkable agreement of the lowest-order eigenfunction to the Maxwell-Boltzmann distribution. The diffusion lifetime given by this approximation is

$$\tau_{\mathrm{cyl}}(\eta) = \frac{n_b\,\bar{\sigma}_D}{g_{\mathrm{cyl}}\,\bar{v}_\mu}\,e^{0.31\eta+0.018\eta^2}. \tag{2.34}$$

This lifetime is greater than the lifetime from the spherical result, for cells with the same radii. The lifetime is $\pi^2/j_{01}^2 = 1.7$ times greater at $\eta = 0$, growing to about 7 times greater at $\eta = 16$. We have assumed that L is large enough compared to R that we can ignore diffusion to the cell axial ends.

The other approach was to use the Monte-Carlo simulation previously described to calculate the lifetime and final distribution of the diffusing atom cloud, beginning from the trap Maxwell-Boltzmann distribution. As is shown in Fig. 2.3, the Monte-Carlo lifetime agrees quite well with the lifetime calculated from the biconic approximate potential.

2.2.3 The valley of death

In the valley of death, atoms experience a maximum in their background gas-driven loss rate. The loss behavior in this region defies analytic prediction: the assumptions of background gas evaporation are violated when atoms in untrapped orbits suffer collisions before they can exit the trap. At the same time, diffusion is not a valid description of transport behavior until λ becomes smaller than approximately 1/100th of the cell size.

One approach to calculating the valley of death loss rate, which is not too unreasonable, is to simply take the reciprocal sum of the limiting loss rates on either side of the

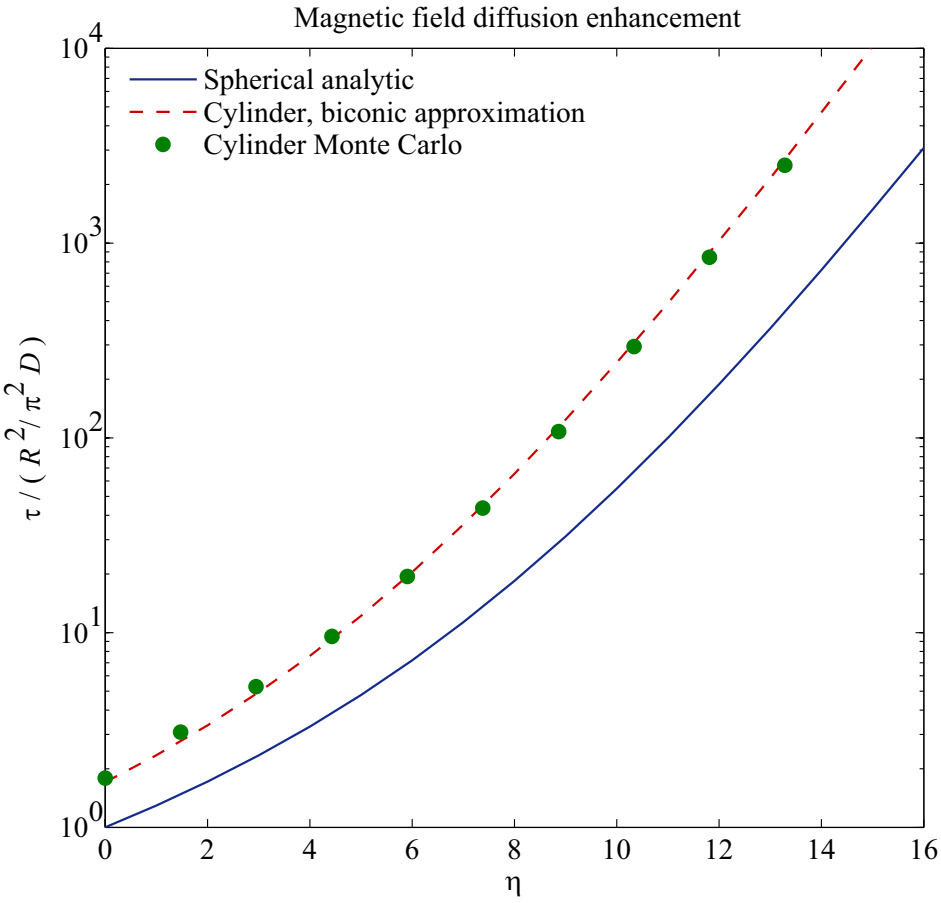

Figure 2.3: Drift-diffusion lifetimes vs. η. The Monte-Carlo diffusion cross-section is taken to be $\sigma_D = 0.8 \times \sigma_E$, to give agreement to the cylindrical solution at $\eta = 0$. L was taken to be ∞ for these calculations.

valley of death. This is rather coarse however. Because the atom loss has a maximum here, an experiment can succeed or fail based on how long background gas is allowed to remain at valley of death densities with respect to the atom loss rate. Factor of unity errors result in exponential changes in the number of atoms.

Our best tool for calculating valley of death loss rates is the Monte Carlo simulation described above. An example of this simulation applied to a few different atomic masses and values of η is shown in Fig. 2.4.

2.2.4 Zeeman relaxation

The previous three loss processes discussed up to here have all been mediated by elastic collisions between trapped atoms and the background gas. However, trap loss can also be caused by inelastic atom-background gas collisions that change the internal state of the trapped atom. We are of course interested in collisions that result in decay from the most low-field seeking m_J state. If we let $\bar{\sigma}_{R;m'_J}$ represent the thermally averaged cross-section for collisions causing relaxation from the most low-field seeking state to some other Zeeman state m'_J, then the rate for collisions from the most low-field seeking state m_{LFS} to state m'_J will be [68]

$$\Gamma_{m_{\mathrm{LFS}}\rightarrow m'_J} = n_b\, \sigma_{R;m'_J}\, \bar{v}_\mu. \tag{2.35}$$

If λ is large compared to the cell size, the relaxed atom will be ejected from the trap without suffering additional collisions (or evaporate relatively quickly, if it is relaxed into a more weakly low-field seeking state). If λ is small, the relaxed atom will diffuse to the cell wall, experiencing either a weak inward drift velocity (for less low-field seeking atoms) or an outward drift velocity (for high-field seeking atoms). As long as the time taken by the atom to diffuse from the cell is shorter than the time it would take for an additional collision to return the atom to the LFS state, the atom will be lost from the trap. If this is the

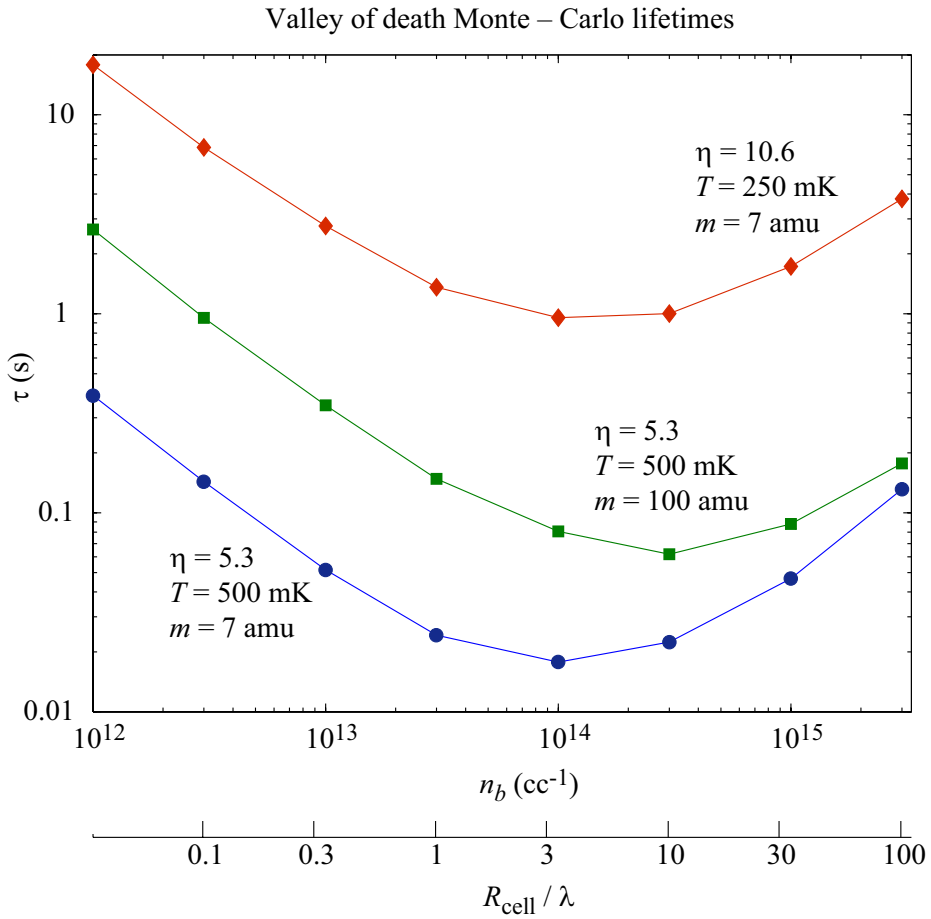

Figure 2.4: Monte-Carlo calculations of the valley of death loss behavior, for low mass and high mass limits. The simulations use $\sigma_E = 10^{-14}$ cm^2. The limiting low and high buffer gas density behaviors vs. η and M are described in (eqn:bgEvap) and (2.34), respectively. The dependence of lifetime on η and M at a specific n_b within the valley of death can be calculated using the Monte-Carlo code described in §2.2.1

case, then the rate of trapped atom loss Γ_R due to these inelastic collisions will just be $\sum_{m'_J} \Gamma_{m_{\rm LFS}\to m'_J}$.

In general this condition — short diffusion time compared to reverse relaxation time — will be satisfied. On the one hand, the diffusion time for relaxed atoms will be exponentially faster than for the most low-field seeking atoms. On the other hand, the reverse relaxation rate is exponentially slower than $\Gamma_{m_{\rm LFS}\to m'_J}$. This can be seen from a detailed balance argument. Consider only two Zeeman states, with populations $n_{\rm LFS}$ and $n_{\rm HFS}$, and with an energy splitting ΔE. When the states are in thermal equilibrium, the Maxwell-Boltzamnn distribution gives

$$\frac{n_{\rm LFS}}{n_{\rm HFS}} = e^{-\Delta E/k_B T}. \tag{2.36}$$

In thermal equilibrium, the change in each population must be 0. Setting the rate equation for each state equal to 0 gives

$$\frac{dn_{\rm LFS}}{dt} = 0 = -n_{\rm LFS}\,\Gamma_{\rm LFS\to HFS} + n_{\rm HFS}\,\Gamma_{\rm HFS\to LFS}. \tag{2.37}$$

And therefore

$$\Gamma_{\rm HFS\to LFS} = e^{-\Delta E/k_B T}\Gamma_{\rm LFS\to HFS}. \tag{2.38}$$

This argument is performed for arbitrary numbers of states in Cort Johnson's thesis [60].

Because the rate of reverse relaxation is slow compared to the relaxed atom loss rate, the trap loss rate due to Zeeman relaxation is given just by the Zeeman state-change rate, and we have

$$\Gamma_R = n_b\,\bar{\sigma}_R\,\bar{v}_\mu, \tag{2.39}$$

where $\bar{\sigma}_R = \sum_{m'_J} \bar{\sigma}_{R;m'_J}$. It is useful to cast this rate in terms of the elastic mean free path λ. Then

$$\Gamma_R = \frac{\bar{v}_\mu}{\lambda\,\gamma_R}. \tag{2.40}$$

where $\gamma_R = \bar{\sigma}_E/\bar{\sigma}_R$ is the ratio of elastic to relaxation thermally averaged cross-sections.

2.3 Thermal isolation

Before buffer gas cooling, a dilute gas of the species to be trapped is prepared, with common preparation methods including laser ablation and gas discharge. This dilute gas enters the buffer gas cell at approximately 1000 K, and requires about 100 collisions with the buffer gas to cool to near the buffer gas temperature [49]. This sets a requirement on the initial size of the elastic mean free path λ, viz. $\lambda(t=0) \lesssim R_{\text{cell}}/100$. After buffer gas cooling is accomplished, the buffer gas acts as a background gas, causing loss via the previously discussed processes. The large number of collisions at the small mean free path used for buffer gas loading pins the atom temperature to the background gas temperature, which is in turn pinned to the cell wall temperature. If we desire to lower the atom temperature below the ~ 200 mK cell temperature, we must find a way to raise λ such that the heating rate from background gas collisions is negligible with respect to whatever cooling rate we can apply to the trapped atom cloud. Barring the unlikely ability to tune σ_E to 0 (by tuning temperature and laboratory fields, say), this many-orders-of-magnitude increase in λ can only be accomplished by removing the background gas.

2.3.1 Background gas heating rate and thermal isolation density

We must first find out to what density the buffer gas must be reduced to achieve thermal isolation. To do this we calculate the heating rate from background gas collisions. We will then balance this heating rate against the atomic cooling rate.

After averaging over collision angles, we find that each background-atom collision adds an energy [49]

$$\overline{dE} = (K_b - K_a)\,\epsilon(m, M) \tag{2.41}$$

to the atom's total energy E_a, where K_b is the energy of the background gas atom and K_a

is the atoms' kinetic energy. This atom must stay in the trap long enough to collide with another trapped atom, if this energy is to be added to the trapped atom temperature. The probability for this atom to leave the trap is equal to

$$p_{\text{loss}} = f\left(E_a + dE\right), \tag{2.42}$$

where $f(E)$ is the fraction of orbits with total energy E that cross the cell's loss surfaces. If we average over all collisions, we find a per atom heating rate

$$\frac{dq_b}{dt} = n_b \bar{\sigma}_{bE} \bar{v}_\mu \left\langle dE\left(1 - f(E_a + dE)\right)\right\rangle. \tag{2.43}$$

To lowest order, we can separate the the two terms in the average in (2.43). If we do this, then, to a crude approximation, the heating rate is

$$\frac{dq_b}{dt} \approx n_b \bar{\sigma}_{bE} \bar{v}_\mu \frac{3}{2} k_B \left(T_b - T_a\right) \epsilon(m, M) \left[1 - f_b\left(\frac{U_{\text{trap}}}{(T_b - T_a)\epsilon(m, M) + T_a}\right)\right], \tag{2.44}$$

where f_b is the 1-body evaporation fraction calculated in §2.2.1. In the limit of small $\kappa \equiv U_{\text{trap}}/k_B T_b$, the evaporation fraction f_b is near unity. In the limit of large κ, f_b is zero. In these two limits, then, the heating rate is

$$\frac{dq_b}{dt} \approx 0 \qquad\qquad k_B T_b \gg U_{\text{trap}} > k_B T_a \tag{2.45}$$

$$\frac{dq_b}{dt} \approx \frac{3}{2} n_b \, \bar{\sigma}_{bE} \, \bar{v}_\mu \, k_B \left(T_b - T_a\right) \epsilon(m, M) \qquad\qquad k_B T_b \ll U_{\text{trap}} \tag{2.46}$$

Meanwhile, the evaporative cooling rate due to atom-atom collisions (in a spherical quadrupole trap) is [61]:

$$\frac{dq_a}{dt} \approx -4\sqrt{2}\, n_0 \, \bar{\sigma}_{aE} \, \bar{v}_a \, k_B T_a (\eta - 3) \, \eta \, e^{-\eta} \tag{2.47}$$

with peak atom density n_0, atom-atom elastic cross-section $\bar{\sigma}_{aE}$, mean atom speed $\bar{v}_a$, and atom temperature T_a. If we require that the background heating rate be less than the

atom-atom cooling rate even when $U_{\text{trap}} > k_B T_b > k_B T_a$, then the maximum allowable background density for thermal isolation is

$$n_{\text{isolation}} \approx \frac{8\sqrt{2}}{3}\, n_0\, \frac{\bar{\sigma}_{aE}}{\bar{\sigma}_{bE}} \sqrt{\frac{m}{M+m}}\, \frac{\kappa^{3/2}}{\eta^{3/2}}\, (\eta - 3)\eta e^{-\eta}. \tag{2.48}$$

Atoms are typically evaporated at $\eta = 5$. The above condition must be satisfied until $\kappa \approx 1$, when the small κ behavior from background gas heating takes over. Substituting these requirements into the above equation we have

$$n_{\text{isolation}} \approx 0.002\, n_0\, \frac{\bar{\sigma}_{aE}}{\bar{\sigma}_{bE}} \sqrt{\frac{m}{M+m}}. \tag{2.49}$$

For trapped lithium, $\bar{\sigma}_a$ is 1.3×10^{-13} cm^2 [69] in the s-wave limit, and $\bar{\sigma}_b$ is $\approx 10^{-14}$ cm^2 [70]. Assuming we have a peak Li density of 10^{12} cc^{-1}, this gives a required density for thermal isolation of trapped lithium of

$$n_{\text{Li-He isolation}} \approx 1.4 \times 10^{10}\, \text{cc}^{-1}. \tag{2.50}$$

For a more in-depth and exact discussion that considers all the heating and cooling rates experienced by the atoms, see Newman's thesis [71].

2.3.2 Buffer gas removal

At the initial loading time, the buffer gas density is quite large, in the diffusive loss regime. We must then remove the buffer gas, leaving a background density of only 10^{10} cc^{-1} (see previous section). At some time during the removal of the buffer gas, the atoms loss rate will be in the valley of death. In order to have any significant number of atoms remaining after buffer gas removal, we must therefore remove the buffer gas with a time constant faster than the valley of death loss rate. There are three methods we may use to remove the buffer gas: First, a "freeze-out", accomplished by lowering the cell temperature until the vapor density of the buffer gas is less than the desired final background gas density.

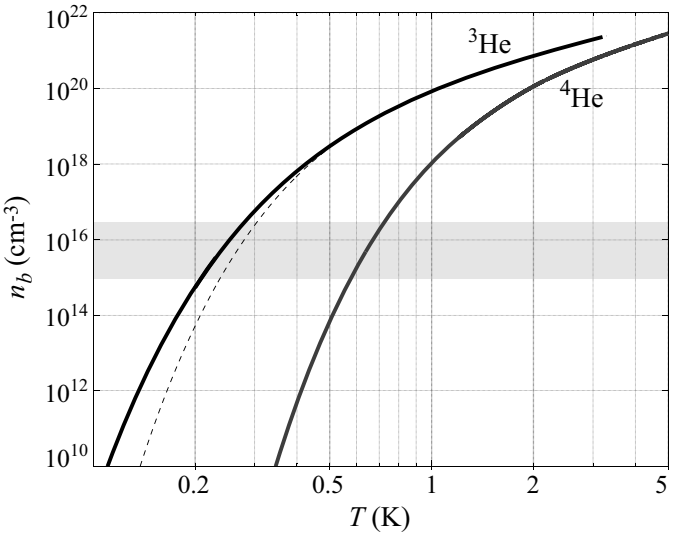

Figure 2.5: Vapor density curves of ^{3}He and ^{4}He, taken from [48].

Second, we can use a valve to open the cell to a pumping chamber. Third, we can keep the cell temperature very low initially, and attempt to thermalize the hot atoms with a dynamic "puff" of buffer gas. This last method is known as "cold loading".

Freeze-out

Fig. 2.5 shows the vapor density of ^{3}He and ^{4}He. These are the only two buffer gases that have significant vapor pressures at achievable trapping temperatures. We can make fits to these curves to obtain the vapor density of buffer gas at a given cell temperature [58, 61]:

$$n_{\text{vapor}} = a \left(\frac{T}{K}\right)^c e^{-b/T} \tag{2.51}$$

with

Gas	a (cc^{-1})	b (K)	c
^{3}He	7.7×10^{20}	2.41	3/2
^{4}He	1.3×10^{22}	9.83	0

If we let the time constant for cooling the cell be τ_{therm}, then we find that the instantaneous time constant for removing buffer gas is

$$\tau_{\text{pump}}(t) = \tau_{\text{therm}} \frac{1}{b + c\,T_{\text{cell}}(t)} \frac{T_{\text{cell}}^2(t)}{(T_{\text{cell}}(t) - T_{\text{base}})}, \tag{2.52}$$

where T_{cell} is the cell temperature at time t and T_{base} is the final temperature achieved by the cell. Because the time constant for cooling the cell is typically quite long, around 6 s [57], and because achievable values of T_{base} are near 150 mK, we expect this method will only work for large μ atoms, where ^{4}He can be used for the buffer gas and where the valley of death lifetime is long.

Fast valve pump-out

We can remove the buffer gas much more quickly if we pump through a fast-actuating valve. A chamber is attached to the cell that contains a large surface area of activated charcoal sorb [52]. At cryogenic temperatures, this charcoal sorb acts as a pump for helium, until the charcoal is saturated with helium. Since the charcoal can absorb ≈ 1 gm of He for every gm of charcoal [52], the experiment can be run indefinitely without saturating the charcoal sorb.

These two chambers are connected with a valve, operating at the temperature of the cell. If A is the area of the valve aperture between the cell and pumping chamber, then the time constant for buffer gas removal when the valve is open will be [72]

$$\tau_{\text{pump}} = \frac{4V_{\text{cell}}}{\bar{v}_b A}, \tag{2.53}$$

where V_{cell} is the cell volume and $\bar{v}_b$ is the thermal buffer gas speed. For information regarding our cryogenic valve design, see App. B.

Cold loading

In cold loading, the cell is held at a low temperature where the buffer gas has negligible vapor density. In experiments in which the hot atoms are introduced by laser ablation, a puff of buffer gas is liberated along with the hot atoms. The buffer gas remains in its vapor phase long enough to thermalize the ablated atoms. Because only a minimal amount of heat is deposited in the cell, the buffer gas can rapidly freeze onto the cell walls, leaving behind the trapped atoms.

2.3.3 Wind

When buffer gas is removed from the cell, the gas has a net velocity away from the center of the trap. Trapped atoms therefore feel a cumulative force due to collisions with the buffer gas atoms being removed. If this force is so large as to overcome the trapping force from the magnetic field, the atoms will be lost from the trap. In his thesis, Weinstein showed that the pumpout time constant $\tau_{\rm pump}$ must not be faster than a critical time constant

$$\tau'_{\rm wind} = \frac{n_b\,\bar{\sigma}_E\,m\,\bar{v}_\mu R\,L}{U_{\rm trap}}. \tag{2.54}$$

$$\approx \frac{8\,n_b\,\bar{\sigma}_E\,R\,L}{\pi\,\eta\,\bar{v}_\mu} \tag{2.55}$$

One should note that this critical constant is known only to a factor of unity [57]. An example of $\tau'_{\rm wind}$ is shown in Fig. 2.6, for 350 mK lithium in a 2.7 K deep trap, for $R = 3.7$ cm and $L = 10$ cm.

2.3.4 Remnant background gas

After the buffer gas removal, it is possible that some buffer gas remains in the gas state, at a density higher than the target isolation density. This remaining buffer gas is

caused by gas desorbing from liquid films. If the buffer gas was removed by cell cooling, these films can emanate from "hot spots" within the cell that remain hot. If a pump-out was used, the cell may be hotter, and the desorbing film can emanate from the entire cell surface. We can also have a remnant background gas density if the pumping chamber cannot pump below a given density.

A very nice treatment of these desorbing films is contained in Michniak's thesis [58]. We find, that for a given starting thickness of film on the cell walls, a pumping constant τ_{pump}, and cell wall temperature T_{wall}, the pump-out stalls at a buffer gas density determined by the thickness of the He film.

To deal with this He film, one must pump on the cell while the cell is at a high temperature. This temperature should be the highest temperature achievable without losing too many atoms due to background gas-driven loss. After pumping for a few seconds, the temperature of the cell walls must be reduced. In order to achieve thermal isolation, a 200 mK temperature drop is typically necessary.

2.3.5 Thermal isolation of 1 μ_B species

In order to have a dense sample of atoms in thermal isolation, we must remove the buffer gas faster than total atom loss time. At the same time, the gas must be removed slowly enough that the pump-out does not remove buffer gas too quickly that wind becomes an issue.

At any time t during the pumpout, there will be an instantaneous background gas density $n_b(t)$. At this instantaneous background gas density, the pumpout time constant is $\tau_{\mathrm{pump}}(n_b)$. We can make a parametric plot of this pumpout time constant versus background gas density. In order to be successful, the parametric trajectory traced on this plot must not spend significant time in "forbidden zones": An "atom loss zone" where τ_{pump} is longer

Figure 2.6: Forbidden pumping regions in n_b-τ_{pump} space and example pumping trajectories. The data points are Monte-Carlo simulations of atom lifetimes at 250 mK (diamonds), 350 mK (squares), and 500 mK (circles). The atom mass is 7 amu and the trap depth is 2.7 K; the elastic cross-section used is 10^{14} cm^2. The upper shaded area is the forbidden atom loss region for 350 mK atoms. Note that we can have τ_{pump}-n_b combinations in this upper region without significant atom loss, as long as the pump trajectory does not spend more than an atom lifetime in this forbidden region. The lower shaded area is the approximate wind loss forbidden region. Also shown are two pumping trajectories, using a 1.4 in diameter valve, opened linearly in 80 ms (dotted line) and 300 ms (solid line, arrows show direction of increasing time and annotations show times corresponding to the trajectory location).

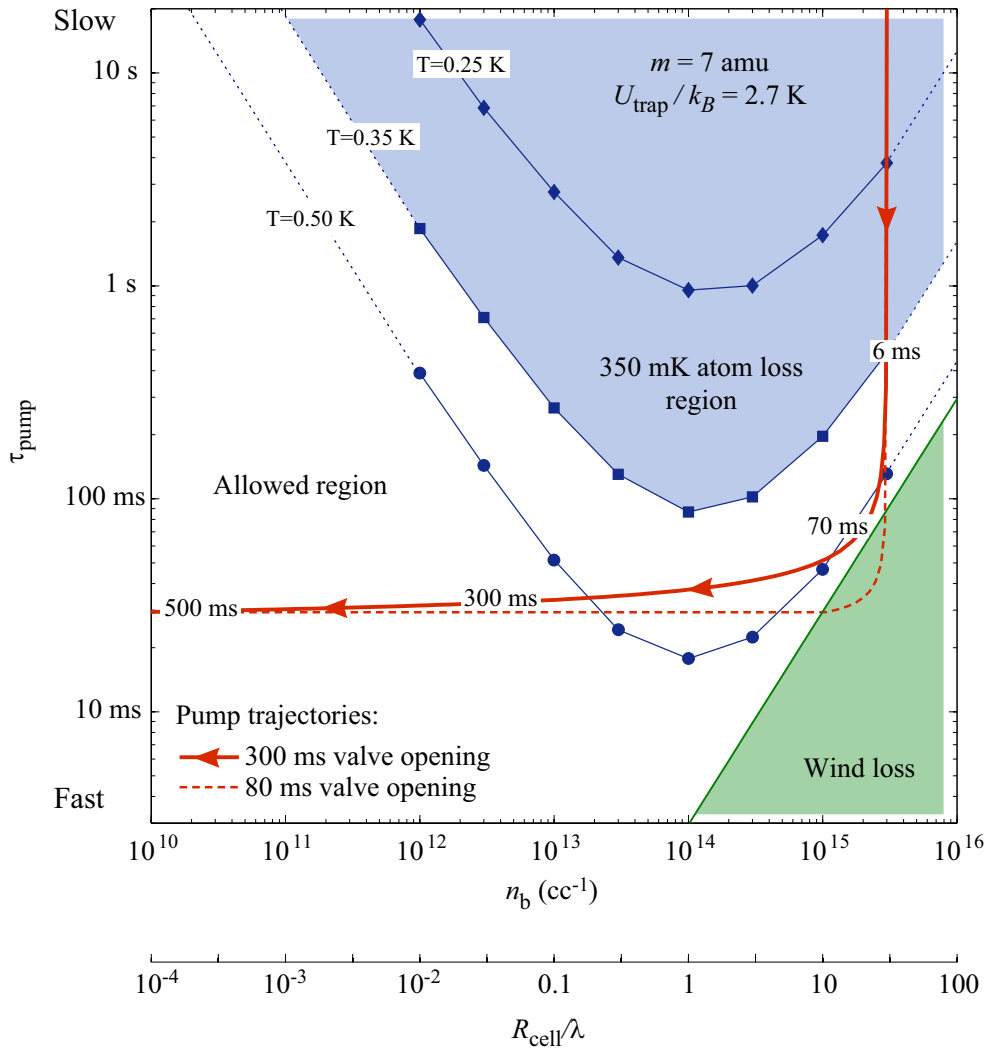

Figure 2.6 (continued)

than the atom lifetime at n_b, and a "wind loss zone" where $\tau_{\rm pump}$ is shorter than the critical wind time constant at n_b. Such a plot, for 7 amu, 1 μ_B atoms in a 4 T trap (the current state-of-the-art in magnetic traps [20]), is depicted in Fig. 2.6. We find that the atom loss and wind loss forbidden zones meet for atom temperatures larger than 500 mK or so. At very cold atom temperatures, less than 250 mK, we can remove the background gas by opening a pumping aperture with a pumping time constant of 200-300 ms. At intermediate atom temperatures, the pumping trajectory must navigate a narrow path of allowed $\tau_{\rm pump}$ and n_b. This can be achieved by adjusting $\tau_{\rm pump}$ during the pump-out. A couple of pumping trajectories, achieved by adjusting the amount of time over which a 1.4 in diameter valve is opened, are also shown in Fig. 2.6. In practice, the appropriate pumping trajectory can be found by progressively decreasing the valve opening time just until atoms do not experience wind loss. If the atom temperature is low enough, the atoms will not experience significant static background-driven loss, and a significant density of atoms will remain after pumpout.

However, due to buffer gas films some remnant background gas density will remain in the cell. This remnant density will prevent thermal isolation. We would like to use the "cryo-bakeout" method of Michniak. In order to obtain the requisite temperature change, the base temperature of our experiment must be very cold. This is because the trapped 1 μ_B atoms can not tolerate a very high temperature during the bakeout. If the buffer gas is pumped at 350 mK, we must have a 150 mK cell base temperature to achieve a 200 mK temperature swing.

Chapter 3

Lithium experiments

Our experiments with lithium (Li) were motivated by two desires. First, we wished to demonstrate that buffer gas cooling could be used to generate large samples of cold trapped 1 μ_B gases. Previous experience with sodium (Na) indicated that large numbers (on the order of 10^{13} atoms) of the alkali atoms could be produced using laser ablation [55]. Because of its simple atomic structure, spectroscopy of Li was expected to be straightforward, with high signal-to-noise. Li does not suffer large Li-Li spin relaxation in the ultracold limit [73]. This suggests that Li is highly isotropic in its collisions, and that Li will not spin relax in Li-He collisions.

Second, we wished to use lithium as a model species for the trapping of hydrogen. Li is the most closely related atom to hydrogen (H), in that it is the next most massive atom with just one s valence electron. Additionally, the efficiency ϵ of energy transfer in He-Li collisions is similar to the efficiency in He-H collisions, with

$$\epsilon(^3\mathrm{He}, ^7\mathrm{Li}) = 0.410,$$

$$\epsilon(^3\mathrm{He}, ^1\mathrm{H}) = 0.375.$$

If we can trap and cool Li using buffer gas techniques, this suggests we could also trap and

cool H as well as its heretofore untrappable isotopes deuterium and tritium. If we manage to trap Li simultaneously with H, we can use Li to sympathetically cool the trapped H, producing denser samples of ultracold H than available previously [1, 74]. This would lead to denser H BECs, as well as precision measurements with strong signals.

Our experimental efforts with Li occurred in three major stages. First, we conducted a test experiment to merely load Li into a buffer gas trap. In this experiment we calibrated our spectroscopy and made thermal measurements on our apparatus. In the second stage we added a valve for buffer gas-removal and tuned our loading and pump-out processes to obtain large densities of Li after buffer gas removal. In the third experiment, we added the ability to change the trap depth in the experiment, to attempt evaporative cooling of the trapped Li.

3.1 Spectroscopic methods

In order to measure physical properties of the Li that we cooled and trapped, we used laser absorption spectroscopy [75, Chapt. 6]. For general details on how laser absorption spectroscopy is performed on our trapped atoms, see Appendix A.

3.1.1 Spectroscopic apparatus

A schematic of the optical setup is shown in Fig. 3.1. Single wavelength light is produced by a New Focus Velocity Laser operating at 670 nm [76]. The beam is passed through an optical diode [77]. A small fraction of the beam is picked off and monitored with a wavemeter [78]. Using the wavemeter, we adjust the center frequency of the laser to $\sim$670.970 nm (vac. λ), between the $D1$ and $D2$ transitions of lithium, at 670.976 nm and 670.961 nm[37], respectively.

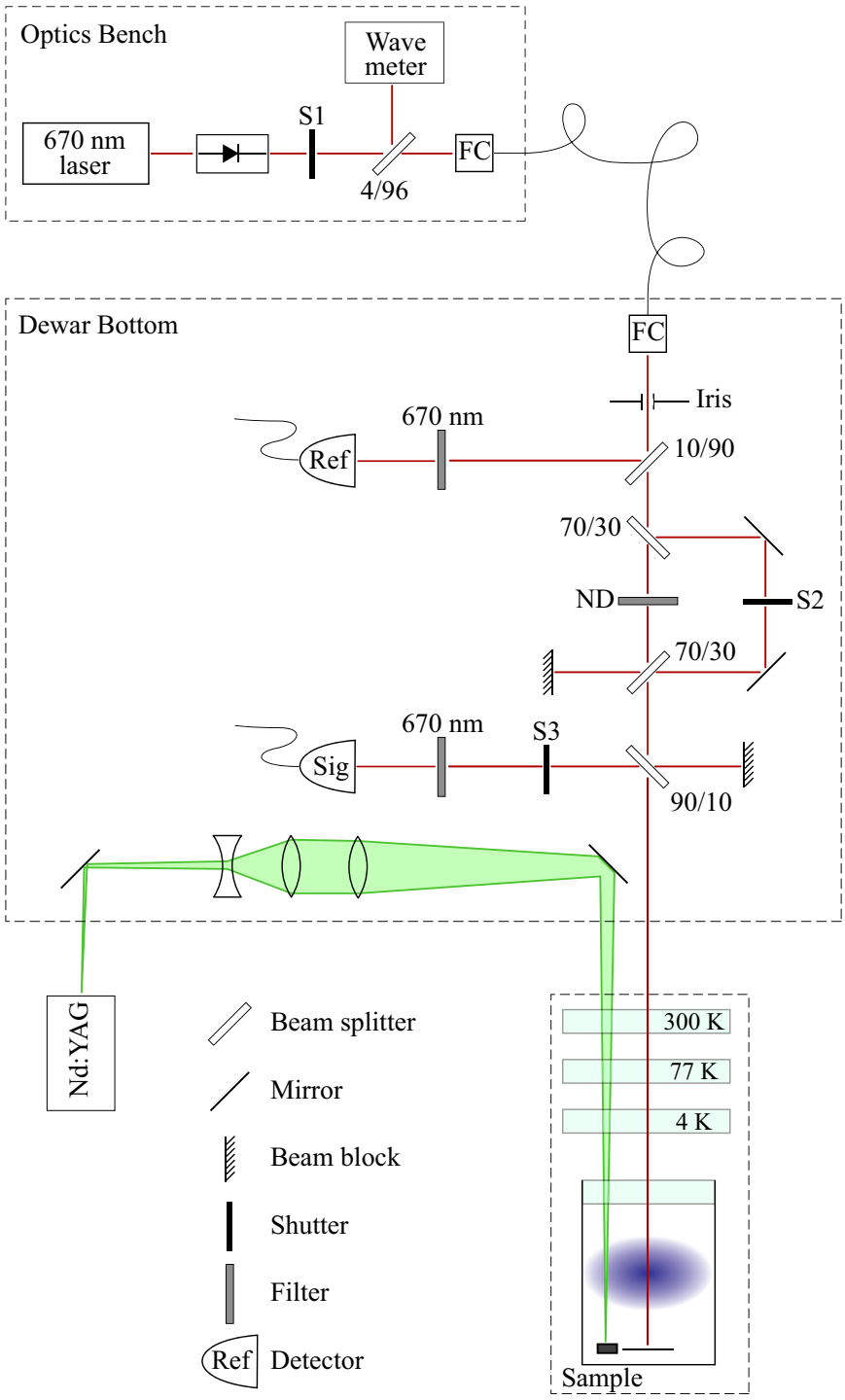

Figure 3.1: Schematic of the optical setup used for our Li experiments. Some steering mirrors have been left out. Beam splitter annotations are R/T, where R is reflectance and T is transmittance.

The laser beam is then coupled into a single-mode fiber. This fiber transports the laser light from the floating optics table on which the laser head rests to an optics breadboard bolted to the underside of our cryogenic apparatus. After exiting from the fiber, the beam passes through an iris, which is used to adjust the beam diameter. For most of the work, this iris was left fully open. After passing through the iris, approximately 10% of the beam is split off and sent into a reference photodetector. The remaining light is sent into the cell to interrogate the atom cloud. The beam is retroreflected in the cell, passing through the atom cloud a second time. After exiting the cell, the returning beam is deflected by a beam splitter into the signal photodetector. In order to get the best signal-to-noise possible, we wish to capture as much of the light that interrogates the atoms as possible. Therefore, we use a 90% reflecting beam splitter to deflect the retroreflecting beam to the signal photodetector. Each photodetector was covered with a 10 nm wide interference bandpass filter, to reduce background and noise from ambient light sources.

The laser is attenuated prior to entering the cell using a neutral density filter (and again by passing through our 90% reflecting beamsplitter), until optical pumping by the probe beam does not cause significant loss of trapped atoms. In order to obtain an optical pumping lifetime of 10 s, this requires a laser power at the atom cloud of

$$P_{\text{laser}} \leq 300 \text{ nW}, \qquad \text{for } \tau_{\text{optical pumping}} \geq 10 \text{ s}. \tag{3.1}$$

Using laser powers at the atom cloud less than 300 nW causes significant shot noise on the signal, with a noise ratio of approximately 5×10^{-3} at 300 nW. To observe the atoms for longer than 10 s, a TTL operated shutter is placed in the beam path (S1 on the schematic). Atomic spectra are taken at some small duty cycle, for 1/2 to 1 s every 10 to 30 s, and the shutter is opened only when these spectra are taken. This allows us to observe the atom cloud for up to 300 s without significant loss from optical pumping.

For some experiments we would like to use optical pumping to remove the trapped atom cloud, to obtain baseline measurements. To do this we split off a portion ($\sim 70\%$) of the probe beam before the neutral density filter. This portion is sent through a normally closed shutter (S2), and recombined with the portion that passed through the neutral density filter. In order to optically pump the atoms, we merely open this shutter for a brief ($\sim$2 s) period of time while scanning over the $\Delta m = 0, -1$ atomic transitions. To protect the photodetector from this much greater light power, we add a normally open shutter (S3) just before the photodetector. This shutter is operated on the same TTL signal as S2, so that the photodetector is blocked whenever the optical pumping light illuminates the atoms.

Depending on the experiment in question, we used photodiodes (New Focus 2001, [76]) or photomultiplier tubes (Hamamatsu R2557, [79]) as our photodetectors. Photodiodes were used when we had high light powers on the photodetectors. This was the case in our first Li experiment, where we did not worry about optical pumping. In the second and third experiments we used PMTs, although a photodiode was used for the reference detector for a portion of the second experiment. This was changed to a PMT later, to match the noise response of the reference detector with that of the signal detector.

3.1.2 Spectroscopic method

To calculate physical parameters such as atom number, temperature, and state distribution, we compare the power of the probe beam after passing through the atom cloud ("signal") to the power of the probe beam before passing through the atom cloud ("reference"). The comparison is made by dividing the powers measured on the corresponding signal and reference photodetectors. By doing this we eliminate common mode noise from amplitude fluctuations in the laser. The absorption A of the probe beam by the atom cloud,

at laser frequency ν, is proportional to this division, with

$$A(\nu) = 1 - \frac{1}{B(\nu)} \frac{P_{\text{signal}}(\nu)}{P_{\text{reference}}(\nu)}. \tag{3.2}$$

Here $B(\nu)$, called the "baseline", represents the laser attenuation by all optics between the reference pick off and the photodetectors. Its value is such that $A = 0$ when no atoms are present in the trap. It is easily measured by simply taking measurements of the signal and reference detectors in the absence of trapped atoms. Due to etaloning within the optics, the baseline will in general be slightly dependent on frequency (in practice the baseline varies by about 10% over the frequency range of interest).

We then calculate the "optical density" as a function of laser frequency, where the optical density is

$$OD(\nu) = -\log(1 - A). \tag{3.3}$$

The optical density is proportional to the number of atoms in the probe beam that absorb a photon of frequency ν. We scan the frequency of the laser rapidly (between 50 Hz and 200 Hz), taking an optical density spectrum with each scan period. The laser is scanned by sending an oscillating voltage to the scan control input of the laser controller. Fig. 3.2 shows an example laser scan. The upper plot shows the scan function sent to the laser controller. The lower plot shows the raw division of the signal photodetector signal over the reference photodetector signal. Note that the laser frequency lags the scan voltage. This can be seen by observing when the turning point in absorption occurs, vs. the turning point in scan voltage. To determine the dependence of laser frequency on control voltage, we measure a known atomic spectrum (zero field Li, in this case), then use the published atomic structure [37] to determine the laser frequency as a function of voltage.

The measured optical density spectra are compared to spectra simulated from the Li atomic structure, parameters of the probe beam, and the number, temperature, and

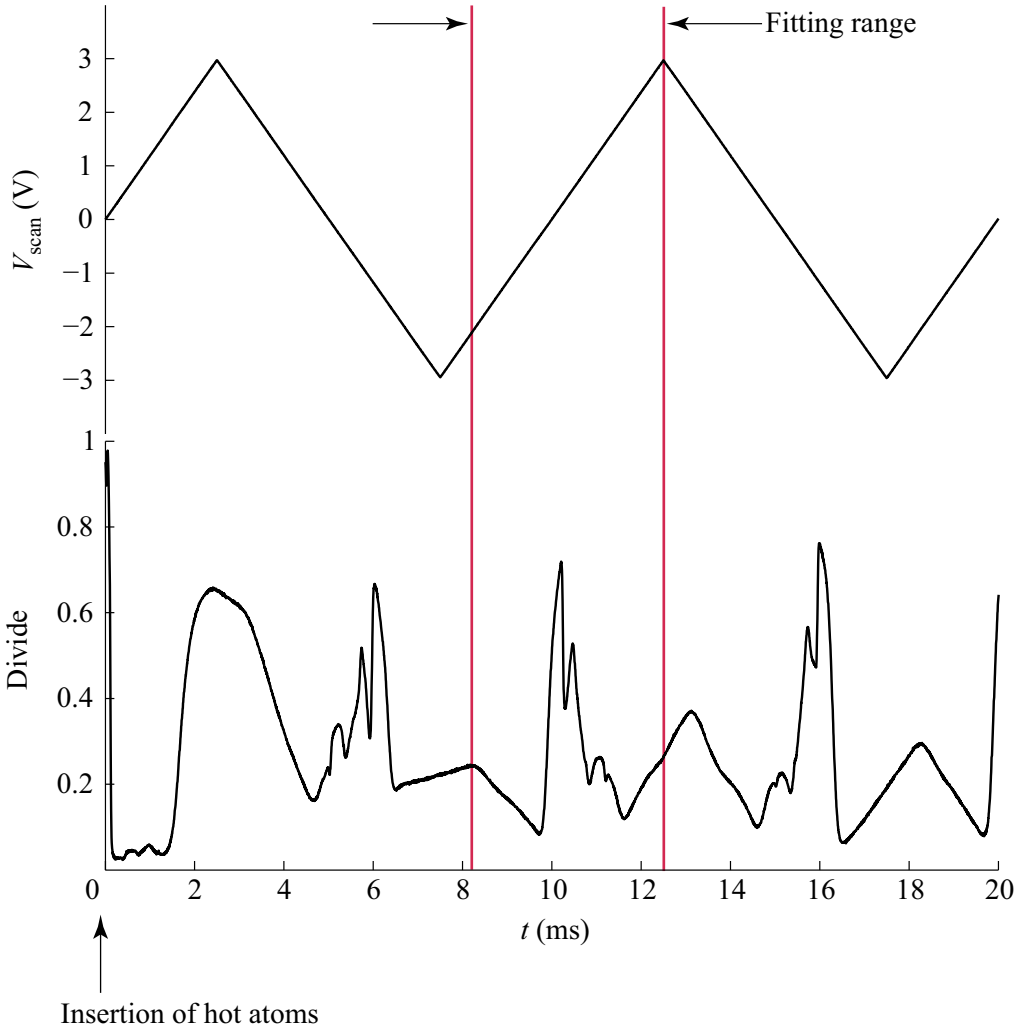

Figure 3.2: The upper plot shows the scan voltage sent to the laser controller. The lower plot shows the observed Li spectrum (this particular spectrum was taken with Li atoms in a 3.6 T trap). Hot atoms are injected into the experiment at $t = 0$. The frequency of the laser lags the scan voltage. Spectrum fits are performed using the data from each scan after the frequency turning point.

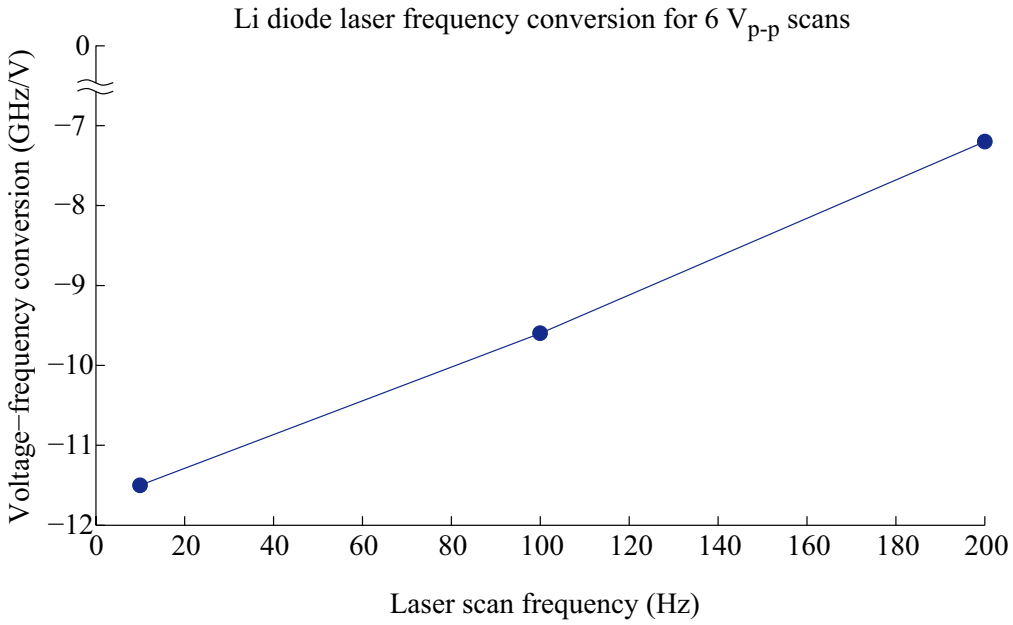

Figure 3.3: Li laser voltage to frequency conversion, for 6 V peak-to-peak scan amplitudes, vs. scan frequency.

state distribution of the atomic cloud. By performing a χ^2 fit of the simulated spectra to the observed spectra, we can extract the parameters of the trapped atoms, along with confidence intervals for these parameters. This process is described in detail in Appendix A. To deal with the frequency delay of our laser, we simply exclude an initial portion of each spectrum, corresponding to this delay, from each fit.

3.1.3 Li atomic structure

In order to simulate the optical Li spectrum, we must know the energy dependence of the ground and excited energy levels of Li, as well as the transition rates between these levels. This structure was calculated according to the prescription in App. A, using atomic structure coefficients taken from the literature. Center-of-gravity energies, Landé g-factors, and fine structure coefficients of the $1s^2 2s$ and $1s^2 2p$ levels of ^{7}Li were taken from [37]. The Einstein A coefficient [25] for the transition was also taken from [37]. Hyperfine coefficients

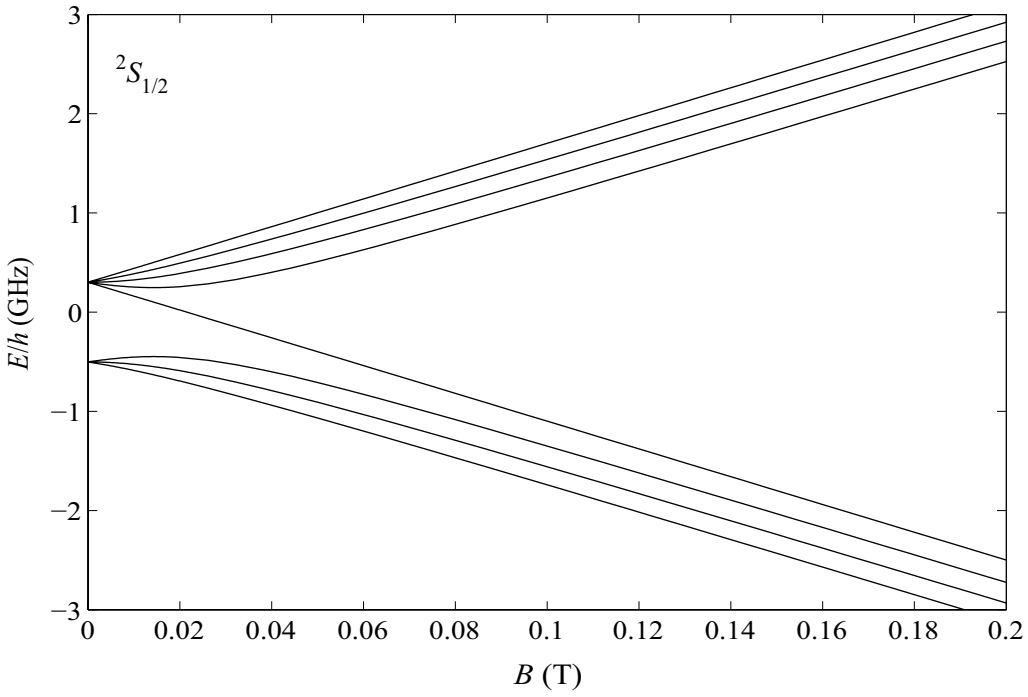

Figure 3.4: Energy levels of ground state $1s^2 2s$ Li.

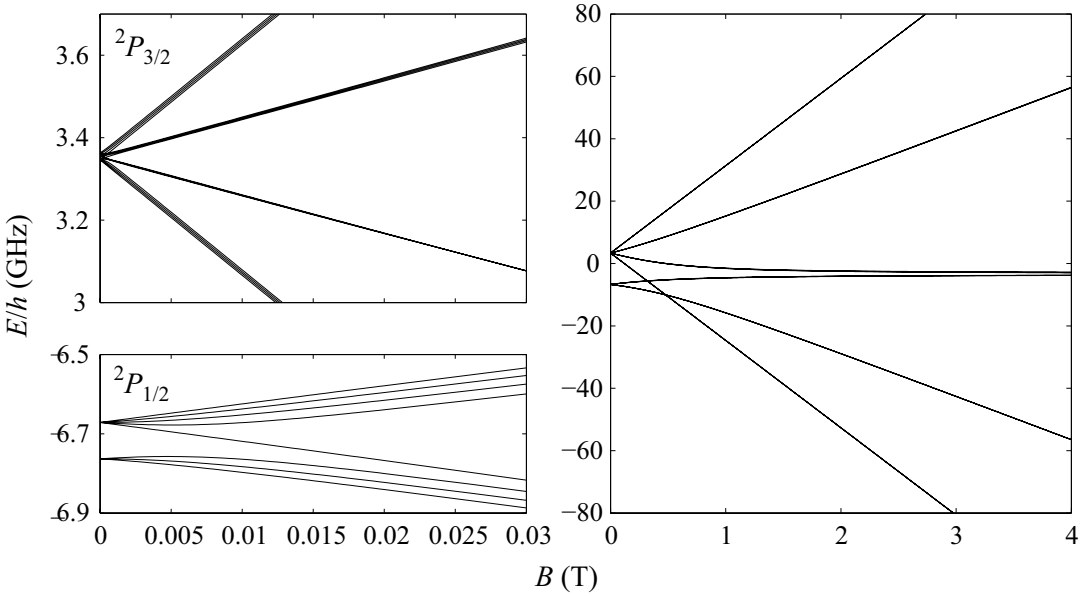

Figure 3.5: Energy levels of excited state $1s^2 2p$ Li. The two plots on the left show low field behavior of the $^2P_{3/2}$ (upper plot) and $^2P_{1/2}$ (lower plot) states. At fields less than 0.3 T, J is a good quantum number. The plot on the right shows the field behavior up to 4 T. Between 0.3 T and 0.5 T we see avoided level crossings. At high field the Paschen-Back effect lifts the $\vec{\mathbf{L}} \cdot \vec{\mathbf{S}}$ coupling, and m_l and m_s are the good quantum numbers.

were taken from [80]. The calculated Zeeman energies of the ground and excited state manifolds are shown in Figs. 3.4 and 3.5. The Zeeman energy of excited state Li is rather unique, because the strength of the Zeeman interaction can overcome the fine structure $\vec{\mathbf{L}}\cdot\vec{\mathbf{S}}$ interaction at fields that exist within our magnetic trap.

We typically ignore contributions to the atomic spectrum due to ^{6}Li, as the natural abundance of this isotope is only 5%. However, we did calculate the Zeeman energies and transition probabilities between ground and excited state ^{6}Li. The results are similar to those for ^{7}Li, with the major change being the hyperfine degeneracy, as ^{6}Li has $I = 1$ compared to $I = 3/2$ for ^{7}Li.

3.2 Shared apparatus

Each of our lithium experiments shared the same general cryogenic apparatus, with the different abilities of each experiment implemented by modifying the cell and valve apparatuses. A schematic of the general cryogenic apparatus, minus the cell and valve components, is depicted in Fig. 3.6. The experiments are housed within a triple wall cryostat. Within this cryostat we have inserted an Oxford Instruments Kelvinox 400 [81] dilution refrigerator [52]. The refrigerator has a measured cooling power of 31 mW/K^2, and a base temperature of 16 mK[1] when disconnected from any heat loads. Hanging from the lower third of the fridge is a vacuum can, called the "inner vacuum chamber", or IVC. Our cell and valve apparatuses were contained within this IVC. The IVC is extended by a brass tube. This tube fits inside the bore of the magnet and extends the IVC vacuum within the trapping region, where the experimental cells are located. The bottom of this extension is mated to the bottom of the cryostat bath using an edge-welded bellows, making

[1] As measured via nuclear orientation thermometry.

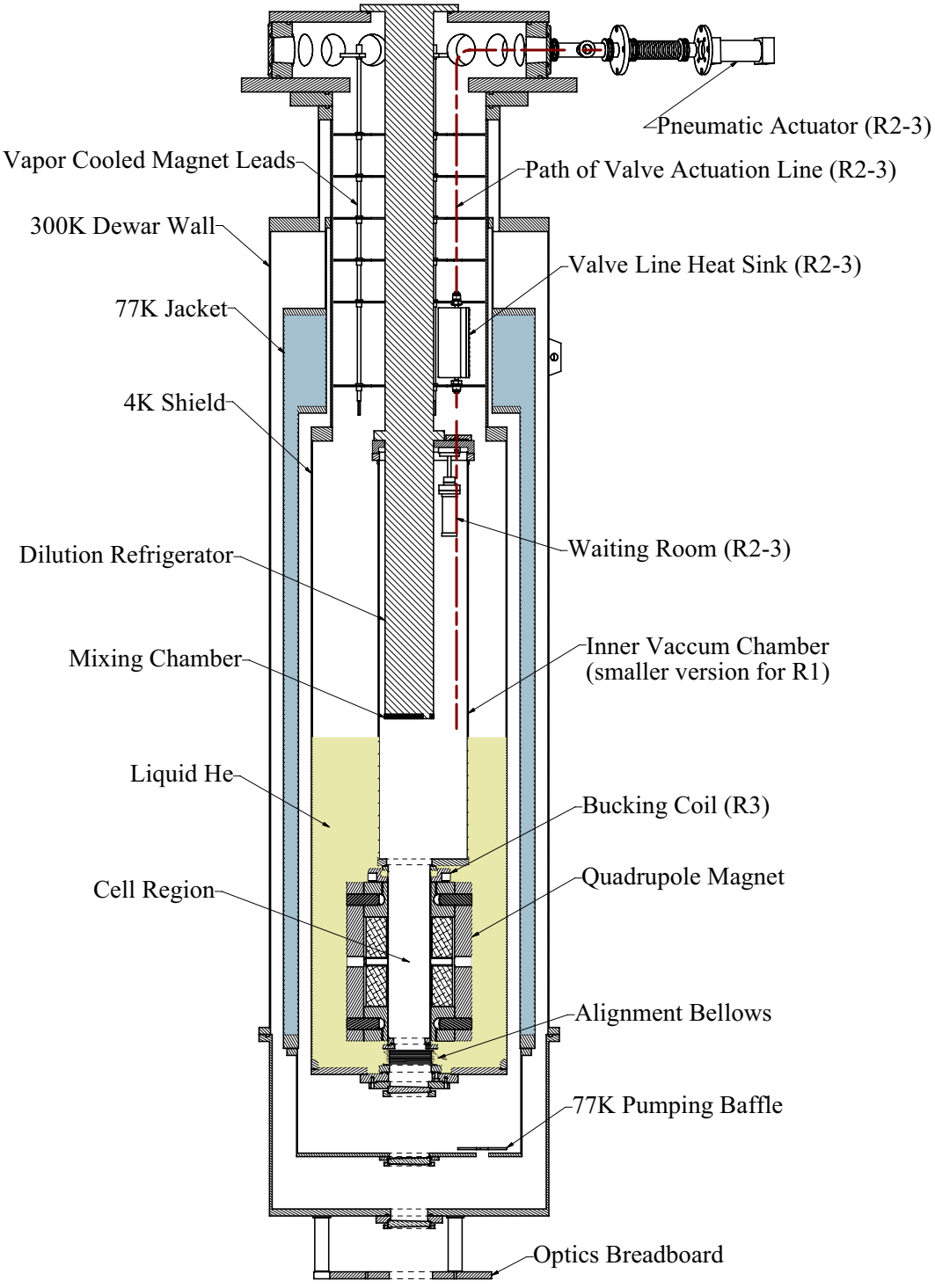

Figure 3.6: General cryogenic apparatus schematic. Items marked with Rx only appeared in run: R1) test run, R2) valve run, R3) evaporative cooling run. The cell, much of the valve actuation, bus bars, magnet supports, and transfer plumbing are not shown.

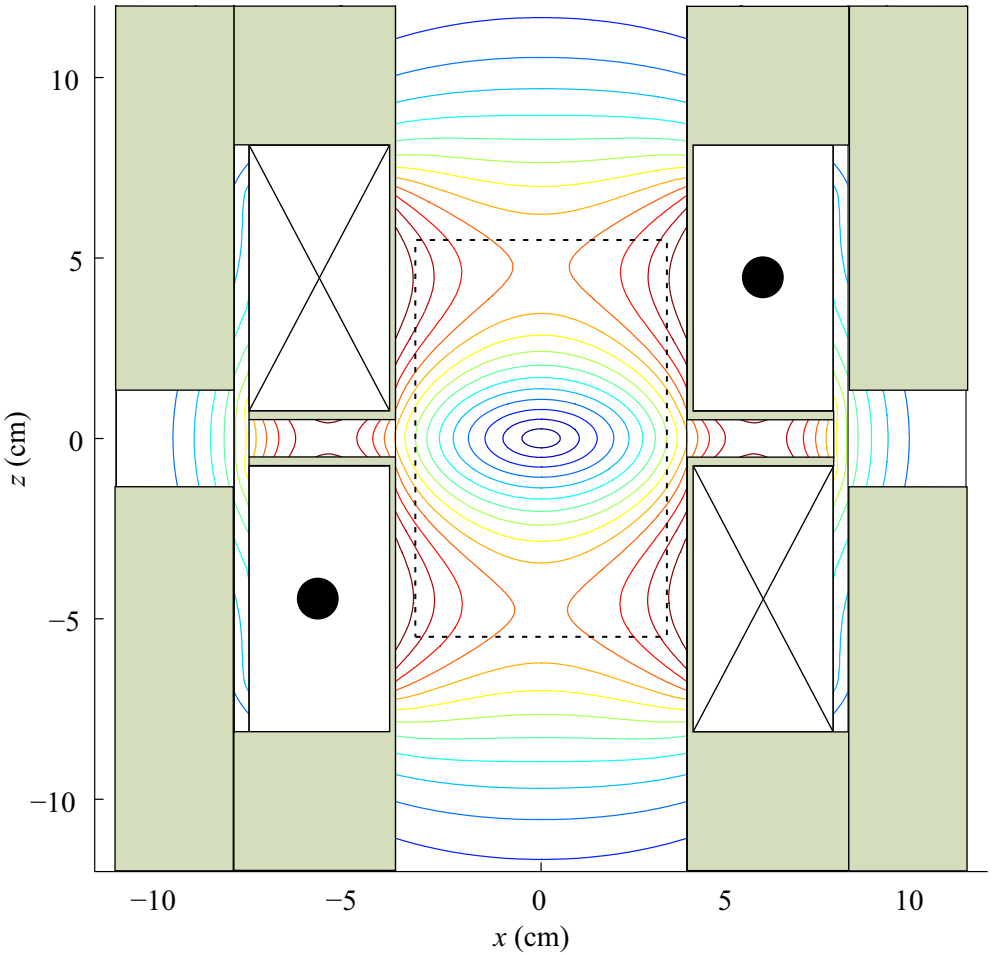

Figure 3.7: Schematic of the superconducting magnet. Field contours are every 0.5 T, with a current of 100 A in each magnet coil. The dashed rectangle is the inner dimension of the cell walls.

up for misalignment of the bath and the fridge. A set of borosilicate glass windows allows optical access from the bottom of the cryostat into the cell. The window closest to the cell makes a seal between the IVC and the cryostat guard vacuum. This is done to prevent stray helium gas that may enter the guard vacuum from creating a superfluid film on the dilution refrigerator.

Trapping magnet

The superconducting magnet is similar to the "Mark V" magnet described in [20]. Current is delivered to the magnet via a set of vapor cooled leads [82] and composite copper/superconductor bus bars. The magnet was designed to be run with up to 96 A in each coil with the coil currents running in opposite directions (i.e., the magnet is run as an anti-Helmholtz magnet). The magnet can in practice be run at currents up to 101 A in each coil without causing the coils to go normal.[2] For safety we consider the maximum current of our magnet to be 100 A in each coil. Because the in-coil fields add when the magnet is run in a Helmholtz configuration, the current limit is only 80 A when the coil currents run in the same direction.

A minimum amount of distance is needed between the inner diameter of the magnet and the inner wall of the trapping cell. This distance includes the thickness of the IVC extension, a 1.5 mm vacuum clearance between the IVC extension inner diameter and the outside of the cell, and the thickness of the cell wall itself. For our thinnest cells (0.080 in wall thickness), 100 A in each magnet coil corresponds to a minimum trapping field at the cell wall of 4.0 T. This is equivalent to a trap depth of $U_{\mathrm{trap}}/k_B = 2.7$ K, for $1\mu_B$ species.

For the evaporative cooling experiment, we bolt a home-wound bucking coil to the top of the magnet. This coil is run in series with the top magnet coil, but wired such that the current direction is opposite that of the top magnet coil. The geometry of this coil was chosen to eliminate fields near the copper and brass parts of our evaporative cooling cell and the refrigerator mixing chamber. A complete description of the bucking coil is given in Newman's thesis [71].

[2]It is possible the real current limit is higher. The magnet quenched once when operating at 101 A, but we believe this was due to a problem with our Lakeshore Supply which has since been fixed.

Ablation laser

For each of our experiments, a gas of Li was produced via laser ablation of either Li metal or LiH salt. To install the Li metal samples in our cells, we performed the final assembly of the cells in a glove box containing an argon environment. Light for laser ablation is produced from a Continuum Minilite II 532 nm Nd:YAG laser [83], with pulse energies up to 25 mJ and pulse widths of 5 ns.[3]

For the first two experiments, the ablation laser was focused on the Li targets by inserting a lens in the ablation beam. For the thermal isolation experiment, we first used a telescope to broaden the YAG beam to a ~ 0.8 in waist, then focused the beam. This increases the numerical aperture of the focusing lens, allowing for a tighter focus on the face of the Li sample.

3.3 Test experiment

For our test experiment we used a simple copper cell, shown in Fig. 3.8. The cell is suspended from the refrigerator mixing chamber by a copper heat link. A standoff ring [57, Chap. 5] prevents the sub-Kelvin cell from contacting the 4 K IVC extension. The heat link is a 0.53 in diameter, 10 in long OFE copper rod. Our mixing chamber in this setup had a base temperature of ~ 130 mK. In steady state, the cell resided at a temperature 30 mK warmer than the mixing chamber. To heat the cell to the 300 to 400 mK required to obtain a significant ^{3}He vapor density, we applied a 1 s long 2 to 3 V heater pulse. The cell

[3] In order to synchronize our data collection with the ablation, we fired the YAG via a remote trigger, generated by our data acquisition routine. Despite being supposedly designed for remote triggering, the Minilite will episodically go into a mode in which it is unable to accept further triggering without manual intervention. We therefore recommend against using the Continuum Minilite for laser ablation in buffer gas cooling experiments. If the Minilite is used, this problem can be alleviated by sending a "maintenance pulse". To perform a maintenance pulse, the flashlamp trigger signal is delivered to the YAG; after a long delay (>400 μs, such that no excited Nd ions remain) the q-switch is triggered. This pulse should be sent to the YAG every 30 s or so.

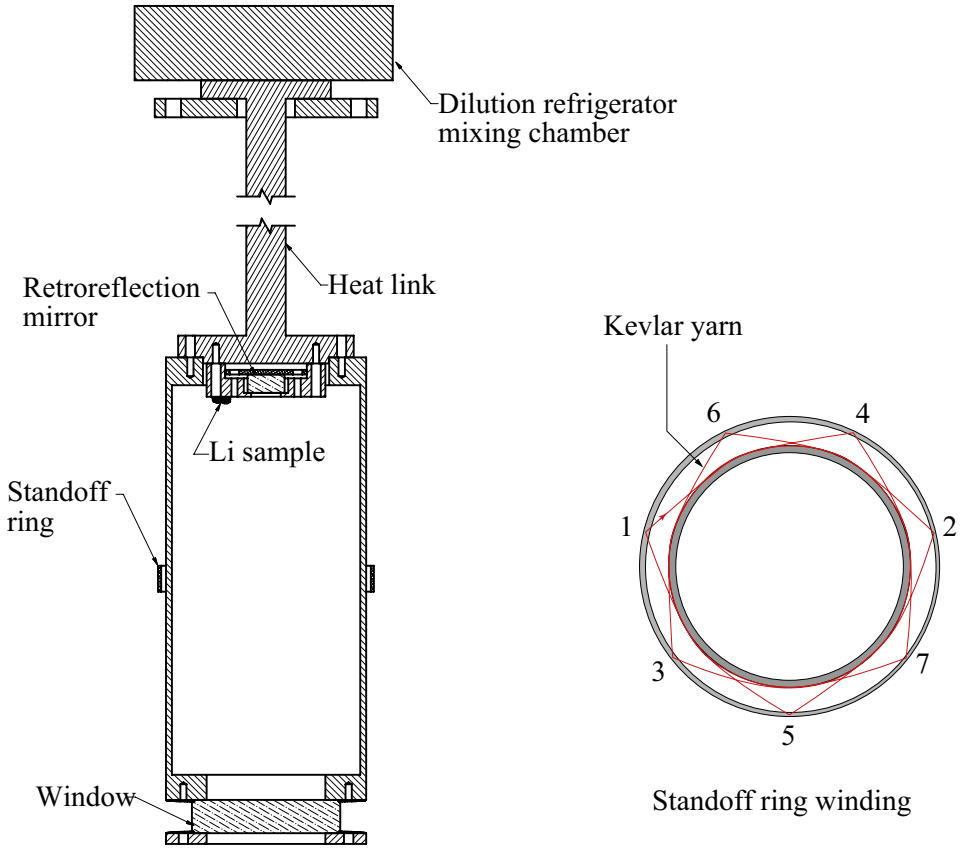

Figure 3.8: Lithium test cell. The inset shows how the standoff ring is attached to the cell with kevlar yarn, with the yarn wound clockwise, attached to the standoff ring in the order indicated by the numbers in the figure.

was run in this mode of operation, until bad vacuum in the IVC caused the mixing chamber temperature to rise drastically. After this point the mixing chamber base temperature was 440 mK, and we ran without a heater pulse.

Buffer gas was delivered to the cell by a capillary fill line. To set the density of buffer gas in the cell, we would meter a fixed amount of room temperature He, then allow this helium to expand into the cold cell. Because the cell is 1000 times colder than room temperature, almost all this buffer gas ends up in the cell.

Fig. 3.9 shows the Li spectrum we measured in our test cell at zero field. This was taken after the magnet had been ramped to full field a couple times; therefore, trapped currents could cause broadening of the zero field lines. We use this scan to calibrate the laser's voltage to frequency conversion. This conversion is shown in Fig. 3.3. Our fit to this scan gives 2×10^{11} atoms in the cell, thermalized to the buffer gas. However, we took other scans (at higher buffer gas densities) displaying up to 10^{13} atoms.[4]

We then raised the trapping field. A sample spectrum of Li in our trap, taken directly after ablation is shown in Fig. 3.10. Initially, the atoms do not lie in a true Maxwell-Boltzmann distribution. Good fits to a model that presupposes a Maxwell-Boltazmann distribution are therefore difficult to obtain at short times after ablation. After a trap lifetime these fits become much more accurate.

To determine the lifetimes of atoms in our trap, we could fit the optical density spectra, taken each laser scan period, for atom number. Such a sequence of spectral fits is shown in Fig. 3.11. We would then fit the atom number vs. time to determine the atom lifetime. However, this method is prohibitively time consuming to execute on many ablations. If our laser did not drift between ablations, we could average the spectra over many

[4]The plotted scan is chosen because it is the only scan taken in the test run that shows all the peaks in the transition.

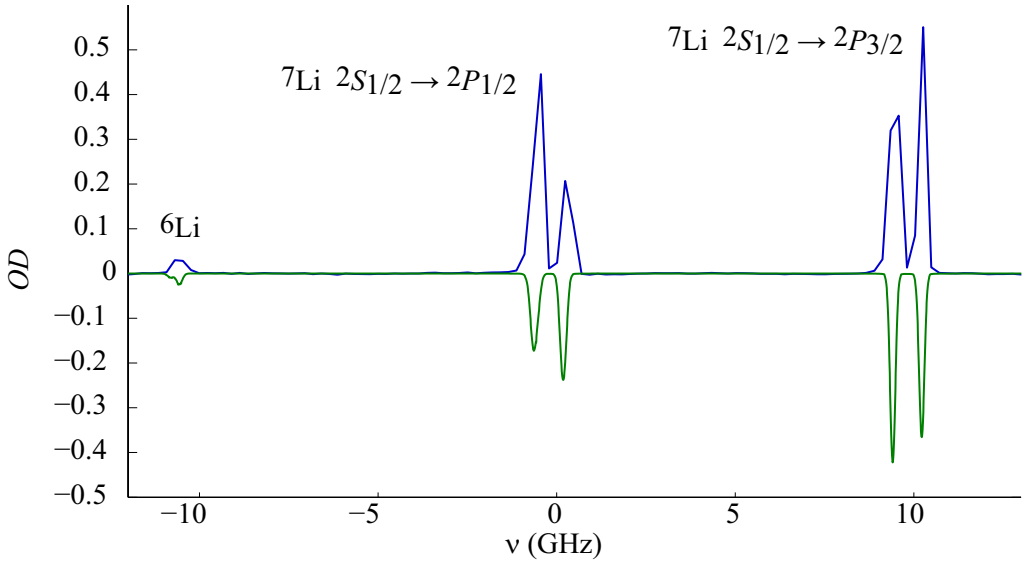

Figure 3.9: Spectrum of Li at 0 field in our test cell. Data are plotted on the positive axis, simulated spectrum is on the negative axis.

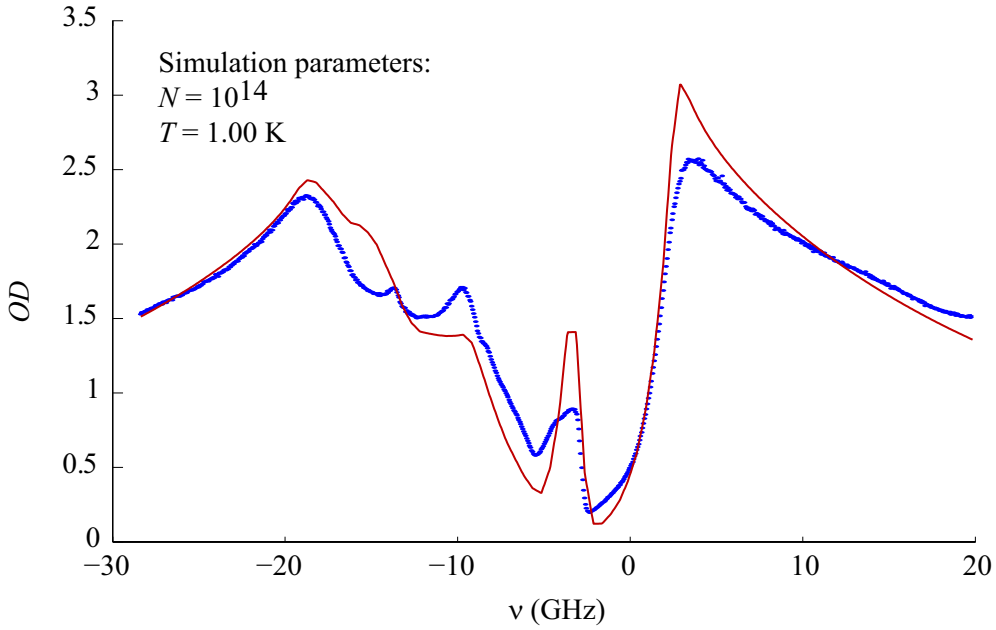

Figure 3.10: Spectrum of Li in our test cell, with 90 A in the magnet coils (2.4 K trap depth), taken directly after ablation. $n_b \approx 3 \times 10^{15}$. Fits are generally bad directly after ablation, and improve after 0.5 s. The probe beam was off-axis by 3 mm in our test experiment scans, leading to smoothing of the spectral features.

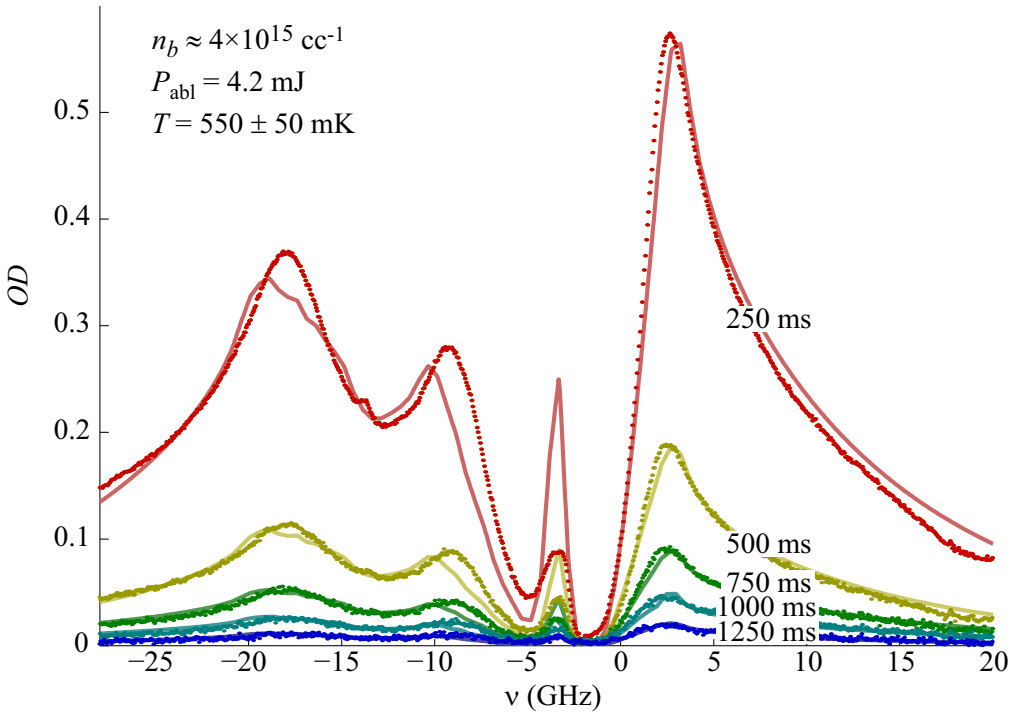

Figure 3.11: Successive fits to Li spectra in our test experiment for an example ablation. Times are time after ablation. Each spectrum is an average of 25 ms of data (3 scans). The quoted temperature is taken from the spectral fits.

identical ablations, and fit each averaged spectrum. However, the laser center frequency drifts, on the order of 200 MHz/min. In addition, other experimental parameters such as cell temperature drift with time.

To easily fit lifetimes we instead make fits to the decay of the spectra optical density. This is validated by the following argument: If we assume that the atoms are in a Maxwell-Boltzamnn distribution, and additionally that the Zeeman interaction is close to linear, then from (A.24) and (2.9), we find that the total atom number is proportional to the integrated optical density of the spectrum:

$$N(t) \propto T^2 \int d\nu \, OD(\nu, t). \tag{3.4}$$

If the temperature of the atoms does not change during the time we wish to measure

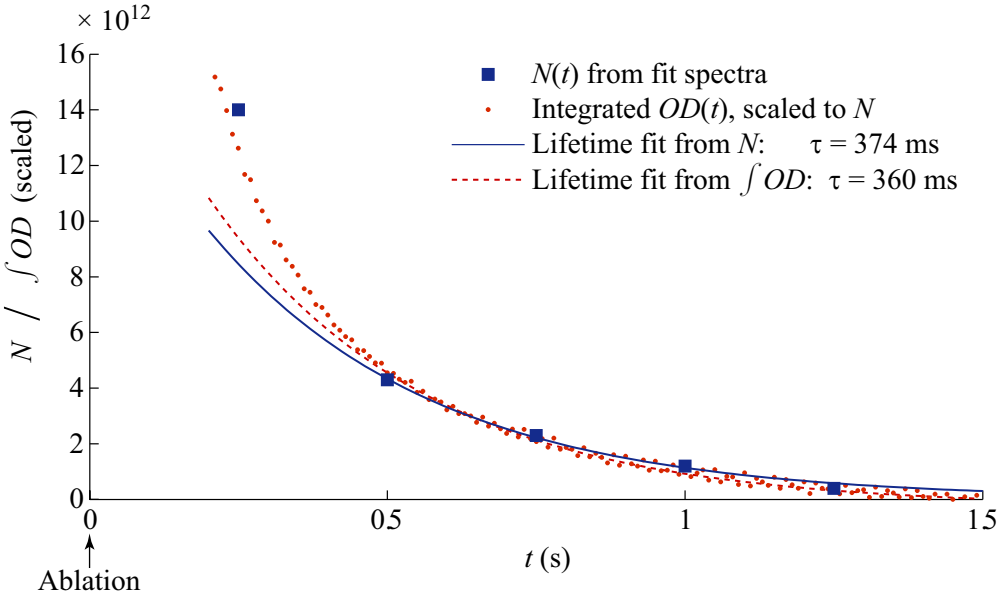

Figure 3.12: Time profile and atom lifetimes for the example ablation of Fig. 3.11. Lifetimes are fit after 500 ms.

the atom lifetime, we can then calculate the atom lifetime by fitting an exponential to $\int d\nu\, OD(\nu, t)$. We find in general that these two approaches yield similar results, as is shown in Fig. 3.12.

Despite the hot temperatures we ran with in this experiment, we were able to observe Li lifetimes up to 350 ms at ^{3}He buffer gas densities between 3×10^{15} and 10^{16} cc^{-1}. Lifetimes were limited by drift-diffusion (see §2.2.2). These numbers are in rough agreement with our $M = 7$ amu Monte-Carlo predictions at 500 mK, assuming an elastic Li-^{3}He cross-section of 10^{-14} cm^2 (see §2.3.5). This gave us faith that if we could design our next experiment such that the Li could be loaded at 350 mK, and we could tune the pump-out trajectory of our cryogenic valve, we would be able to reduce the background gas density below the valley of death, while keeping a significant fraction of our trapped Li sample.

3.4 Buffer gas pump-out experiment

In our second experiment, we wished to demonstrate that we could successfully remove buffer gas from the cell, to the point that the lifetime of trapped Li was not limited by elastic collisions with the background gas.

3.4.1 Apparatus

Because obtaining a low cell temperature was crucial for this experiment, we chose to use a copper cell. Having this copper cell would give good thermal conductivity down the length of the cell; however, due to eddy current heating, having a copper cell would prevent us from changing the depth of the trap while Li remained in the trap. A drawing of the apparatus is shown in Fig. 3.13.

The cell is composed of two chambers: a lower trapping chamber and an upper pumping chamber. These two chambers are attached by an indium seal. The vacuum spaces of these two chambers are separated by a high conductance cryogenic valve.

The lower trapping chamber has a volume of 300 cc. At the bottom of this chamber is a BK7 window, located at the lower saddle point of the magnetic field. At the top of the chamber is our copper sample holder, located about 1 cm above the upper saddle point of the magnetic field. Our retroreflecting mirror is clamped to the middle of this sample holder. Our samples are glued to the bottom of our sample holder using Stycast 2850 epoxy.

The pumping chamber contains 15.3 gm of activated coconut charcoal. Coconut is chosen for its small pore size, yielding enhanced pumping of helium vs. other charcoals [84]. This charcoal is thermally anchored to the cell wall. The active area of the charcoal is 200 cm^2, giving a pumping speed for 350 mK ^{3}He of 80 L/s.[5]

[5]This assumes that the He has a 30% chance of sticking to the charcoal surface.

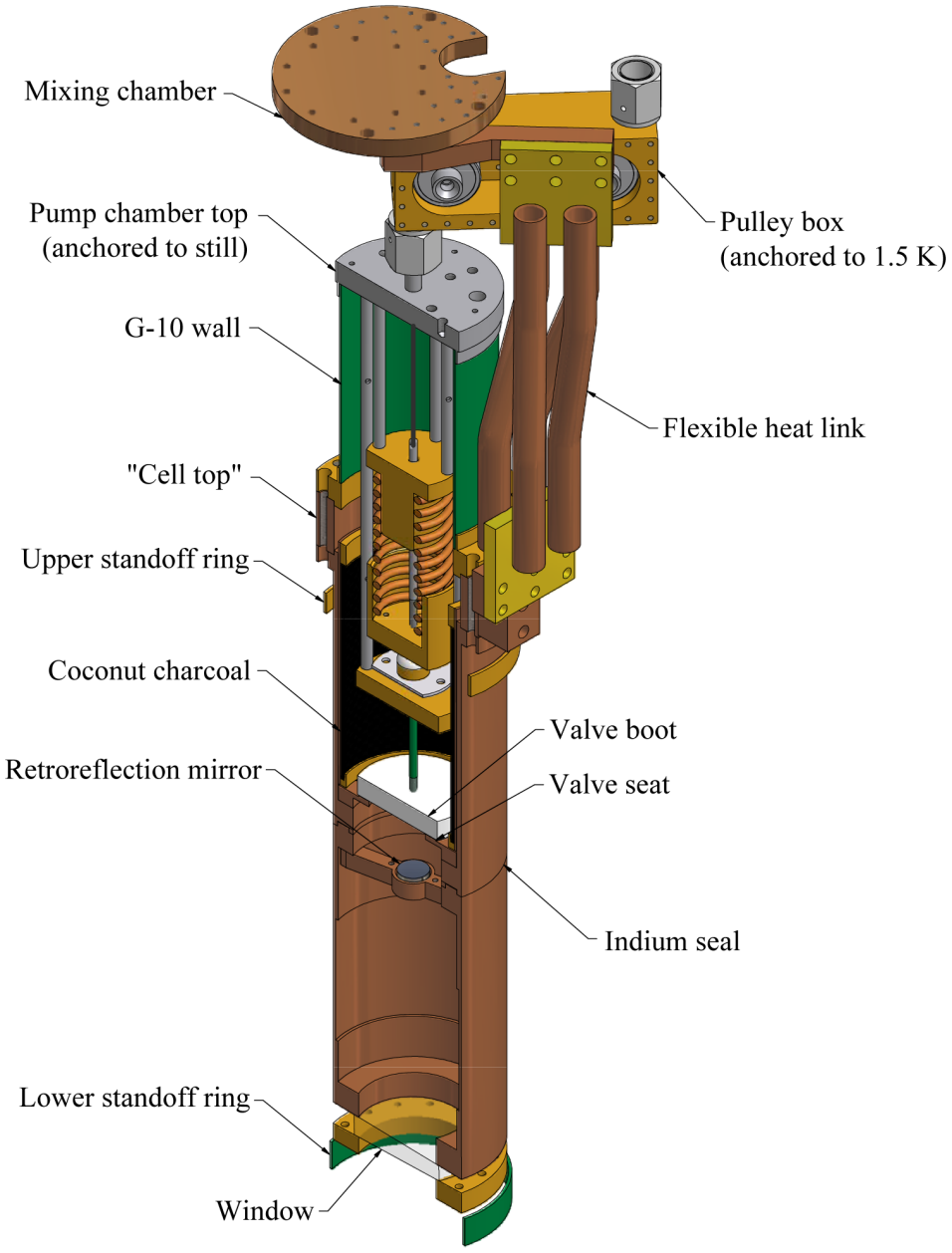

Figure 3.13: Apparatus used for the buffer gas pump-out experiment. Note that the pulley box is attached only to the pump chamber top, and contacts neither the mixing chamber nor the heat link. The fill line is not shown.

Cryogenic valve

In order to ensure that we remove buffer gas with a τ_{pump} much faster than the valley of death lifetime for 350 mK Li, we chose a valve diameter of 3.6 cm. This gives a valve open conductance of 12 L/s for 350 mK ^{3}He. Because the valve open conductance is significantly less than the charcoal pumping speed, the valve limits the speed at which we remove buffer gas. For the 360 cc trapping chamber we used, our 12 L/s valve conductance translates to a τ_{pump} of 30 ms. This is more than twice as fast as the 80 ms valley of death lifetime for 350 mK Li (see Fig. 2.6).

To both load buffer gas in the trapping chamber and to keep the buffer gas during Li loading, the valve must seal reasonably well. Because the valve is opened on a ~ 300 ms time scale, we require at a bare minimum that the valve retain the buffer gas for at least a few seconds. The actual measured loss time for ^{3}He from the cell with our valve is 24 minutes, limited not by the impedance of the closed valve, but by the buffer gas loading impedance (described in the next section). Our valve has a measured 4 K conductance of 3×10^{-5} L/s, corresponding to a buffer gas decay time of 5 hrs. Our long hold time allows us to perform many diagnostic experiments without worrying about non constant buffer gas densities.

Because dilution refrigerators are notoriously fragile, we wished to minimize the amount of force we applied to the cell in order to seal the valve. In addition, our cryostat design restricted us to locating our cell directly beneath the dilution refrigerator. These two constraints prevented us from using the direct valve actuation method (i.e., pushing the valve closed with a rigid rod, from room temperature) used in previous valved buffer gas experiments [58]. The process to design a cryogenic valve that would meet all the criteria listed here was rather involved; it is described in full in App. B. The end result is shown in Figs. 3.13 and B.2.

The valve we designed is actuated using a stainless steel wire pull rope. Pulling on this rope opens the valve; upon releasing the rope the valve is closed by a spring located within the pump chamber. The rope is contained within a 0.25 in diameter, 0.035 in wall stainless steel tube. The rope pulls against this tube: because the length of the tube is fixed, the opening and closing forces are contained within the cell, tube, and wire rope. This results in a minimum transmission of force to the IVC and hence the dilution refrigerator (measured to be a few ozs., but still enough to cause a slight torque on the cell). We use a pneumatic actuator to pull the rope. This pneumatic actuator consists of a piston; compressed gas is put on each side of the piston. We keep a static 80 psi on the bottom of the piston. To close the valve, we put 100 psi above the piston. This volume "above the piston" is attached to a high-conductance solenoid valve. When this solenoid valve is activated, the 100 psi gas is discharged, and the valve opens. With these gas pressures, our valve opens in 34 ms. By placing a constriction past the solenoid valve, we can slow the discharge of the above-the-piston gas, reducing the valve opening time.

Waiting room and loading impedance

Because we would need to rapidly replace buffer gas in the cell after every valve opening, we added a "waiting room" to store buffer gas in a charcoal sorb between buffer gas loadings (similar to the waiting room described in [58, pp. 121-5]). This waiting room (shown in Fig. 3.6) was suspended from the top of the IVC via a brass heat link. This heat link was designed such that the temperature of the waiting room could be increased to up to 20 K using one to two Volts applied to a resistive 15 Ω heater, but still be cooled to the 4 K temperature of the IVC within a few seconds when no heat was applied. Inside the waiting room we put 1.34 gm of the same coconut charcoal used in the pumping chamber. This amount of charcoal can hold ≈ 0.1 gm of He gas [52], or enough gas for 7000 loadings

of the cell at $n_b = 10^{16}$ cc^{-1}.

The waiting room is connected to the cell trapping chamber by a high gas conductance 3/8 in diameter thin-walled stainless steel tube. This tube is heat sunk to the dilution refrigerator 1 K pot and still, at points between the waiting room and the cell; this results in a negligible heat load on the cell by the waiting room. Between the end of this tube and the trapping chamber of the cell we insert a tuned impedance. The value of the impedance is chosen to give a long lifetime of buffer gas within the cell while allowing loading of the cell on reasonable time scales. We chose an impedance of 4×10^{-4} L/s, obtained by sending the gas through a 20 mil diameter, 0.25 in long tube. This gave us a buffer gas hold time in the cell of 24 min. Note that the impedance must have a larger conductance than the closed valve, if we are to successfully load buffer gas into the cell.

To load buffer gas into the cell, we first opened a metered amount of room temperature gas to the waiting room volume. We would typically load 10 STP mL of ^{3}He into the waiting room. This gas would be pumped by the cold charcoal within the waiting room, and most would end up absorbed into the charcoal. Some would make it into the cell; this would be removed by opening the valve and heating the cell to 400 mK. Buffer gas could then be loaded into the cell from the waiting room by heating the waiting room for some amount of time. The exact parameters depend on the amount of ^{3}He absorbed into the charcoal, but a typical buffer gas load would involve raising the waiting room sorb to 10 K for 90 s. The desorbed gas leaks through the loading impedance for the time the waiting room remains hot. We then wait for the waiting room to cool to near 4 K; this pumps the desorbed gas from the fill line, ensuring that we have no gas leaks into the cell during the experiment. To measure the amount of loaded buffer gas, we measure the lifetime of atoms diffusing in 0 field. This lifetime, when combined with the cell temperature as measured by our cell thermometer, is input into the zero-field diffusion lifetime equation (2.29) to

determine the diffusive mean free path. For all our buffer gas measurements, we assume a Li-^{3}He diffusion cross-section of 3×10^{-15} cm^2. This is based on a calculation performed by Dalgarno [70].

Flexible heat link

We also payed special attention to the thermal statics and dynamics of the apparatus. Because we wished to mechanically divorce the cell from the dilution refrigerator insert, we constructed a flexible heat link to thermally connect the cell to the mixing chamber. One can imagine two different methods for constructing a flexible heat link. In the first method, the heat link would be constructed of narrow metallic wires or foils. The flexibility is provided by introducing some amount of slack in the wires or foils. In the second method, the heat link is provided by superfluid ^{4}He. The link is made flexible by containing the liquid ^{4}He in a flexible tube. Superfluid He heat links have been successfully used in buffer gas trapping experiments before [57]. Because the thermal conductivities [52] of superfluid He and of copper have different power law dependences on temperature, the best heat link method to use will depend on the operating temperature of the experiment. The conductivity of superfluid ^{4}He is $\sim T^3$, while the conductivities of most metals go as T. For 101 OFE copper, with a typical residual resistivity ratio (RRR, the ratio of electrical conductivity at 4 K vs. 300 K) of 150, the conductivity is greater than the conductivity of superfluid ^{4}He for temperatures less than $\approx$ 200 mK [52]. Because we wished to maintain high thermal conductivity at temperatures as low as 100 mK, we chose to make a flexible heat link from copper.

The first iteration of this heat link is depicted in Fig. 3.14. The heat link was composed of 500 0.5 mil thick $\times$ 1 in wide OFE Cu foils. These foils were stacked one on top of another; this stack was then bolted to a clamp on either end; the lower clamp was

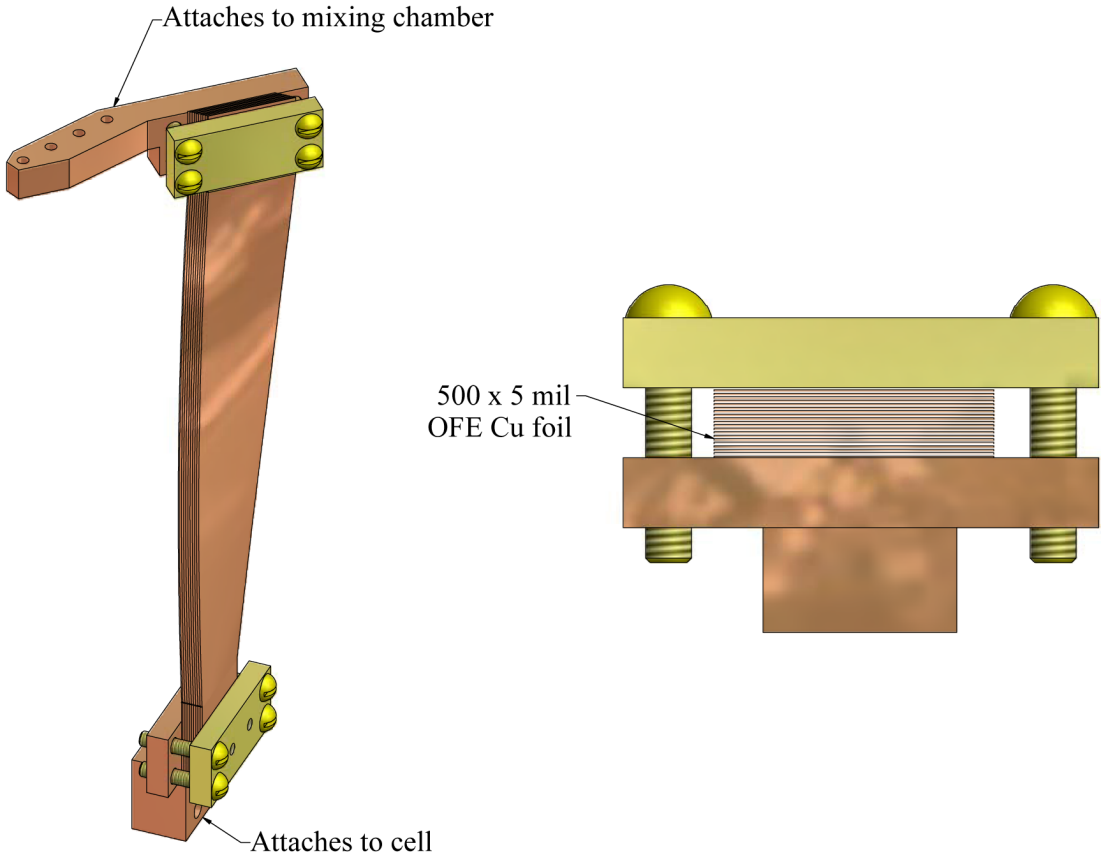

Figure 3.14: Our first, failed, flexible heat link design. The entire heat link as assembled is shown on the left. The right shows how the copper foils were stacked and compressed together.

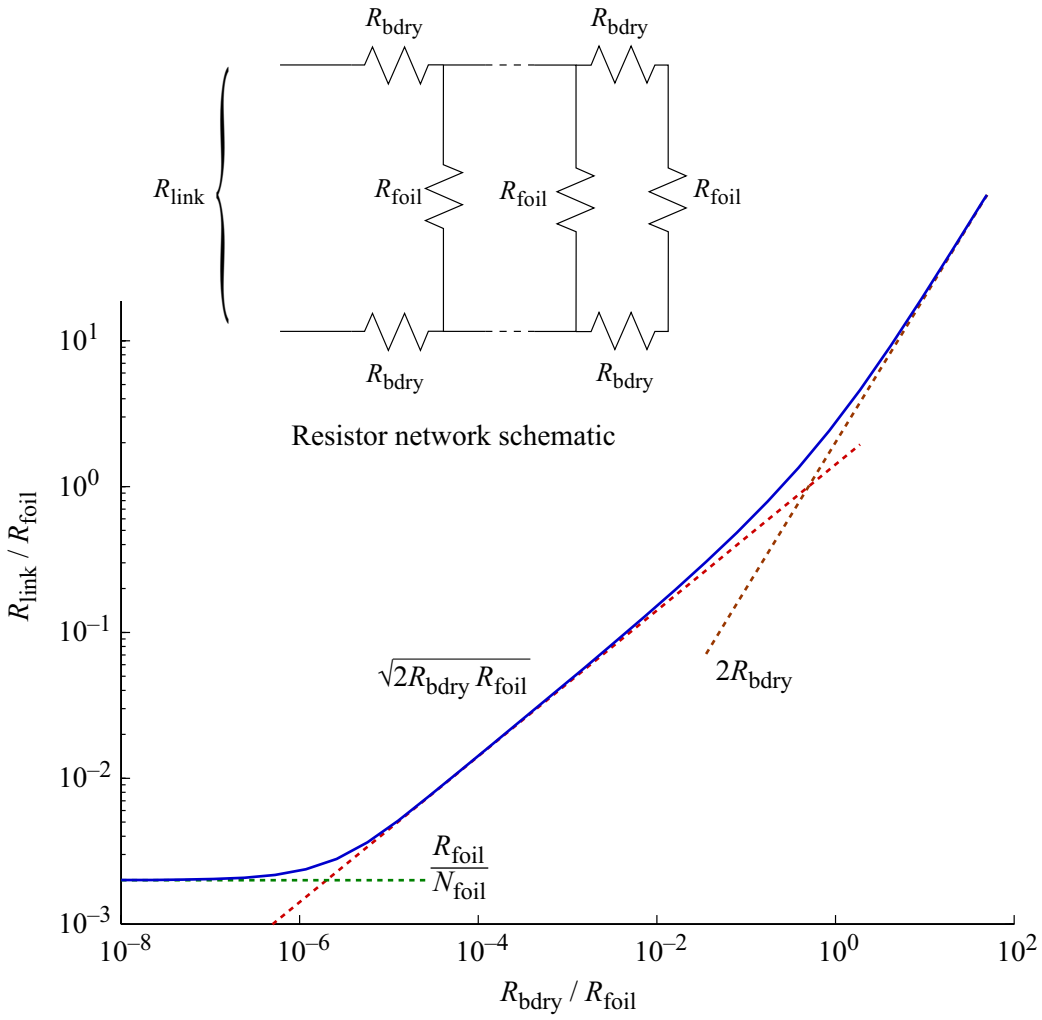

Figure 3.15: Thermal resistance of our foil heat link, modeled as a resistor network. We assume that each foil has the same thermal resistance along its length, and each boundary resistance is identical. The calculation was performed for 500 foils.

bolted to the cell while the upper clamp was bolted to the mixing chamber. The stacks were bolted to the clamps using 4 8-32 brass screws for each clamp. This allowed us to apply 400 lb. of compressing force to each end of the foil stack [85]. We expected the net thermal conductance of this heat link to be $80 \times (T/\mathrm{K})$ mW/K.[6] We assembled the cell with this heat link, and cooled the experiment. By applying heat to the cell, we were able to measure the actual thermal conductivity of the heat link. But instead of the large thermal conductance we expected, we measured the thermal conductance of the heat link to be $0.73 \times (T/\mathrm{K})^2$ mW/K. This large discrepancy is due to the addition of the many small boundary resistances between each foil. The T^2 dependence of the measured thermal conductance suggests that the conductance of this link is limited by an amorphous substance (such as oil or grease) (cf. [52]). We can model the foil heat link as a resistor network, as shown in Fig. 3.15. Between each foil end is a boundary resistance R_{bdry}, caused perhaps by an oxide layer or grease film. Each foil has a resistance down its length of R_{foil}. Using standard addition rules for resistances, we obtain a recursive relation for the resistance of a heat link with N foils:

$$R_{N+1} = 2R_{\mathrm{bdry}} + \frac{1}{1/R_{\mathrm{foil}} + 1/R_N}. \tag{3.5}$$

We can solve this equation numerically; the result for a 500 foil heat link is shown in Fig. 3.15. At large boundary resistances, the heat is conducted entirely through the first foil. For boundary resistances smaller than $R_{\mathrm{foil}}/N_{\mathrm{foil}}^2$, the conductance of the total mass of copper is obtained. Comparing this result to our measured heat link, we find that our thermal boundary resistance was $\approx 1/100$ the resistance of each foil. Despite this small boundary

[6]The conductance $K(T)$ is defined here such that the power transmitted between two ends of a heat link at temperatures T_1 and T_2 is $P_{\mathrm{link}} = \int K(T)dT$. This definition is only valid if temperature is constant across cross-sections of the heat link.

resistance, the net effect over 500 boundaries was to greatly reduce the thermal conductance of the heat link.

Although we could have done better at reducing the foil thermal boundary resistances in our heat link, the poor operation of our foil heat link caused us to go to a heat link composed of wires. This heat link was produced by Janis Research [86], using 4 bundles, each containing 600 5 mil diameter wires. Using data from a test conducted by Janis [86, private communication], we determined that these wires have a RRR of 65. Assuming the boundary resistances between wires, the heat link clamps, and the cell / mixing chamber are all negligible, this gives a predicted thermal conductance of $34 \times (T/K)$ mW/K. In this heat link the boundary resistances between copper wires are eliminated by welding the wire ends together. These wire ends are then welded at each end to a short copper tube. The copper tubes are then brazed to clamps that can be bolted to the cell or mixing chamber. The measured thermal conductance of this heat link, as affixed in our experiment (see Fig. 3.13), is $2.8 \times (T/K)$ mW/K. While not quite as high a conductance as we might desire, this gave us a cold enough cell that we could attempt buffer gas removal of trapped Li. A "thermal schematic" of the cell, showing the cell base temperatures and various conductance is shown in Fig. 3.16.

3.4.2 Preliminary measurements

We now had an apparatus with good thermal characteristics. Before we proceeded to buffer gas removal, we wanted to take some preliminary measurements of Li in our trap, in the diffusive regime. We measured both the yield of thermalized Li and the lifetime of trapped Li vs. buffer gas density, ablation energy, and the strength of the heater pulse we use to drive buffer gas into the gas phase.

After reducing our probe power (to prevent optical pumping), and substituting

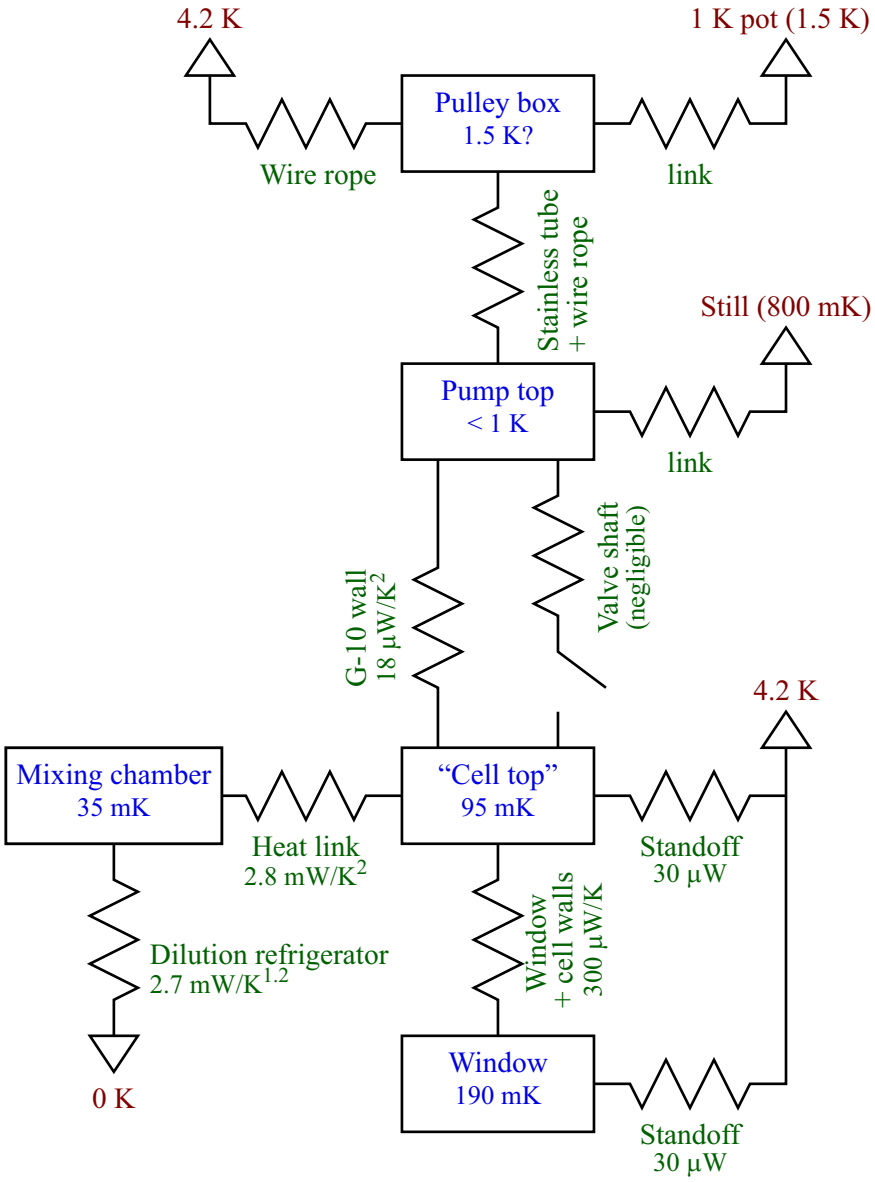

Figure 3.16: Measured thermal loads and conductances of the buffer gas pump-out experiment. All measurements were taken with a fridge still power of 3 mW. Boxes depict thermal masses of the cell. The associated temperatures are the base operating temperatures. The zigzag connections between the thermal masses are heat links. The associated annotation give the power for a given thermal difference across the heat link. These are written in the form a mW/K^b; this indicates the power conducted across the link is $P = a(T_1^b - T_2^b)$ mW.

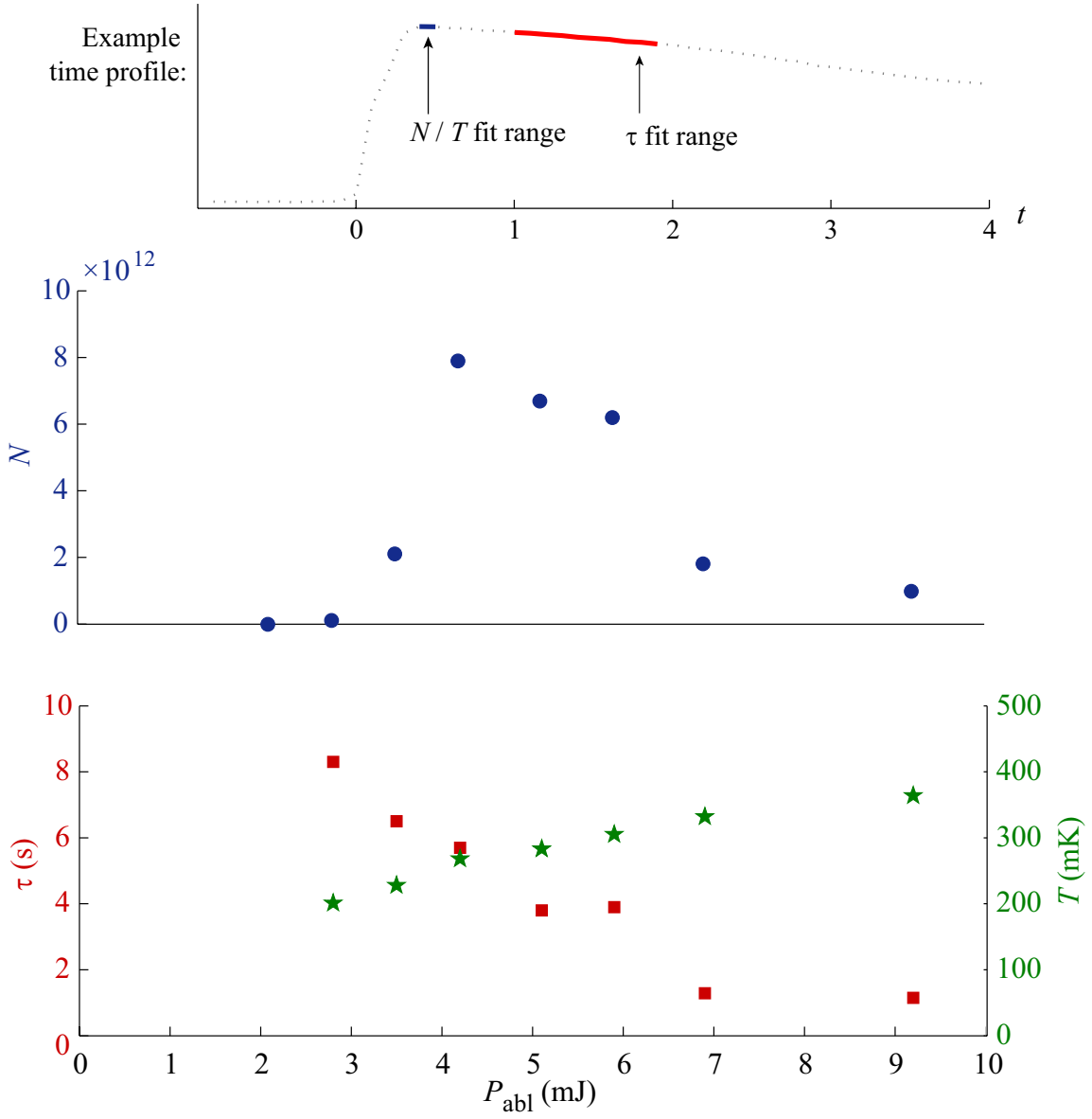

Figure 3.17: Li yield, temperature, and lifetime at early times vs. ablation power. The inset shows an example trace of integrated OD vs. time. We use the data between 0.4 and 0.6 s after ablation to extract number (circles) and temperature (stars). Lifetimes (squares) are fit beteen 1 and 3 s, after the OD decay begins to appear exponential. All these data are taken with no heater voltage applied to the cell; these are "cold loads". The cell contained $\approx 2 \times 10^{19}$ ^{3}He atoms when these data were taken.

PMTs for our photodiodes, we measured the number and lifetime of thermalized Li versus ablation energy. These results are shown in Fig 3.17. We find that there is a "sweet spot" of ablation energy. If ablation energy is too low, no atoms are ablated. If the ablation energy is too high, the atoms and cell are heated by the ablation pulse, leading to short trap lifetimes. For Li in our cell, we find that a 4 mJ pulse is best for producing large numbers of Li at long times.

We also investigated how these atom cloud parameters depended on the amount of energy applied to our cell heater located at the "cell top". The energy was applied by sending a fixed voltage for 0.5 s. This heat was applied 0.5 to 1.0 s prior to ablation. The results of this study, using a 4 mJ ablation pulse, are shown in Fig. 3.18. We found that for low heater energies, less than 6 mJ (corresponding to a heater voltage of 3 V), the heater has little affect on the initial production, temperature, or lifetime of the atoms. Presumably this is because the thermal dynamics of the experiment are dominated by heating from the ablation pulse. Only a fraction of the heater pulse is deposited in the cell walls, with much of the heat going directly to the mixing chamber; this contrasts to ablation, in which almost all of the pulse energy is delivered to the cell interior. As more than 6 mJ is applied, more and more buffer gas is driven into the gas phase, leading to longer lifetimes. At very high heater energies, the atoms are heated, leading to decreased lifetimes as η decreases.

3.4.3 Buffer gas pumpout

When we first began the experiment, we would open our valve as quickly as possible (an opening time of $\approx$ 30 ms). We hoped to load atoms at hot temperatures, 400 mK or greater; pumping on the buffer gas at these hot temperatures would ensure a thin buffer gas film when the cell reached its base temperature of 100 mK. In order to achieve a pumping time below the atom loss forbidden region (See Fig. 2.6), this would require as short a valve

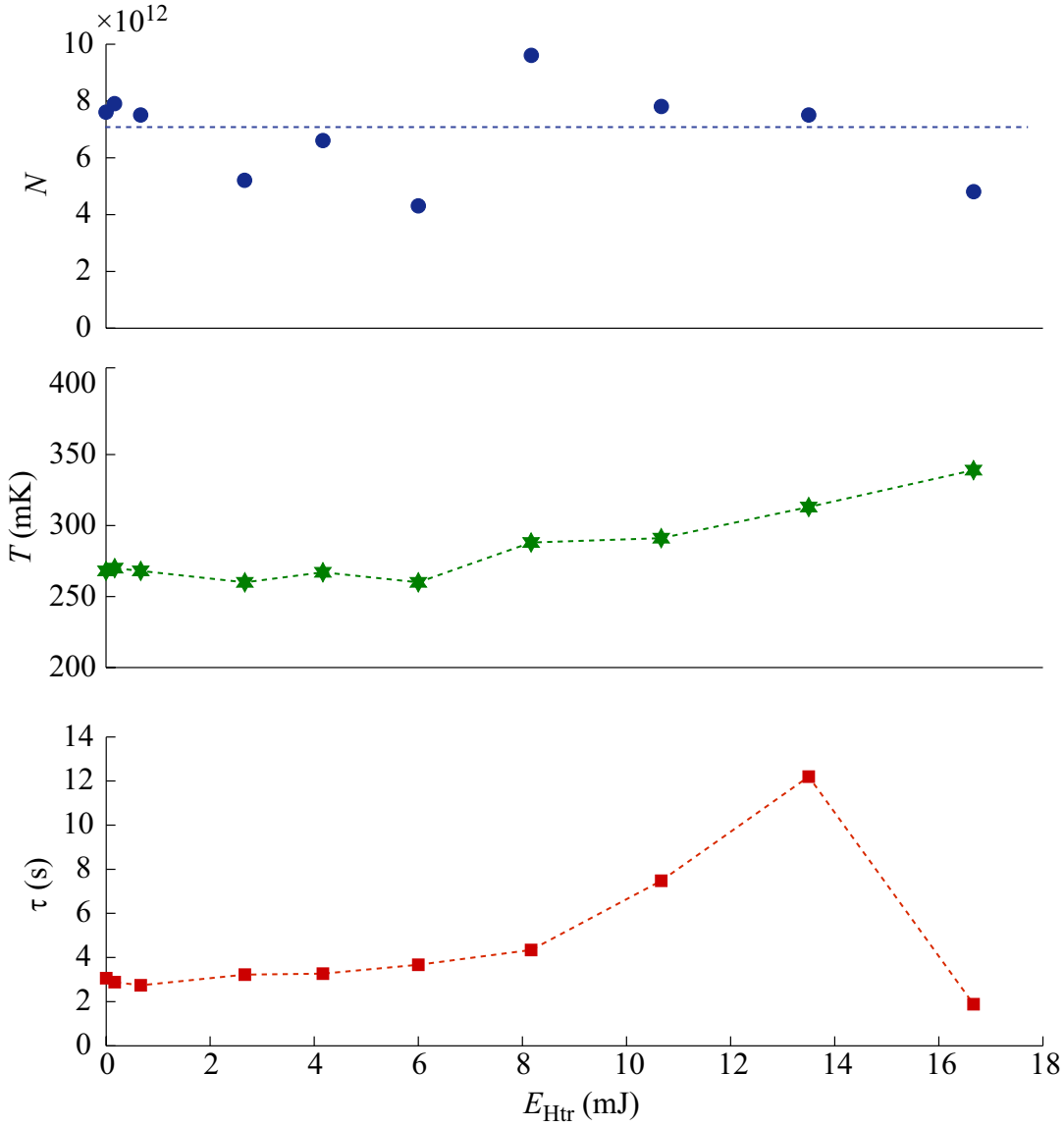

Figure 3.18: Li yield, temperature, and lifetime at early times vs. applied heater pulse. Atoms were ablated using a 4 mJ pulse. The cell contained $\approx 2 \times 10^{19}$ ^{3}He atoms.

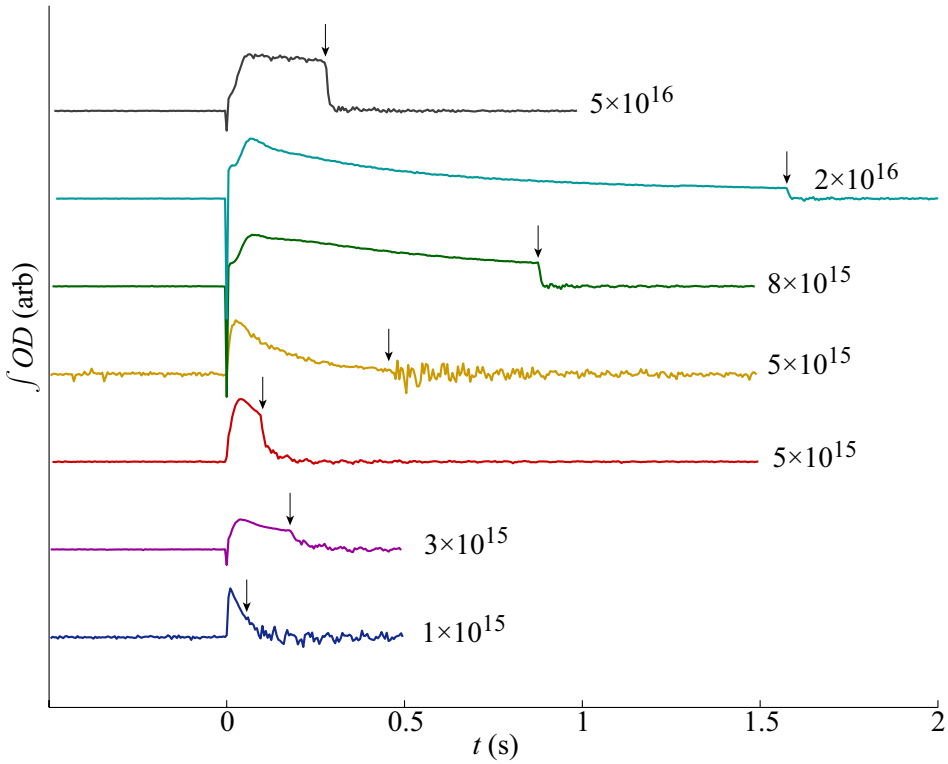

Figure 3.19: Atom optical density profiles for fast (40 ms) valve opening times. Arrows indicate when the valve was opened. Profile annotations indicate approximate buffer gas density, in cc^{-1}. Atom temperatures were between 450 and 550 mK.

opening time as possible. Results for 450 – 550 mK atoms are shown in Fig. 3.19. We find, for buffer gas densities $> 3 \times 10^{15}$ cc^{-1}, that wind removes all our atoms, due to the fast valve opening time. For smaller buffer gas loading densities, we simply lose all our atoms before we traverse the valley of death.

Because we could not successfully remove buffer gas with such fast valve opening times, we implemented the pneumatic actuator throttling described in §3.4.1. We throttled the valve such that the time to open the valve was around 300 ms. In addition, we allow the atoms to cool to between 200 to 350 mK, to prevent valley of death loss. An example integrated optical density profile for this pump-out method is shown in Fig. 3.20, for atoms at a loading temperature of 240 mK. After opening the valve, we see atom loss while we traverse the valley of death. This loss disappears after a few seconds, and we have trapped atoms for long lifetimes, up to 150 s. At early times, the atom temperature given by spectral fits tracks the cell temperature given by our resistive thermometer located at the cell top. These temperatures are discrepant by 20 mK, suggesting a systematic error from either the thermometer calibration or the laser voltage-to-frequency conversion. At late times we see that the atom temperature ceases to track the cell temperature. This is suggestive of thermal isolation — that atom-atom loss is dominating the heating and cooling of the atom cloud.

The long-term behavior of the trapped Li sample after buffer gas pumpout is shown in Fig. 3.21, vs. applied heater energy. We observe that the trapped Li is more or less unaffected by heater energy as long as this energy is less than a critical value, above which all Li is lost after valve opening. This loss is due either to wind loss (because more buffer gas is in the gas state in the hot cell) or valley-of-death loss (because the atoms are hotter at valve opening).

We also found that we could observe long lived atoms without opening the valve.

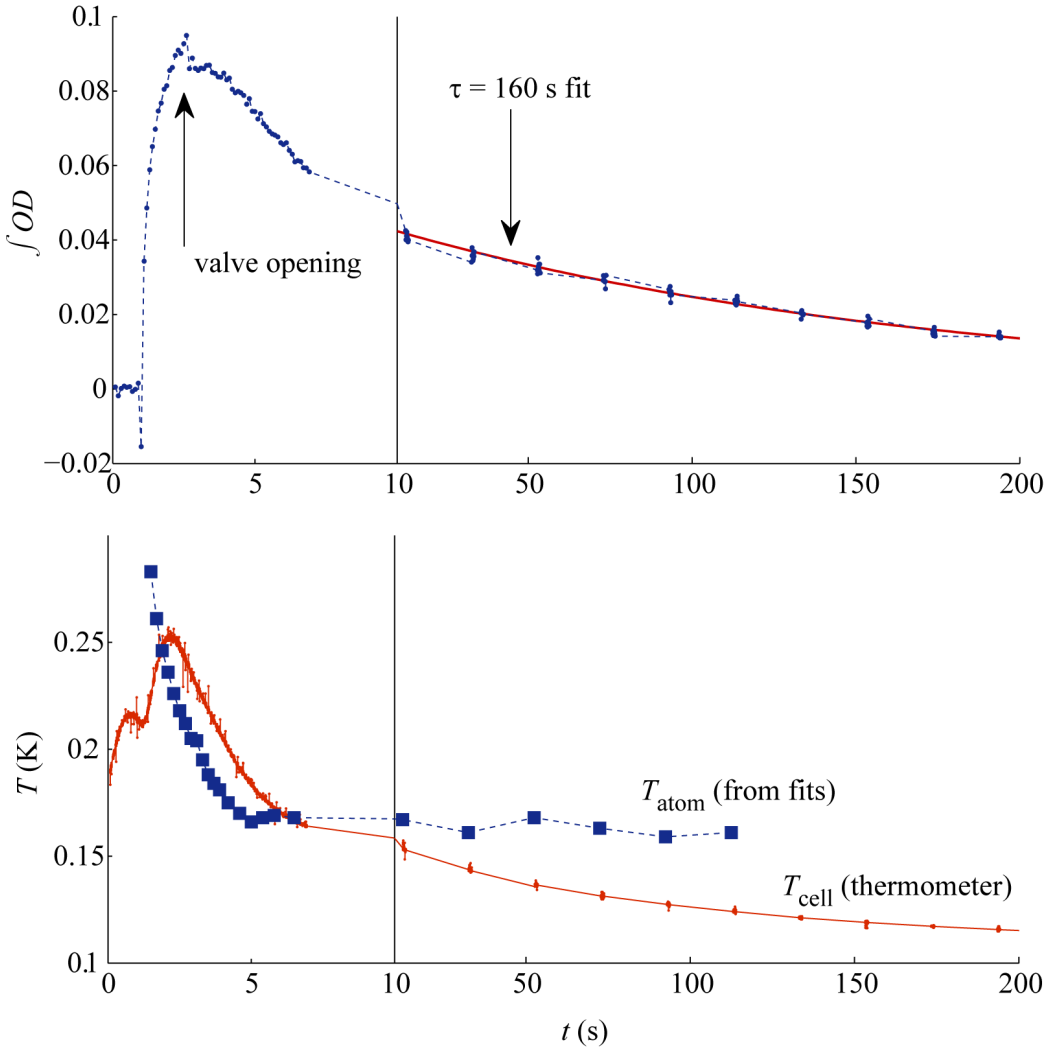

Figure 3.20: The upper plot shows an atom optical density profile for a slow (300 ms) valve opening time. The valve begins opening at 1.5 s after ablation. The heater energy was 8 mJ. The lower plot shows the corresponding atom and cell temperatures. Note the change of scale on the t axis.

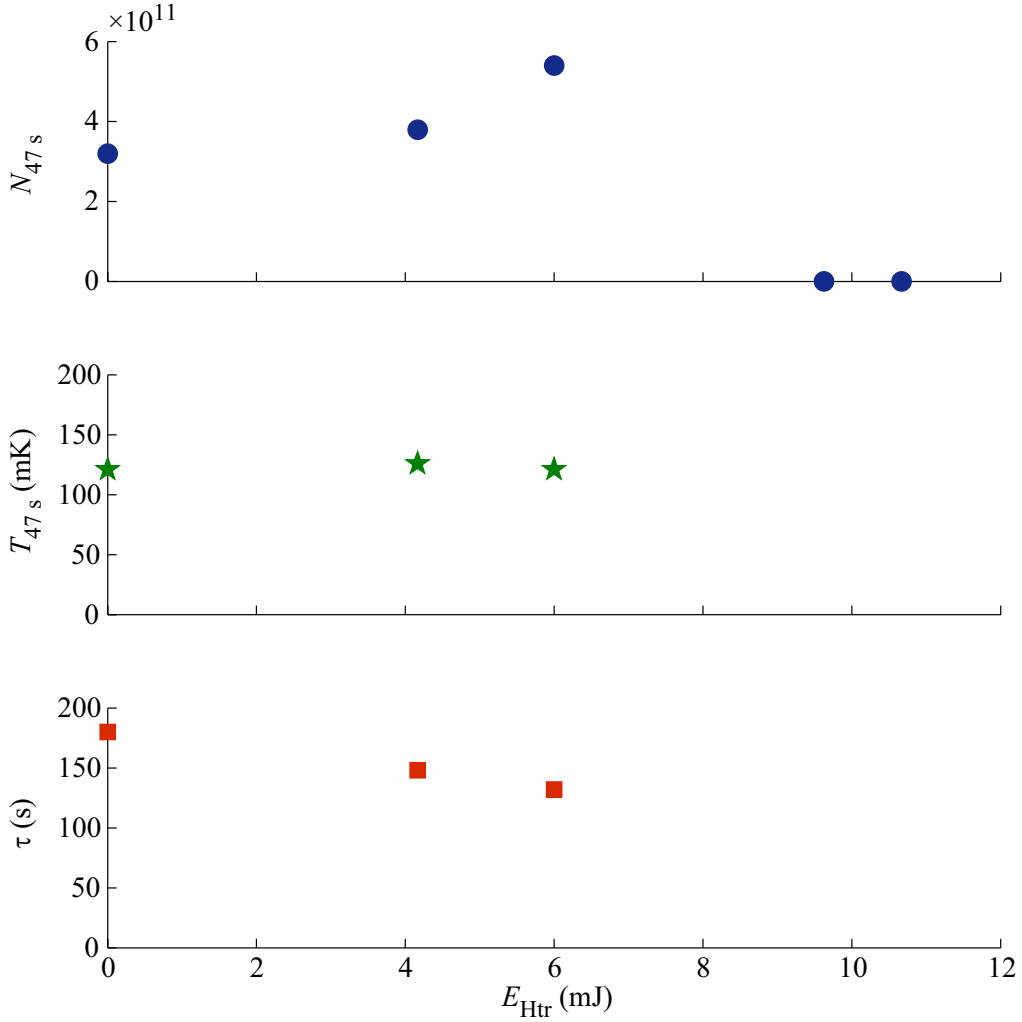

Figure 3.21: Number (circles) and temperature (stars) of Li at 47 s after ablation. Buffer gas is removed with the valve, opened in 300 ms. Also shown is the long-time lifetime (squares) after valve opening. Ablation energy was 5 mJ.

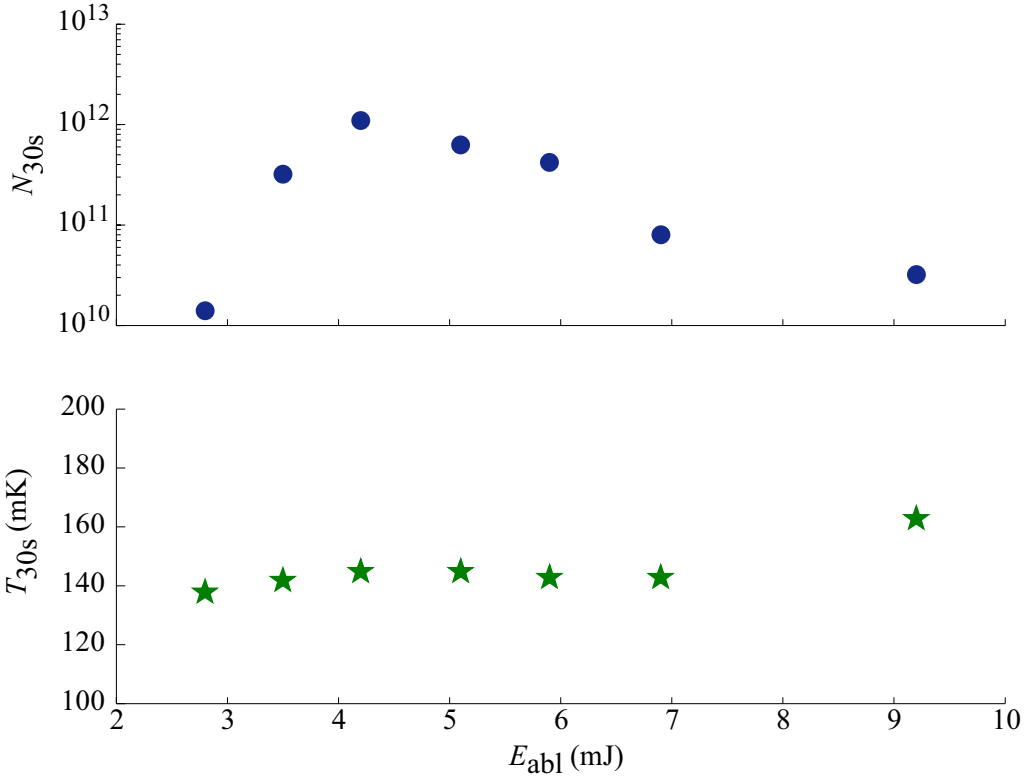

Figure 3.22: Long-time behavior of Li after buffer gas removal by freeze-out. No valve or heater pulse was used. The cell contained $\approx 2 \times 10^{19}$ ^{3}He atoms.

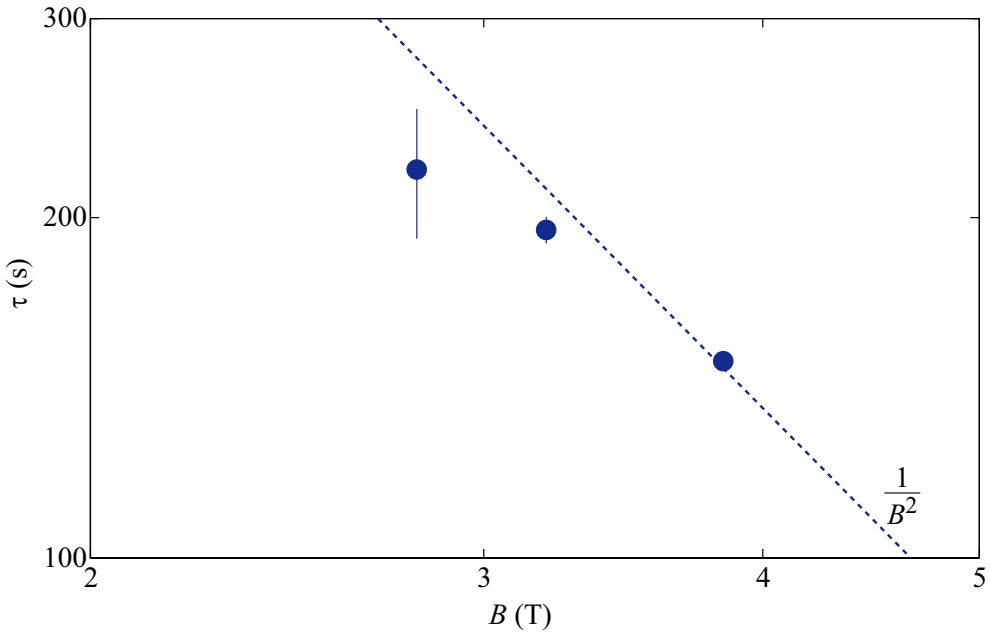

Figure 3.23: Long-time lifetime of trapped lithium, vs. loading trap depth, after buffer gas pumpout. The dashed line shows the expected field dependence of Majorana loss. Atom temperature is 150 mK.

Without opening the valve, the buffer gas freezes to the cell walls as the cell cools to its base temperatures. As long as the atoms are cold enough when loaded, the valley of death lifetime will be long enough that the atoms survive the freeze out. With no heater pulse applied to the cell, and using a 4 mJ ablation pulse, we retained 60% of our atoms at long times (specifically, at 30 s after ablation). Fig. 3.22 shows a plot of the number of atoms remaining 30 s after a freeze-out of the buffer gas vs. ablation power. Also shown is the temperature of the atoms at 30 s. For all but the most extreme ablation energy, the atoms all end up at the same low temperature.

We wished to determine to determine what process was limiting our atom lifetime. If we were to observe 2-body loss, due to atom-atom evaporation, we could be confident we had achieved thermal isolation. However, the observed decay after buffer gas removal, either using the valve or cell wall cooling, was always 1-body. To see if this loss was due

to background gas evaporation or due to Majorana loss (cf. [57], Table 2.2), we varied the loading trap field (the field is still held constant during each time profile observation). A plot of the observed lifetime vs B_{trap} is shown in Fig. 3.23. The dashed line shows a $1/B^2$ power law; this is the behavior of Majorana loss. Because we see that the lifetime decreases with increasing field, we conclude that the atom lifetime is dominated by Majorana loss.

Before moving on to our next experiment, we wished to see if we could show thermal isolation in our copper cell. Because the atom lifetime was Majorana limited, we could not distinguish between background gas evaporation and atom-atom evaporation in our trapped sample. Because we could not ramp the magnetic field after the buffer gas pump-out, we could not lower η after loading, in order to make evaporation the dominant loss mechanism. However, we could lower η using optical pumping. In this scheme we applied a large amount of laser power (> 10 μW) at a frequency resonant with atoms at a magnetic field corresponding to $\eta = 5$. This should remove all the atoms with orbits passing through this magnetic field. Because we had only one laser available, this was done by halting the laser scan. Restarting the laser scan took 100 ms, setting a minimum delay time before the resultant atomic spectrum could be observed. If the atoms were thermally isolated, and if the atom-atom rethermalization time were longer than this delay time, we would see a distorted spectrum that thermalized over time to a colder temperature than before the optical pumping. We never saw a distorted spectrum, nor did we see cooling of the atomic cloud after the optical evaporation, even for optical evaporation resulting in large atom loss. This implies that the atom-background gas rethermalization time is shorter than 100 ms.

3.5 Thermal isolation experiment

Because our lifetime in the buffer gas pump-out experiment was not limited by atom-atom evaporation, we needed to move to lower η to verify thermal isolation. We would load our trap at $\eta = 15$, pump out the buffer gas, then ramp to a low η where atom-atom evaporation dominated over Majorana loss. If atom-atom evaporation loss were dominant, we would see 2-body loss and cooling of the atoms. If we were not thermally isolated, we would expect to see a rapid 1-body loss due to background gas driven evaporation (see the $\eta = 5$ curve on Fig. 2.6) and no cooling of the atoms.

This experiment is discussed in detail in Newman's thesis [71]; a brief description is given here. The apparatus is depicted in Fig. 3.24. We wanted to ramp our magnet while our atoms were contained in the trap. This requires that we minimize induced eddy currents in the cell. To do this, we added a bucking coil. This coil cancels the magnetic field between the cell top and the mixing chamber to below 300 gauss at full current. We replaced all the metallic parts of our valve below the cell top with Vespel. Instead of a copper cell, our cell was of a composite G-10 / copper wire construction. The cell vacuum was made by a thin G-10 wall. Over this wall we laid 1000 10 mil diameter copper wires. These provide the thermal connection between the top and bottom of the cell. The wires are gathered at the cell top into a bundle (not shown on the figure); this bundle extends to the level of the mixing chamber, where the wires are welded to a clamp; this clamp is then bolted to the mixing chamber. In this experiment the base temperature at the cell bottom was 165 mK. For a complete description of the apparatus, see [60].

To evaporate the atom cloud, one of the top or bottom coil currents would be reduced. This moves the center of the trap up (to the mirror) or down (to the window). This brings the atoms closer to an evaporation surface, reducing η. This method is used (as

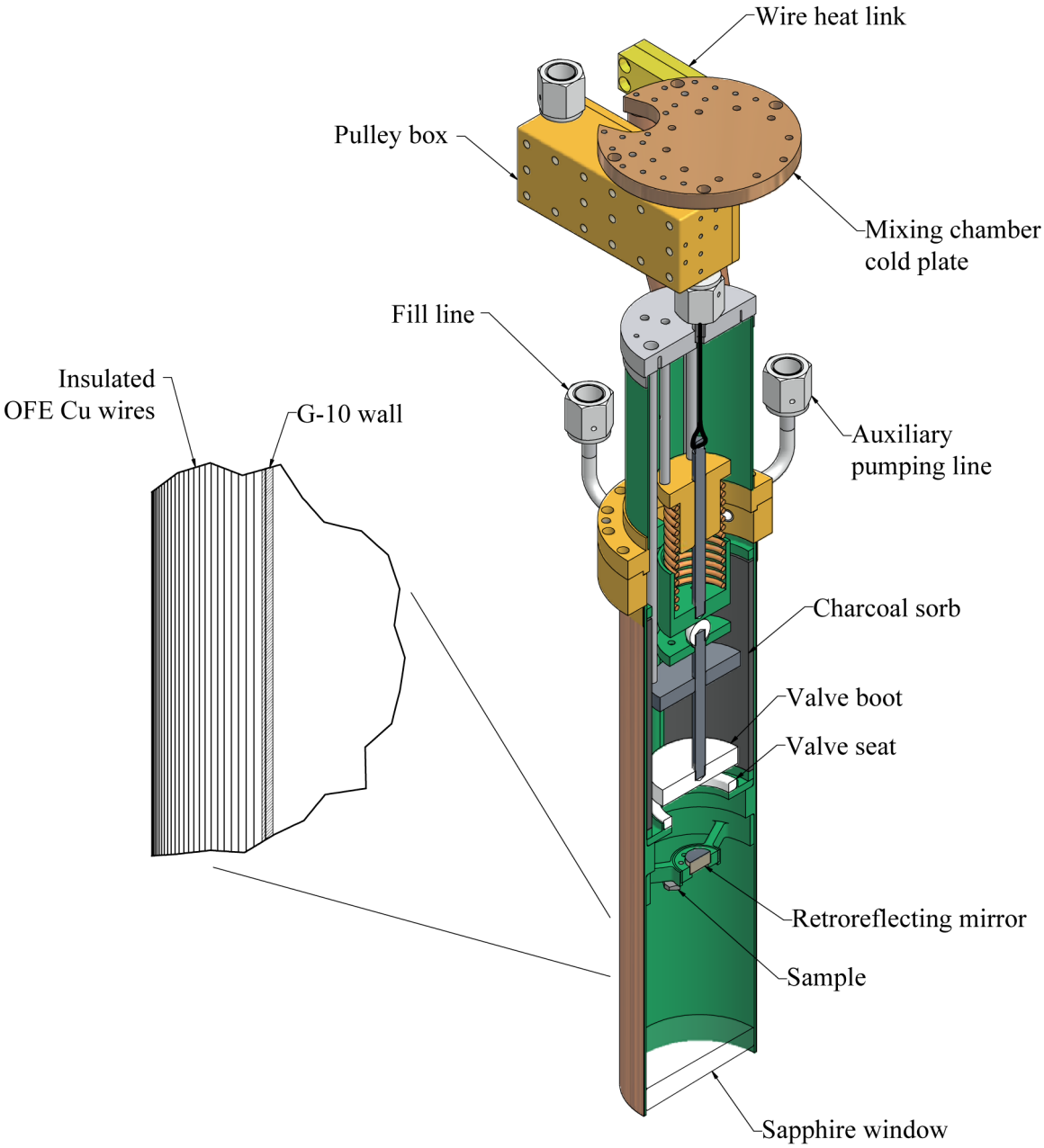

Figure 3.24: Apparatus used for the evaporative cooling experiment. The wires running the length of the cell are gathered into a bundle at the cell top. This bundle (not shown) extends to the level of the mixing chamber, where the wires are welded to a copper clamp which is bolted to the mixing chamber cold plate.

opposed to equal reduction of the coil currents) to ensure tight confinement of the atoms and therefore a rapid elastic collision rate (cf. [87, §6.6]). As the magnet is ramped, eddy current heating increases the temperature of the cell. For a 5 A/s ramp of the coil currents, the cell temperature would increase to 185 mK for ramps to the mirror or 190 mK for ramps to the window.

When we evaporated the atoms, we observed fast loss of the atoms (less than a 1 s time constant) when η was reduced below 4.5. If η was reduced to 7, atoms remained long enough that we could observe the atom temperature. The Li temperature was seen to be around 80 mK. We can calculate the density of background gas necessary to pin the Li temperature at 80 mK by balancing the background gas heating rate (2.43) at this trap depth with the atom-atom cooling rate (2.47). This gives a background gas density of between 10^{11} and 10^{12} cc^{-1}. The observed fast atom loss at low η is consistent with background gas-driven evaporation loss.

We can not tell whether this high background gas density is caused by cell heating from the magnet ramp. We did reduce the cell heating by ramping more slowly; however this came at the expense of lower signals and we did not observe any improvement in atom temperature. It is also possible that we never achieved thermal isolation in the first place, or that because of the weaker thermal conduction along the sides of the plastic cell, that we do not have thermal isolation in this apparatus.

3.6 Conclusions

We constructed an experiment to trap 1 μ_B species using buffer gas cooling. Large numbers of Li atoms were trapped, up to 10 trillion atoms, at initial temperatures between 250 mK and 500 mK. This was achieved by carefully adjusting the energy of the ablation

laser, with the most favorable results obtained at $E_{\mathrm{abl}} = 4$ to 6 mJ. We found that applying heat to the cell prior to ablation was more or less unnecessary, and in fact detrimental to trapping for high enough heater powers.

We were able to remove buffer gas past the valley of death, with up to a trillion atoms remaining after buffer gas removal. Buffer gas was removed to a high enough degree that the Li lifetime appeared to be dominated by Majorana loss, with a 150 ± 10 s lifetime at $U_{\mathrm{trap}} = 2.7$ K. We were able to remove buffer gas using our cryogenic valve, as long as the valve opening was slow enough to prevent wind loss. We also were able to remove the buffer gas using a freeze-out, by allowing the cell to cool rapidly to below 140 mK. For both of these techniques, we found it is generally better to perform a "cold load" of the atoms: that is, buffer gas is not driven into the gas phase prior to ablation.

When we attempted to show thermal isolation of our trapped Li, we found conflicting evidence. On the one hand, a comparison of atom temperatures taken from atomic spectra with cell thermometer temperatures suggested that the two temperatures were independent. Optical pumping experiments suggested that the atom temperature was pinned by the background gas. When we attempted to evaporatively cool the Li atoms, we could not cool them below 80 mK.

Based on our experience with trapping Li, we give a "recipe" for buffer gas trapping of 1 μ_B species. This recipe is shown in Table 3.1. The secret to obtaining dense samples of buffer gas cooled species after buffer gas removal is to have atoms at a certain minimum η. Our experiments show that this minimum η is 10. This is similar to the value[7] obtained by a previous buffer gas experiments in a warmer apparatus[58], limiting that experiment to species with magnetic moments greater than 2 μ_B. In order to buffer gas-trap trap 1 μ_B

[7]Michniak and his collaborators found that, in a nearly identical magnetic field, the minimum magnetic moment for buffer gas removal was 2 μ_B, for an atom temperature of 600 mK during buffer gas removal. This corresponds to $\eta \approx 10$.

1 μ_B buffer gas trapping "recipe"

1. Cool the trapping cell to < 150 mK.
2. Introduce hot atoms. The cell temperature should be between 250 mK and 280 mK.
3. Remove the buffer gas with $\eta \geq 10$, slowly enough to avoid wind, using either:
   A. Valve pumpout. The valve should be large enough to pump out significantly faster than the $\eta = 10$ valley of death lifetime. The rate at which the valve is opened should be adjusted to avoid wind.
   B. Freeze-out. A minimal amount of heat is applied to the cell during the introduction of hot atoms. The buffer gas is pumped by the cooling cell.
4. Reduce the residual buffer gas to thermal isolation density. This has not yet been demonstrated with 1 μ_B species. The most attractive options are:
   A. Bakeout the cell while atoms are present in the trap, with the valve open. In order not to lose atoms, η must be kept well above $\eta = 10$. cf. [58].
   B. Cool the cell such that the vapor density of He is lower than the thermal isolation density. Care must be taken to eliminate "hot spots".

Table 3.1: 1 μ_B buffer gas trapping recipe.

species and then remove this buffer gas, we therefore require loading temperatures between 250 mK (to obtain sufficient buffer gas density) and ∼280 mK (to maintain high η). The upper bound is set by the trapping field — if a deeper magnetic trap is used, this number should increase.

The required experimental conditions to obtain thermal isolation are more elusive. Certainly if the entire interior of the cell can be made colder than 100 mK, the background gas density will be lower than 10^{10} cc^{-1} (cf. Fig. 2.5). In our thermal isolation experiment, we could only obtain cell wall temperatures of 170 mK or so. Michniak showed [58] that the remnant background gas can be reduced by performing a "cryo-bakeout": pumping on the gas with the cell at the hottest temperature the trapped atoms can bear, and then lowering the cell wall temperature. This method requires a large temperature swing, however. In his experiment the buffer gas was pumped at temperatures 100 mK to 200 mK hotter than the base temperature. The behavior of atoms in our experiment after various bakeouts is

described in Newman's thesis [71]; we were never able to successfully use this method to achieve thermal isolation.

Making improvements to the apparatus to lower the base temperature of the cell are therefore the best chance for achieving thermal isolation of 1 μ_B species. In addition, using a more massive species such as potassium (K), would allow more aggressive cryo-bakeouts, due to the reduced efficiency of energy transfer with the He background gas.

Chapter 4

Noble metal experiments

In applying buffer gas cooling to the noble metals, we wished to show that buffer gas cooling could open up new 1 μ_B systems for study. Like the alkali atoms, the noble metals are composed of closed core electron shells and a single valence s electron, giving a ground state dipole moment of 1 μ_B. At the same time, the noble metals copper (Cu), silver (Ag), and gold (Au) possess narrow two-photon transitions. Ag has garnered particular interest: it has two-photon transition with a linewidth of 0.8 Hz, which is interogated at 661 nm. This line has attracted attention as a proposed frequency standard [88], with groups working on producing cold Ag samples [45] and measuring the clock transition [43]. Meanwhile, Au is the heaviest stable atom with a single s valence electron. Its atomic spectrum is greatly influenced by relativistic effects, and is hence a good species for testing relativistic theories of atomic structure [44]. Furthermore, new classes of atoms can exhibit novel collisional behavior at cold temperatures, leading to increased theoretical understanding of interatomic interactions [28, 64, 89, 90]. The large laser powers at UV frequencies needed to laser cool the noble metals (240 to 330 nm) have posed a serious challenge to experiments thus far, limiting the number of Ag atoms trapped in a MOT to 3×10^6 [45].

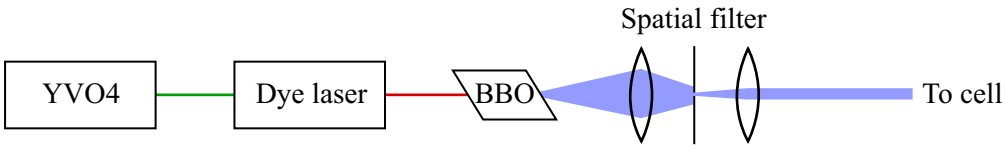

Figure 4.1: 330 nm light generation for Cu and Ag spectroscopy.

Figure 4.2: 243 nm light generation for Au spectroscopy.

4.1 Method

4.1.1 Apparatus

The cryogenic apparatus used was the same apparatus as used for our Li thermal isolation experiment, and described in §3.5. For most of our measurements we simply left the valve closed, and measured the properties of our buffer gas cooled samples at constant buffer gas density. In general, due to the high ablation powers needed to produce the noble metals, the samples were too hot to allow for buffer gas removal.

Light for the spectroscopy transitions at 325 and 327 nm for Cu, 328 and 338 nm for Ag, and 243 nm for Au, was produced by frequency doubling light from a dye laser. For the $\sim$ 330 nm transitions, light was produced using a YVO4-pumped Coherent 899 ring laser [78] using DCM Special dye, then frequency doubled with a single pass through a BBO crystal. The light was then spatially filtered into a 2 mm diameter Airy beam, and sent to the cryostat bottom. Light for the Au transition was produced using an ion laser-pumped Coherent 699 ring laser using Coumarin 480 dye, then frequency doubled using a Coherent MBD-200 resonant frequency doubler. For the 243 nm Au light, the divergence of the beam

after the doubler was compensated by passing the beam through an iris once it reached the bottom of the cryostat.[1] In each case the UV light was delivered via free space coupling, as opposed to the fiber delivery used for Li.

4.1.2 Collisional studies

We wished to study noble metal-^{3}He inelastic Zeeman relaxation collisions. These studies were done in the short λ regime, where we would be sensitive to Zeeman relaxing collisions. In this regime, the total lifetime of atoms in the trap is the reciprocal sum of the diffusion (2.34) and Zeeman relaxation lifetimes (2.40):

$$\tau_{\rm trap}(n_b) = \frac{1}{1/\tau_D(n_b,\eta) + 1/\tau_R(n_b)}. \tag{4.1}$$

Ideally we would have a very good knowledge of the background density n_b in the trap. Then the atom-^{3}He diffusion cross-section $\bar{\sigma}_D$ and the relaxation cross-section $\bar{\sigma}_R$ could be measured by fitting (4.1) to the trap lifetime. Knowledge of n_b would ideally be obtained by measuring the zero-field diffusion lifetime (2.28) of an atom whose diffusion cross section was well known. Such an atom, however, was not readily availabe to us. We can, however, extract the ratio γ_R of $\bar{\sigma}_D$ to $\bar{\sigma}_R$, without knowing n_b precisely.

To eliminate n_b, we use (2.28) and (2.34) to transform (4.1) into a relation between trap-on lifetime and trap-off lifetime τ_0. Doing so gives

$$\tau_{\rm trap}(\tau_0) = \frac{\tau_0}{e^{-0.31\eta - 0.018\eta^2} + (g_{\rm cyl}\,\bar{v}_\mu^2/\gamma_R)\,\tau_0^2}. \tag{4.2}$$

To measure γ_R, we load buffer gas into our cell to achieve a desired τ_0. We then turn on the magnetic trap to measure $\tau_{\rm trap}$. The experiment is repeated for a range of τ_0, and $\tau_{\rm trap}$

[1] Spatial filtering was necessary with the 330 nm light because we only obtained 100 μW from the single-pass doubling, compared with the 10 mW we obtained from the MBD-200. Spatial filtering of the 243 nm beam introduced extra noise into our system.

is fit to

$$\tau_{\text{trap}}(\tau_0) = \frac{\tau_0}{C_1 + C_2\,\tau_0^2}, \tag{4.3}$$

where C_1 and C_2 are the fit parameters. The cross-section ratio is determined from C_2, the geometry factor g_{cyl}, and the thermal velocity of the colliding system:

$$\gamma_R = \frac{g\bar{v}_\mu^2}{C_2}. \tag{4.4}$$

4.2 Measurements

4.2.1 Zero field

Atomic Cu, Ag, and Au were produced via laser ablation. The ablation energies necessary to achieve similar densities as were achieved with Li were significantly higher, however. This means that our atoms were very hot after ablation, with atom temperatures between 500 to 600 mK, at 500 ms after ablation. In the noble metals we also noticed that, for a given ablation energy, there was a threshold buffer gas density. For densities above this threshold, the zero-field diffusion lifetime is seen to be a constant for increasing buffer gas density. At which density this threshold occurs appears to be species dependent — for Cu and Ag this threshold occurs at $\lambda \approx 8$ μm for the 5 to 12 mJ ablation energies used in this experiment, while for Au the threshold was highly dependent on the ablation energy, and is shown in Fig. 4.4. This phenomenon has been observed before in buffer gas cooling experiments loaded with laser ablation [57, Chapt. 4], and while various mechanisms have been proposed to explain this behavior, including macroscopic ablation ejecta (a.k.a. "dust") and shock waves in the buffer gas, the exact nature of this "non-diffusion" loss process is unknown. When this process is active, the trap lifetime is seen to be limited to the same value as the zero-field lifetime — trapping is impossible in this regime. Thus we only were able to trap Cu and Ag in our experiments. Budker [91] has suggested that large

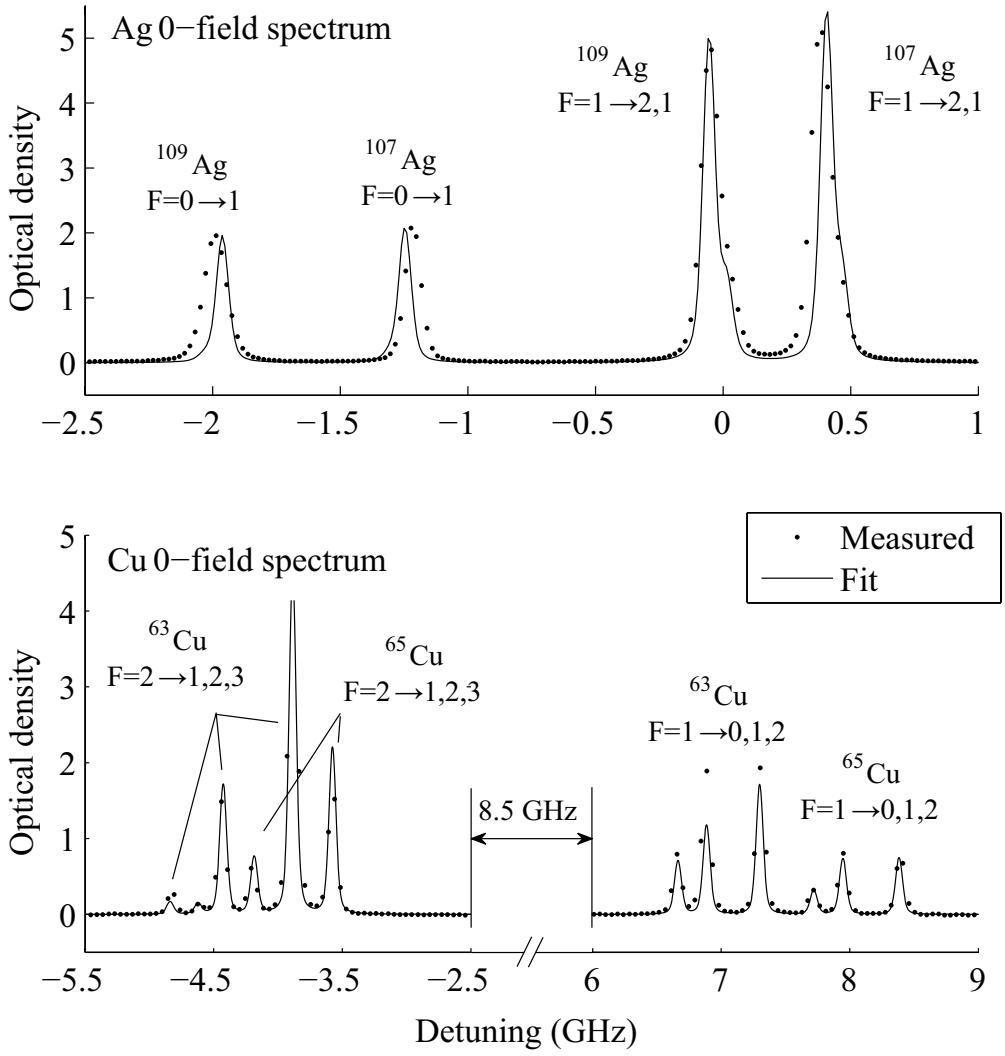

Figure 4.3: The zero field spectra of Cu and Ag in our experiment, with peak hyperfine and isotope assignments, and fit spectra.

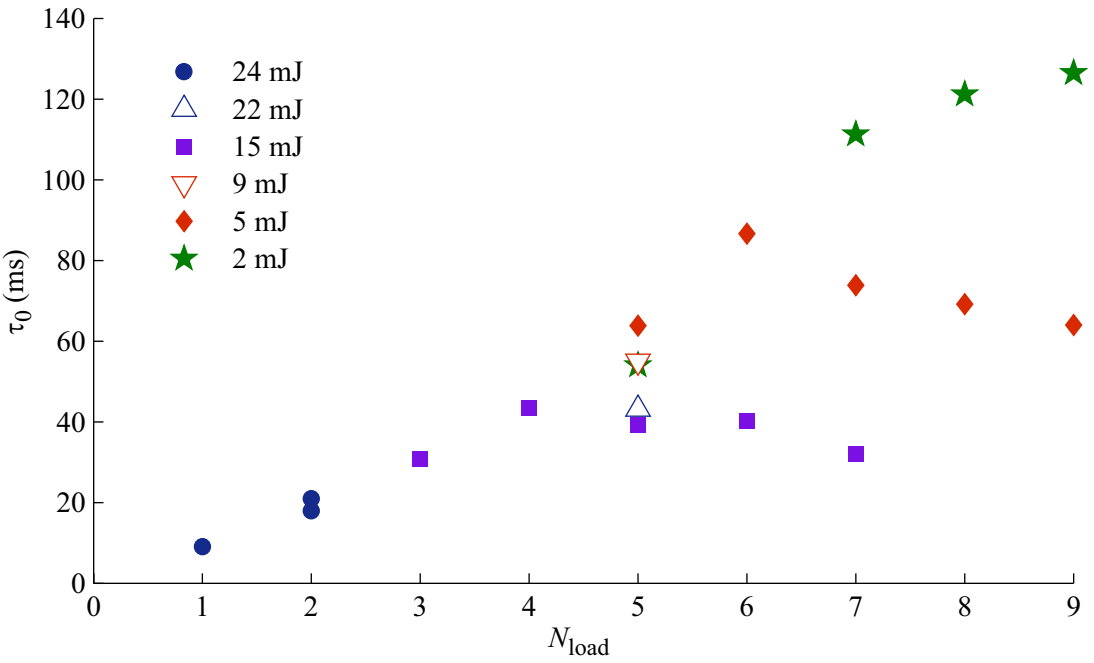

Figure 4.4: Lifetime of Au at zero field vs. ablation energy and the amount of buffer gas loaded into the cell. Each load adds $\approx 5 \times 10^{14}$ cc^{-1} to the cell buffer gas density.

numbers of Au can be thermalized in buffer gas cooling experiments with minimal ablation energies by ablating the tip of a fine (50 μm diameter) Au wire.

Fig. 4.3 shows the measured absorption spectra of Cu and Ag at zero field. We use known ground state hyperfine splittings [92–94] to calibrate our laser scan, and then fit the spectrum for all unknown spectroscopic constants. The accuracy of the results is limited by a $\sim 10\%$ nonlinearity in our laser scan. For Ag, we fit for the isotope shift of the line center of gravity, yielding $\nu_{109} - \nu_{107} = -520 \pm 50$ MHz, in agreement with Walther's -470 ± 10 MHz result. For Cu we measure $\nu_{65} - \nu_{63} = 540 \pm 50$ MHz. We also fit for the excited state hyperfine structure. The measured magnetic dipole and electric quadrupole hyperfine constants are shown in table 4.2.1.

Hyperfine constants of excited state Cu		
Isotope	$a_{3/2}$ (MHz)	$b_{3/2}$ (MHz)
63	190 ± 20	-30 ± 20
65	210 ± 20	-20 ± 20

Table 4.1: Measured hyperfine magnetic dipole a_j and electric quadrupole b_j coefficients of the $^2P_{3/2}$ state of copper. For definitions of these coefficients, see App. A.

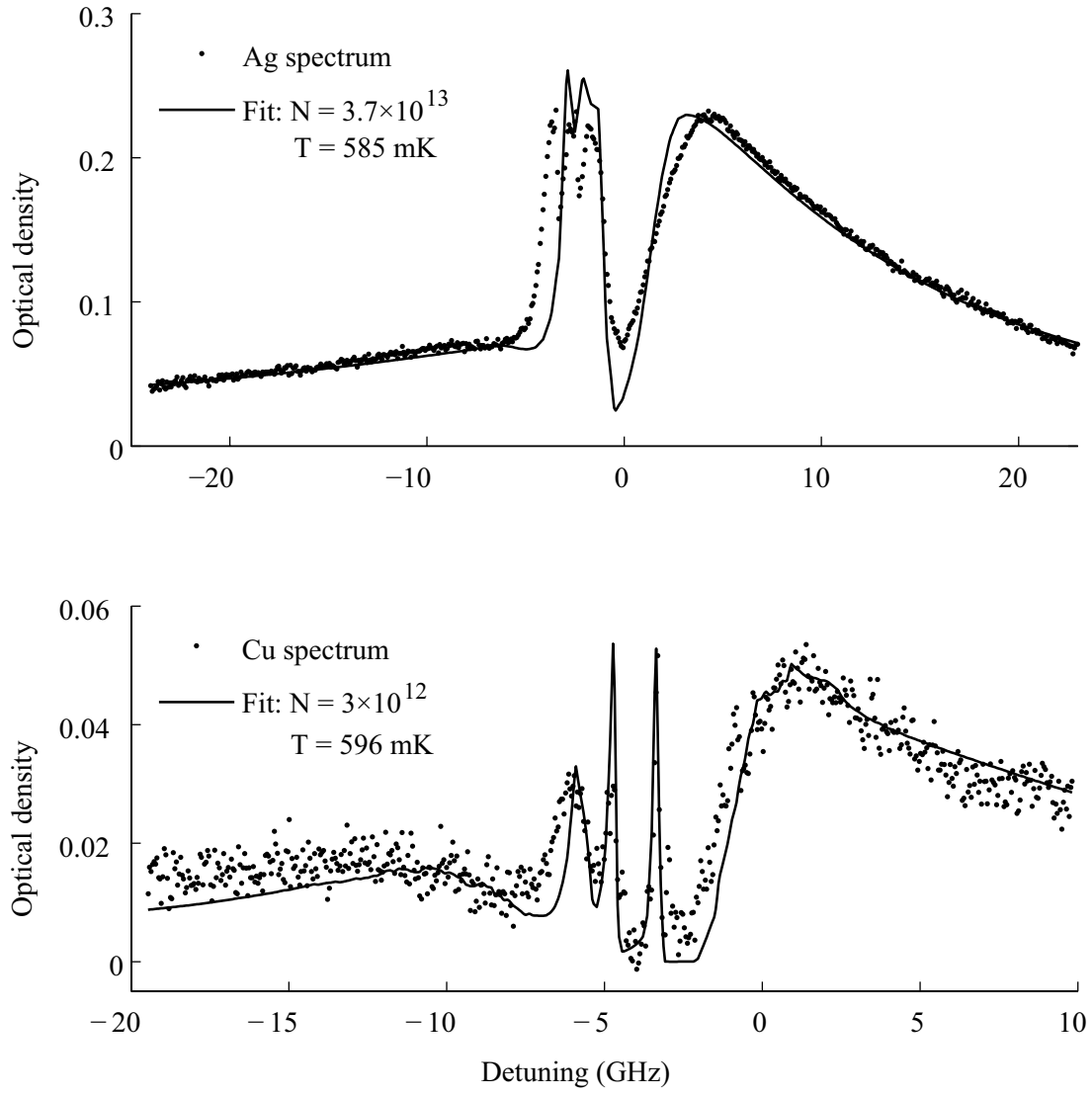

Figure 4.5: Measured spectra of Cu and Ag in our 4 T anti-Helmholtz trap, with best-fit simulations. The fit parameters are number, temperature, probe beam profile and hyperfine sublevel populations.

4.2.2 Trapping field

Typical spectra of trapped $\left|m_J = \frac{1}{2}\right\rangle$ Ag and Cu in our anti-Helmholtz trap are shown in Fig. 4.5. See App. A. The spectra are simulated from experimental parameters including atom number, temperature, field profile, and probe beam characteristics [57, 95]. By fitting the simulation to the measured data, we can extract properties of the trapped atom cloud. We trap 4×10^{13} Ag atoms and 3×10^{12} Cu atoms at 600 mK, at 500 ms after ablation.

Atom lifetime is determined by scanning the probe laser rapidly (between 5 and 100 Hz) relative to the atom loss rate. Lifetimes are taken from the decay of the integrated optical density. Low-frequency noise is reduced by subtracting the integral of an off resonant portion of the spectrum from the optical density integral. Fig. 4.6 shows an example of the trap-on lifetime vs. the trap-off lifetime for Ag, along with a fit to (4.3). At low buffer gas densities, loss from elastic collisions is dominant, while at high buffer gas densities, spin relaxation is dominant. At low He densities ($\tau_0 < 150$ ms), at 420 mK, the trap enhances atom lifetime by a factor of 20. By tuning the buffer gas density, we were able to trap Ag for up to 2.3 s and Cu for up to 5 s.

At 420 mK, we measured γ_R for Ag-^{3}He to be $3.2 \pm 0.2 \times 10^6$. For these collision studies we measure cell temperature using a solid-state thermometer. This agrees with the atom temperature obtained from spectra to within 30 mK over the time ranges for which we fit lifetimes. The quoted uncertainty in γ_R includes a 5% systematic uncertainty associated with this temperature measurement. At 310 mK, γ_R for Cu-^{3}He was $8.2 \pm 0.4 \times 10^6$.

We investigated the dependence of γ_R on temperature in the range 320 mK to 600 mK for Cu-^{3}He and Ag-^{3}He. The measurement is shown in Fig. 4.7. We find a strong temperature dependence for Ag-^{3}He, with power law exponent = 5.8±0.3 (stat.)±0.3 (sys.). The systematic uncertainty results from temperature measurement. The temperature de-

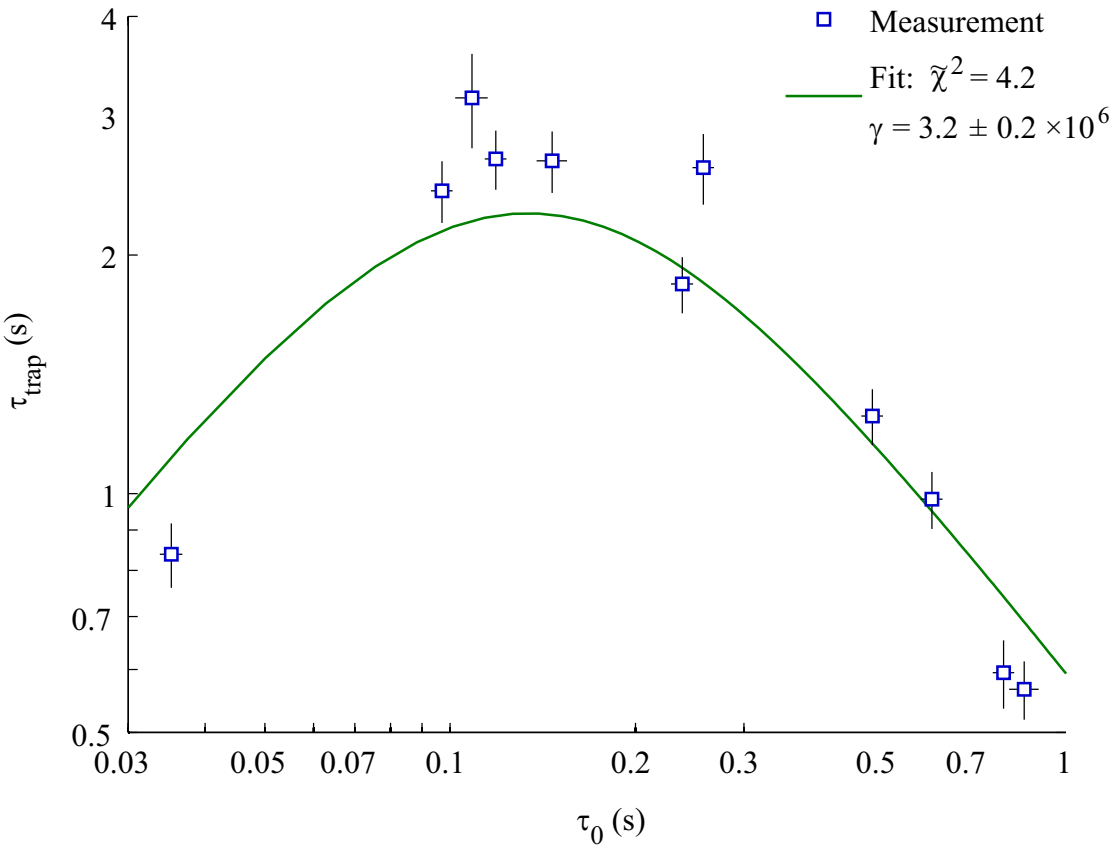

Figure 4.6: Ag trap-on lifetime vs. trap-off lifetime at 420 mK. The fit is to (4.3).

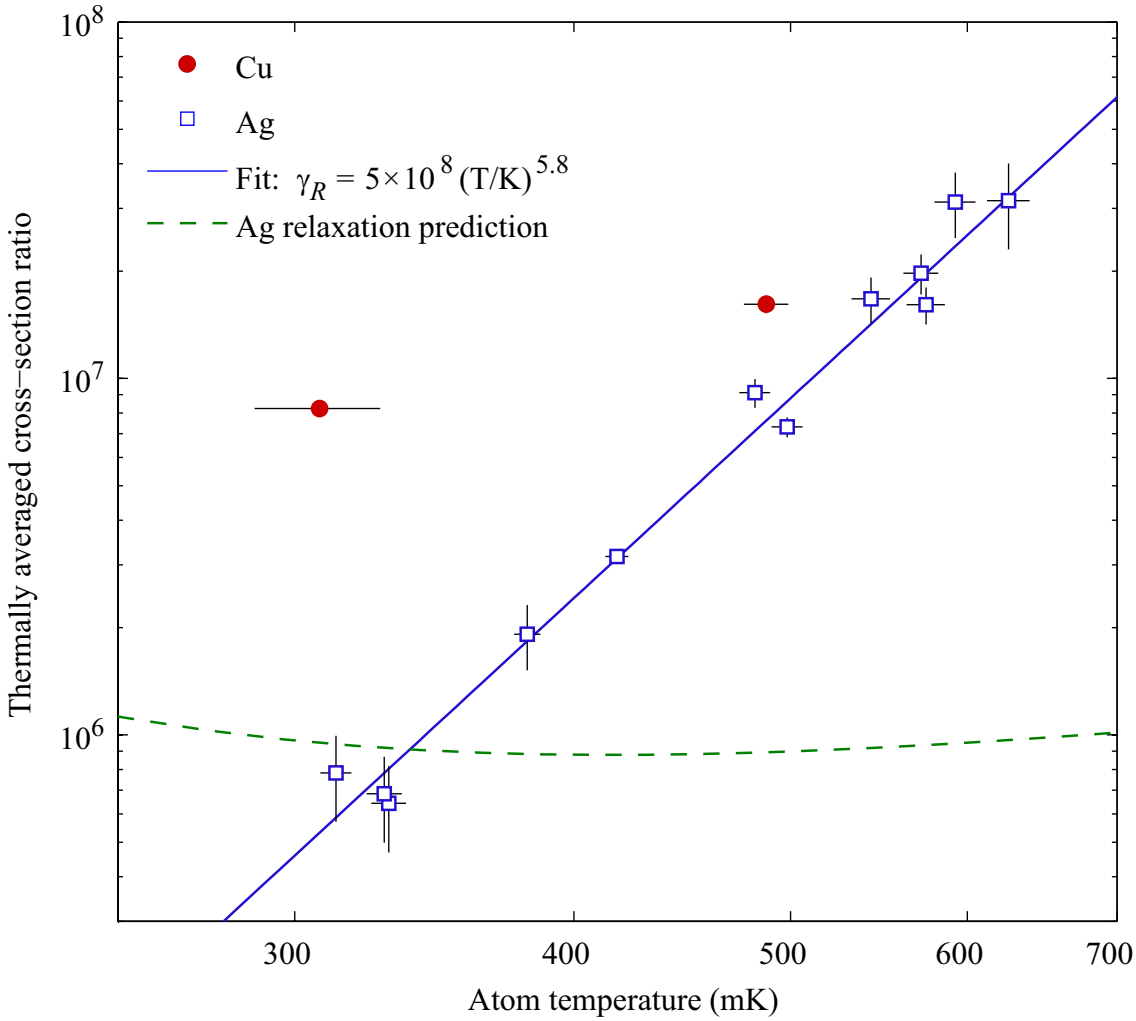

Figure 4.7: The measured ratio of thermally averaged transport cross-section, $\bar{\sigma}_D$, to thermally averaged relaxation cross-section, $\bar{\sigma}_R$, in a 4 T trap for Cu-^{3}He and Ag-^{3}He. The dashed line depicts a theoretical prediction for Ag-^{3}He. Both axes are logarithmic.

pendence of $\bar{\sigma}_D(T)$ for Ag-^{3}He was studied independently by measuring τ_0 vs. temperature, for a constant background gas density. We found that τ_0 did not depend significantly on temperature (varying by 20% between 420 mK and 600 mK). Because the thermal dependence of τ_0 is weak, we believe the strong temperature dependence of $\gamma_R(T)$ is due to temperature dependence of the relaxation cross-section $\bar{\sigma}_R(T)$.

We also investigated the cross-section ratio for Ag-^{3}He vs. magnetic field. At a constant temperature, the average field experienced by the trapped atoms scales linearly with trapping field. At 320 mK, for 2 T $< B_{\rm trap} <$ 4 T (equivalently, 1 T $< \langle B \rangle <$ 2 T), the cross-section ratio was measured to be $4.8 \pm 0.4 \times 10^6 \, (B_{\rm trap}/{\rm T})^{-0.9\pm0.2}$.

4.2.3 Anomalous spin relaxation

I compared the measured temperature dependence to a theoretical prediction of the Ag-^{3}He cross-section ratio. The dominant mechanism used to explain spin-relaxation in hydrogenlike (single valence s electron) atoms is the electron spin – molecular rotation interaction [3, 96, 97]. I generated a theoretical prediction for the Ag-^{3}He spin-relaxation cross-section ratio using the results of Walker *et al.* [3] and the Ag-He potentials of Takami and Jakubek [98]. For completeness I included the Fermi contact hyperfine interaction [99]. The result of this calculation (see App. C) is plotted on the dashed line in Fig. 4.7. At low temperatures the cross section decreases as T^{-1}. The weakly increasing behavior at higher temperatures is due to a scattering resonance at 0.07 meV. The absolute magnitude of γ_R may depend on details of the scattering potential. However, it is important to note that the power-law dependence of γ_R for these interactions must be less than T^2. This is because the strengths of these spin interaction effects are monotonically increasing functions of collision energy, save for the effect of possible scattering resonances. Resonances would give rise to the largest possible temperature dependence, T^2. We therefore conclude that the $\sim T^6$

dependence observed for Ag must be due to a heretofore neglected effect. One possibility is an anomalous rotation dependence of the interaction, such as has been observed in ground state YbF molecules [100].

We did not observe an anomalous temperature behavior for the cross-section ratio of Cu-^{3}He. The two data taken are consistent with the T^2 temperature dependence mentioned above. We did not make a theoretical prediction for the Cu-^{3}He cross-section ratio because we could not find suitable internuclear potentials in the literature.

4.3 Conclusions

We trapped 4×10^{13} Ag atoms for up to 2.3 s, and 3×10^{12} Cu atoms for up to 5 s. We developed a technique to measure transport to relaxation cross-section ratios that is independent of one's knowledge of buffer-gas density. This ratio was measured for the Ag-^{3}He and Cu-^{3}He systems. It was found to be large ($> 10^6$) in both cases. For Ag-^{3}He, an anomalously strong $T^{5.8}$ temperature dependence was discovered.

Our measurements of spin relaxation could indicate that atom-atom collisions in the trap would be favorable for evaporative cooling. By doubling η, either by increasing the cooling power of the experiment or by using a deeper magnetic trap (using a Nb_3Sn or Nb_3Al wound magnet, for example), these atoms could be thermally isolated from the trapping cell and evaporatively cooled. If so, dense samples of ultracold copper or silver could be produced using buffer gas loading.

Chapter 5

Prospects

We have shown that buffer gas cooling can be used to generate large trapped samples of 1 μ_B atoms, with up to 40 trillion atoms, with lifetimes between 3 and 200 s. The longest lifetimes are achieved when the buffer gas can be removed from the trapping volume.

Buffer gas removal is found to be possible when trapping ηs are larger than 10. This is in agreement with experiments performed with more strongly magnetic species [58]. While large samples of alkali atoms can be obtained using low laser ablation energies, and therefore low loading temperatures, this does not extend to species such as the noble metals. The best way to increase the applicability of buffer gas cooling among 1 μ_B species is to increase the loading η. If hot atom gases are to be produced via in situ laser ablation, deeper magnetic traps would need to be developed. Currently the trapping magnets used for buffer gas trapping are wound with NbTi superconducting wire. NbTi has a critical field of 15 K (at 0 K). Other materials, such as Nb_3Sn, have higher critical fields (25 K for Nb_3Sn), and could be used to make significantly deeper traps. However, these materials are brittle, and winding a magnet with one of these materials is not simply a matter of replacing the wire. A firing step is needed, putting restrictions on the materials used for

spacers and insulation. In addition, the resulting wire is brittle, and could be damaged by the large forces present within the magnet. An alternative tack to lowering η would be to produce the 1 μ_B species outside the cell, such as in a room-temperature supersonic beam [35], or a buffer gas cooled beam [55].

In order to evaporatively cool the 1 μ_B species we have trapped, we must achieve thermal isolation. This was not conclusively demonstrated in these experiments. To achieve thermal isolation, we must either reduce the thickness of adsorbed buffer gas films in the cell, or reduce the cell temperature to prevent them from desorbing. Adding a deeper magnet would allow for pumping of the buffer gas films at higher temperatures, leading to thinner films. Alternatively work could be done to improve thermal conductivity between the cell and the mixing chamber, in order to freeze the film.

Appendix A

Spectrum fitting

The buffer gas loading technique brings with it a set of data analysis challenges. Namely, the challenge of extracting meaningful atomic parameters from the spectra of atoms trapped in large quadrupole fields in the cold regime. This problem has been attacked since the birth of the technique, and is well described in [101] and [57].

In order to extract physical parameters such as atom number, temperature, and state distribution, we compare simulations of the atomic spectrum to observed spectra. By performing a chi-square fitting routine, we can extract best estimations of these parameters, together with statistical confidence intervals for these estimations. In this appendix, I first described details of the of the spectrum simulation. Since our spectrum simulation is similar to the algorithm presented by Weinstein in his thesis [57], it will only be necessary to discuss areas in which our simulation differs, or areas for which the description in [57] begs greater detail. I will discuss in detail three major components of the spectrum simulation: First, how the Zeeman energies of atoms are calculated in our simulation, with special attention to atoms displaying the Paschen-Back effect. Second, how we calculate transition probabilities between the atomic ground and excited state manifolds, including a calculation of the

"polarization factor" mentioned in Weinstein's thesis. Third, how we calculate the optical absorption by our laser cloud in general, when certain assumptions made in Weinstein's thesis are violated. After describing the spectrum simulation, I give a brief overview of the MATLAB code we use to execute the calculations.

A.1 Zeeman structure calculation

A general atomic Hamiltonian for an electronic state of a multi-level atom may be written as:

$$\mathscr{H}(\vec{B}) = E_{nl} + \mathscr{H}_{\mathrm{FS}} + \mathscr{H}_{\mathrm{HFS}} + \mathscr{H}_{\mathrm{Z}}(\vec{B}) \tag{A.1}$$

E_{nl} is the center of mass energy of the electronic state. $\mathscr{H}_{\mathrm{FS}}$ describes the fine structure of the atom associated with spin-orbit coupling, spin-spin coupling, and the like. $\mathscr{H}_{\mathrm{HFS}}$ describes the interaction of the nucleus with the electrons (hyperfine structure), and is always smaller than fine structure effects. $\mathscr{H}_{\mathrm{Z}}(\vec{B})$ describes the Zeeman effect of the state. Once this Hamiltonian has been constructed, one need only solve the eigensystem $\mathscr{H}(\vec{B})\psi_i(\vec{B}) = E_i(\vec{B})\psi_i(\vec{B})$ to find the energy levels and wavevectors at every $\vec{B}$. Quantum numbers may then be found in the usual manner, e.g. to find j: $j(j+1) = \langle\psi_i| \left(\vec{\mathbf{L}}+\vec{\mathbf{S}}\right)^2 |\psi_i\rangle$.

In practice, the atomic Hamiltonian in (A.1) can not be constructed in the same manner for all atoms. $\mathbf{J}^2$ commutes with the first three terms in the Hamiltonian, but not the Zeeman term. For most atoms, the Zeeman term is small compared to the fine structure term for experimentally realizable magnetic fields, and j is always a good quantum number. For these atoms, we will construct $\mathscr{H}(\vec{B})$ in the $|nilsm_i jm_j\rangle$ basis (called the j basis here). This is convenient because the coefficients we need to construct the atomic Hamiltonian are universally published in the j basis. In addition, fine structure reduces to a simple diagonal matrix in this basis.

For light atoms, such as helium or lithium, the fine structure term is small, and experimentally realizable fields (0.4T for hydrogen) can cause the Zeeman term to become as large as the fine structure term. In this case, j is no longer a good quantum number, and we must use the $|nilsm_i m_l m_s\rangle$ basis (the ls basis). The challenge becomes that of constructing the ls basis Hamiltonian from published j basis coefficients and g-factors.

A.1.1 Fine structure term

$\mathscr{H}_{\mathrm{FS}}$ folds in all splittings between various j states at zero field. These splittings can arise from many sources: spin-orbit coupling, Lamb shift, jj coupling, etc.

In the j basis, the elements of $\mathscr{H}_{\mathrm{FS}}$ diagonal in j are described by constant diagonal (in m_j) matrices:

$$\mathscr{H}_{\mathrm{FS};j} = f_j \tag{A.2}$$

For example, for $l = 1$, $s = 1/2$, the Hamiltonian[1] in the j, m_j basis is:

$$\mathscr{H}_{\mathrm{FS}} = \begin{bmatrix} f_{3/2} & 0 & 0 & 0 & \cdot & \cdot \\ 0 & f_{3/2} & 0 & 0 & \cdot & \cdot \\ 0 & 0 & f_{3/2} & 0 & \cdot & \cdot \\ 0 & 0 & 0 & f_{3/2} & \cdot & \cdot \\ \cdot & \cdot & \cdot & \cdot & f_{1/2} & 0 \\ \cdot & \cdot & \cdot & \cdot & 0 & f_{1/2} \end{bmatrix}$$

For simple interactions like spin-orbit coupling, the off-diagonal terms will be 0. In general, because j is a "good" quantum number of $\mathscr{H}_{\mathrm{FS}}$, the off-diagonal terms will be quite small.

[1] By convention, the elements in Hamiltonians in this section are of block form in the first quantum number, and checkered in the last quantum number. In the example Hamiltonian, the columns from left to right are (in $|jm_j\rangle$) $\left|\frac{3}{2}\,\frac{3}{2}\right\rangle$ $\left|\frac{3}{2}\,\frac{1}{2}\right\rangle$ $\left|\frac{3}{2}\,-\frac{1}{2}\right\rangle$ $\left|\frac{3}{2}\,-\frac{3}{2}\right\rangle$ $\left|\frac{1}{2}\,\frac{1}{2}\right\rangle$ $\left|\frac{1}{2}\,-\frac{1}{2}\right\rangle$.

Regardless, when we may use the j basis, levels of different j do not cross, and so we need not worry about terms of the Hamiltonian that couple different j.

For light one-electron atoms such as hydrogen or lithium, fine structure arises predominantly from spin-orbit coupling. In this case the Hamiltonian is simply written

$$\mathscr{H}_{\mathrm{FS}} = f\vec{\mathbf{L}} \cdot \vec{\mathbf{S}}. \tag{A.3}$$

We typically ignore the Lamb shift, but if it is important it can be included like any other effect using the method in the following paragraph.

For more complicated atoms displaying the Paschen-Back effect (such as helium), the situation becomes more difficult. We are given a set of $\{f_j\}$. First, we use Clebsch-Gordon coefficients to construct a rotation matrix from the ls basis to the j basis. For each j level:

$$\left|\psi_{jm_j}\right\rangle = \sum_{m_l,m_s} a_{jm_jm_lm_s} \left|\psi_{m_lm_s}\right\rangle. \tag{A.4}$$

We construct a fine structure Hamiltonian $\mathscr{H}_{\mathrm{FS}}$ in the ls basis, with unknown matrix elements, and require the following:

1. $\mathscr{H}_{\mathrm{FS}}$ is a symmetric tensor.
2. $\forall j \forall m_j : \left\langle\psi_{jm_j}\right| \mathscr{H}_{\mathrm{FS}} \left|\psi_{jm_j}\right\rangle = f_j$

   where (A.4) is used to convert $\left|\psi_{jm_j}\right\rangle$ to the ls basis.
3. $[\mathscr{H}_{\mathrm{FS}}, \mathbf{J}^2] = 0$.
4. $[\mathscr{H}_{\mathrm{FS}}, \vec{\mathbf{J}}_z] = 0$.

Note that $\mathbf{J}^2$ is constructed in the ls basis as $(\vec{\mathbf{L}} + \vec{\mathbf{S}})^2$ and $\vec{\mathbf{J}}_z$ as $\mathbf{L}_z + \mathbf{S}_z$. Combining all these requirements yields a system of linear equations that can be solved for the matrix elements of $\mathscr{H}_{\mathrm{FS}}$.

A.1.2 Hyperfine structure term

Hyperfine structure arises from nucleus–electron interactions. In practice only two of these interactions are significant: the nuclear magnetic dipole and nuclear electric quadrupole interactions.

The nuclear magnetic dipole interaction

The nuclear magnetic dipole interaction is [102]

$$\mathscr{H}_{\mathrm{M1}} = -\vec{\mu}_I \cdot \vec{B}_e \tag{A.5}$$

where $\vec{\mu}_I = \mu_N \vec{\mathbf{I}}$ is the magnetic moment of the nucleus, and $\vec{B}_e$ is the field at the nucleus arising from the electron. $\vec{B}_e$ arises both from the orbit of the electron about the nucleus and from the electron spin dipole.

The field from the electron orbit is[103]

$$\vec{B}(r)_{\mathrm{L}} = \frac{\mu_B}{r^3}\vec{\mathbf{L}} \tag{A.6}$$

while the electron spin dipole field is[103]

$$\vec{B}(r)_{\mathrm{S}} = \mu_B \left[\frac{(3\vec{\mathbf{S}}\cdot \hat{r})\hat{r} - \vec{\mathbf{S}}}{r^3} + \frac{8\pi}{3}\vec{\mathbf{S}}\delta^3(\vec{r}) \right]. \tag{A.7}$$

In the ls basis, we will break the Hamiltonian into two terms, one associated with $\vec{\mathbf{L}}$, and one with $\vec{\mathbf{S}}$.

The first term is

$$\mathscr{H}_{\mathrm{M1};\,\vec{\mathbf{L}}} = a_l \vec{\mathbf{I}} \cdot \vec{\mathbf{L}} \tag{A.8}$$

$$a_l = -\langle nli| \frac{\mu_I \mu_B}{r^3} |nli\rangle$$

a_l does not depend on any of m_i, m_l, or m_s.

To deal with the second term, we project the term $(\vec{\mathbf{S}}\cdot\vec{r})\vec{r}$ onto $\vec{\mathbf{S}}$. The Wigner-Eckart theorem allows us to project any tensor operator A onto any other tensor operator that transforms in the same manner under rotations. By "project" we mean that expectation values of A in a state $|jm_j\rangle$ may be written as a product of two terms. The first term is a constant for a given j, regardless of the value of m_j. The second term includes all dependence on m_j, and does not depend on A. In the special case of vector operators, this second term is the Clebsch-Gordon series.

In constructing the $\vec{\mathbf{S}}$ hyperfine term we use the fact that $(\vec{\mathbf{S}}\cdot\vec{r})\vec{r}$ is a vector operator. Using the Wigner-Eckart theorem, we can write its expectation values in terms of a projection on $\vec{\mathbf{S}}$ [51, pp. 522-4]:

$$\langle sm_s'|(\vec{\mathbf{S}}\cdot\vec{r})\vec{r}|sm_s\rangle = \frac{\langle ss|(\vec{\mathbf{S}}\cdot\vec{r})^2|ss\rangle}{s(s+1)}\langle sm_s'|\vec{\mathbf{S}}|sm_s\rangle \tag{A.9}$$

Because $[\vec{\mathbf{I}},\vec{\mathbf{S}}]=0$, we can substitute (A.9) into (A.7), yielding the $\vec{\mathbf{S}}$ term of the magnetic hyperfine Hamiltonian:

$$\mathscr{H}_{\mathrm{M1};\,\vec{\mathbf{S}}} = a_s\vec{\mathbf{I}}\cdot\vec{\mathbf{S}} \tag{A.10}$$

$$a_s = -\langle nlss|\frac{\mu_I\mu_B}{s(s+1)}\left[\frac{3(\vec{\mathbf{S}}\cdot\vec{r})^2 - r^2\mathbf{S}^2}{r^5} + \frac{8\pi}{3}\mathbf{S}^2\delta^3(\vec{r})\right]|nlss\rangle$$

Because the electronic state has a fixed value of s, this Hamiltonian applies for every eigenstate. Finally,

$$\mathscr{H}_{\mathrm{M1}} = a_l\vec{\mathbf{I}}\cdot\vec{\mathbf{L}} + a_s\vec{\mathbf{I}}\cdot\vec{\mathbf{S}}. \tag{A.11}$$

In the j basis the calculation is similar; we now project both the $\vec{\mathbf{L}}$ and the $\vec{\mathbf{S}}$ terms onto $\vec{\mathbf{J}}$ using the Wigner-Eckart theorem:

$$\mathscr{H}_{\mathrm{M1};\,j} = a_j\vec{\mathbf{I}}\cdot\vec{\mathbf{J}} \tag{A.12}$$

$$a_j = -\langle nljj|\frac{\mu_I\mu_B}{j(j+1)}\frac{\vec{\mathbf{J}}\cdot\vec{\mathbf{L}}}{r^3}|nljj\rangle$$

$$-\langle nljj|\frac{\mu_I\mu_B}{j(j+1)}\left[\frac{3\vec{\mathbf{J}}\cdot(\vec{\mathbf{S}}\cdot\vec{r})\vec{r}-r^2\vec{\mathbf{J}}\cdot\vec{\mathbf{S}}}{r^3}+\frac{8\pi}{3}\vec{\mathbf{J}}\cdot\vec{\mathbf{S}}\delta^3(\vec{r})\right]|nljj\rangle$$

Note that this analysis only holds for terms of the Hamiltonian that are *diagonal in* j. Because $\mathbf{J}^2$ does not commute with $\mathscr{H}_{\mathrm{M1}}$, these off-diagonal terms may be of similar size to the on-diagonal terms. But again, since a condition for using the j basis is that different j levels do not interact, we can ignore the off-diagonal terms.

The nuclear electric quadrupole interaction

We also consider the electric quadrupole interaction. This interaction can be written:

$$\mathscr{H}_{\mathrm{E2}} = -\sum_{m=-2}^{2} Q_m V_m \tag{A.13}$$

Q and V are spherical harmonic multipole expansions; Q is the 2nd-rank tensor describing the electric quadrupole moment of the nucleus, and V is the 2nd-rank tensor describing the electron electric potential.[102]

Ramsey [102] shows how the Wigner-Eckart theorem can be used to project Q onto the nuclear spin $\vec{\mathbf{I}}$, and to project V onto $\vec{\mathbf{J}}$. The result is:

$$\mathscr{H}_{\mathrm{E2};j} = b_j\frac{3(\vec{\mathbf{I}}\cdot\vec{\mathbf{J}})^2+\frac{3}{2}\vec{\mathbf{I}}\cdot\vec{\mathbf{J}}-\mathbf{I}^2\mathbf{J}^2}{2i(2i-1)j(2j-1)} \tag{A.14}$$

$$b_j = -\langle ii|\vec{\rho}_N(3z^2-r^2)|ii\rangle\langle jj|\vec{\rho}_e\frac{3z^2-r^2}{r^5}|jj\rangle$$

Because V is specified by the orbital angular momentum $\vec{\mathbf{L}}$ of the electron, we could project V on $\vec{\mathbf{L}}$ instead of on $\vec{\mathbf{J}}$. Doing this gives us the ls basis Hamiltonian:

$$\mathscr{H}_{\mathrm{E2}} = b_l \frac{3(\vec{\mathbf{I}}\cdot\vec{\mathbf{L}})^2 + \frac{3}{2}\vec{\mathbf{I}}\cdot\vec{\mathbf{L}} - \mathbf{I}^2\mathbf{L}^2}{2i(2i-1)j(2j-1)} \tag{A.15}$$

$$b_l = -\langle ii|\vec{\rho}_N(3z^2 - r^2)|ii\rangle\langle ll|\vec{\rho}_e\frac{3z^2 - r^2}{r^5}|ll\rangle$$

Note specifically that when $\vec{\mathbf{L}} = 0$, there should be no quadrupole contribution to the hyperfine splitting (in the j basis, we would expect $\forall j\ b_{ij} = 0$). This can be violated in heavy atoms, for which filled electron shells can contribute to the hyperfine effect.

A.1.3 Zeeman term

The Zeeman term in the ls basis is:[51]

$$\mathscr{H}_{\mathrm{Z}} = \mu_B\vec{B}\cdot\vec{\mathbf{L}} + 2\mu_B\vec{B}\cdot\vec{\mathbf{S}} \tag{A.16}$$

The canonical application of the Wigner-Eckart theorem is that of writing the Zeeman term in the j basis. The result is:

$$\mathscr{H}_{\mathrm{Z};j} = g_j\mu_B\vec{B}\cdot\vec{\mathbf{J}} \tag{A.17}$$

$$g_j = 1 + \frac{j(j+1) - l(l+1) + s(s+1)}{2j(j+1)}; \tag{A.18}$$

For heavy atoms the actual g_j may depart from (A.18). The theoretical equation (A.16) will always be applicable for atoms in which we must use the ls basis, because such atoms are always light.

A.1.4 Determining coefficients of the j and ls basis Hamiltonians

In the j basis, the complete Hamiltonian is:

$$\boxed{\mathscr{H}_j = E_{nl} + f_j + a_j\vec{\mathbf{I}}\cdot\vec{\mathbf{J}} + b_j\frac{3(\vec{\mathbf{I}}\cdot\vec{\mathbf{J}})^2 + \frac{3}{2}\vec{\mathbf{I}}\cdot\vec{\mathbf{J}} - \mathbf{I}^2\mathbf{J}^2}{2i(2i-1)j(2j-1)} + g_j\mu_B\vec{B}\cdot\vec{\mathbf{J}}} \tag{A.19}$$

For most atoms, all the coefficients E_{nl}, f_j, a_j, b_j and g_j will be published in the literature, typically as experimental measurements. For some of the more esoteric transitions, however, E_{nl} (as an isotope shift), a_j or b_j may be unavailable in one or both of the ground or excited states. In this case, one may calculate the coefficients by measuring the zero-field spectrum of the transition. Frequency can be measured using either a known splitting (typically ground state hyperfine structure) or a Fabry-Perot cavity. We index the manifold of ground states by m and that of the excited states by n. Choosing test values for the unknown coefficients gives model energies for the energies of these states, E_m and E_n respectively. The coefficients can then be fit, by minimizing

$$\chi^2 = \sum_{mn} [h\nu_{mn} - (E_n - E_m) + a]^2$$

where the sum is on all measured transitions between states m and n, and ν_{mn} is the measured frequency of the transition. a is an unknown energy offset, constant across all m and n.

It is tempting to construct the ls basis Hamiltonian by performing a basis transformation on the j basis Hamiltonian. Doing so is impossible, however. In projecting various interactions onto the $\vec{\mathbf{J}}$ operator, we found only the elements of the j basis Hamiltonian that were diagonal in j — that is, those elements which do not couple states of different j. Because $\vec{\mathbf{J}}$ does not commute with $\mathscr{H}_{\mathrm{HFS}}$, and may, for some atoms, not even commute perfectly with $\mathscr{H}_{\mathrm{FS}}$, these off-diagonal terms are non-zero — and unknown. Assuming these off-diagonal terms are so small as to be ignored will cause quantum numbers (usually f, and the various m numbers) to be misassigned, causing the wrong number of predicted peaks at the wrong frequencies. Hence it is necessary to construct the ls basis Hamiltonian from the theory developed in this section.

The complete ls basis Hamiltonian is:

$$\boxed{\mathscr{H}_{ls} = E_{nl} + \mathscr{H}_{FS} + a_l \vec{\mathbf{I}}\cdot\vec{\mathbf{L}} + a_s \vec{\mathbf{I}}\cdot\vec{\mathbf{S}} + b_l \frac{3(\vec{\mathbf{I}}\cdot\vec{\mathbf{L}})^2 + \frac{3}{2}\vec{\mathbf{I}}\cdot\vec{\mathbf{L}} - \mathbf{I}^2\mathbf{L}^2}{2i(2i-1)l(2l-1)} + \mu_B \vec{B}\cdot\vec{\mathbf{L}} + 2\mu_B \vec{B}\cdot\vec{\mathbf{S}}} \tag{A.20}$$

For atoms in which $\mathscr{H}_{FS} = f\vec{\mathbf{L}}\cdot\vec{\mathbf{S}}$, the structure of $\mathscr{H}_{ls}$ is known except for four scalar coefficients, f, a_l, a_s, and b_l. For atoms with more complicated $\mathscr{H}_{FS}$, the situation is the same, except that slightly more coefficients are unknown. Because the eigenenergies of $\mathscr{H}_{ls}$ must be identical to the eigenenergies of $\{\mathscr{H}_j\}$ at zero field, we can determine the unknown coefficients by varying them until both Hamiltonians yield the same eigenenergies. This is done using a least squares fit, minimizing the least squares difference between the eigenenergies of $\mathscr{H}_{ls}$ and of $\{\mathscr{H}_{j=|l-s|}, \ldots, \mathscr{H}_{l+s}\}$ at zero field.

A.2 Transition probabilities

Of all the possible pairs of ground and excited states, only a few will be coupled optically. Furthermore, the rate at which atoms will make transitions between two states will depend on many factors: the differences of energies of the states, the quantum numbers of both states, and the polarization of the incoming light.

It will be useful to consider the "optical cross-section" for a transition. Given an incoming light beam of polarization vector $\hat{\epsilon}$ and frequency ω, the cross-section $\sigma_{k'k}(\hat{\epsilon}, \omega)$ describes the probability per unit time $p_{k'k}$ that an atom makes a transition between a ground state k and an excited state k': [51, p. 451]

$$p_{k'k}(\hat{\epsilon}, \omega) = \sigma_{k'k}(\hat{\epsilon}, \omega, \vec{B}) \frac{d\dot{N}_\gamma}{dA}(\hat{\epsilon}, \omega) \tag{A.21}$$

where $d\dot{N}_\gamma/dA = I_0/h\nu$ is the incident photon flux. The cross-section is independent of both light intensity and atom density. However, the cross-section can depend on external parameters such as magnetic field. This is because the quantum numbers of a state may

vary with external field (the energy difference between ground and excited states remains effectively constant versus field, for optical transitions). The relative intensity I/I_0 (a.k.a. the "transmission") of a light beam of polarization $\hat{\epsilon}$ passing through a sample of atoms of density n_k (for each ground state k) and of length L can be found by integrating the scattering rate in (A.21): [57, p. 150]

$$\ln\left[\frac{I}{I_0}(\hat{\epsilon},\omega,\vec{\rho})\right] = -\sum_{k'k}\int_z n_k(\vec{r})\sigma_{k'k}(\hat{\epsilon},\omega,\vec{B}(\vec{r}))dz \tag{A.22}$$

$$\equiv -OD(\hat{\epsilon},\omega,\vec{\rho}) \tag{A.23}$$

Here the z axis of a cylindrical coordinate system has been chosen to lie along the axis of laser propagation; $\vec{\rho}$ describes positions transverse to the laser axis. The quantity in (A.23) is defined as a matter of convenience; it is called the "optical density".

The polarization of the light field, $\hat{\epsilon}$, can be thought of as a vector with $l_\epsilon = 1$ and $m_\epsilon \equiv q \in \{-1, 0, 1\}$. Note that the quantization axis is always chosen along the direction of the local magnetic field. Because the direction of the magnetic field varies with position in the trap, the fraction of the light field with polarization $\hat{\epsilon}_q$ will also vary with position. To take this quantization of the light polarization into account, we slightly alter the definition of optical density as follows:

$$\begin{aligned}\frac{I}{I_0}(\omega,\vec{\rho}) &= \sum_q \exp(-OD_q(\omega,\vec{\rho})) \\ &= \sum_q \exp\left(-\int_z \sum_{kk'} C_q(\vec{r})n_k(\vec{r})\sigma_{k'kq}(\omega,\vec{B}(\vec{r}))dz\right)\end{aligned} \tag{A.24}$$

We will now take this equation as the defining equation of optical density. Now the intensity

I of the transmitted beam is integrated over all polarizations $\hat{\epsilon}_q$. $C_q(\vec{r})$ is the local fraction of the light field having polarization $\hat{\epsilon}_q$ at location $\vec{r}$; it is called the "polarization factor".

A.2.1 Optical cross-section

In order to determine $n_k(z, \vec{r})$ from measured transmission, which in turn yields information about atom number, temperature, and state distribution, we must calculate $\sigma_{k'kq}(\omega, \vec{B}(\vec{r}))$. Such a calculation is made by applying time-dependent perturbation theory to a two-state Hamiltonian; the states interact by the dipole interaction of the electron and the electric field of the incident light. The details of the calculation can be found in [104, pp. 530-3].

First we will consider the cross-section between states of definite l, m_l, s, m_s states. The cross-section can be separated into a radial expectation value and an angular expectation value. The cross-section is:

$$\sigma_{l'm_l's'm_s'lm_lsm_sq}(\omega, \vec{r}) = \frac{3\lambda^2}{2\pi} \frac{\Gamma^2/4}{(\omega - \omega_0)^2 + \Gamma^2/4} |\mathscr{A}_{l'm_l's'm_s'lm_lsm_sq}|^2 \tag{A.25}$$

ω_0 represents the resonant frequency of the transition. The resonant frequency of a transition between two states is proportional to the energy splitting between the states:

$$\omega_{0k'k}(\vec{B}(\vec{r})) = \frac{E_{k'}(\vec{B}(\vec{r})) - E_k(\vec{B}(\vec{r}))}{\hbar} \tag{A.26}$$

$\mathscr{A}_{l'm_l's'm_s'lm_lsm_sq}$ refers to the angular part of the optical cross-section. The angular term describes the coupling of the light polarization with the angular momentum of the electron. It is the normalized probability amplitude for adding the ground state electronic angular momentum $\vec{\mathbf{L}}$ with the light angular momentum $\hat{\epsilon}_q$ to yield the excited state electronic

angular momentum $\vec{\mathbf{L}}'$. The angular term is: [25, §4.5]

$$\begin{aligned}\mathscr{A}_{l'm_l's'm_s'lm_lsm_sq} &= \langle l'm_l's'm_s'|\hat{\epsilon}_q\cdot\hat{r}|lm_lsm_s\rangle \\ &= (-1)^{l'-m_l'}\sqrt{max(l,l')}\begin{pmatrix} l' & 1 & l \\ -m_l' & q & m_l\end{pmatrix}\delta_{l',l\pm1}\delta_{s's}\delta_{m_s'm_s}\end{aligned} \tag{A.27}$$

The expression in parentheses is a Wigner 3-j symbol (described in [105, §5.1]). It describes the z projection of the addition of $\vec{\mathbf{L}}$ with the light angular momentum. Its presence enforces the selection rule $\delta_{m_l'm_l+q}$.

In general a ground or excited eigenstate will not have definite values of m_l or m_s; instead the eigenstate will be a linear combination of states with definite quantum numbers. Such a state $|k\rangle$ will depend on the external field. We write for the ground state $|k\rangle$ and excited state $|k'\rangle$:

$$\left|k(\vec{B})\right\rangle = \sum_{m_lm_s} a_{m_lm_s}(\vec{B})\,|lm_lsm_s\rangle \tag{A.28}$$

$$\left|k'(\vec{B})\right\rangle = \sum_{m_l'm_s'} b_{m_l'm_s'}(\vec{B})\,|l'm_l's'm_s'\rangle \tag{A.29}$$

The values of $a_{m_lm_s}(\vec{B})$ and $b_{m_l'm_s'}(\vec{B})$ are obtained by diagonalizing the ls basis Hamiltonian at field $\vec{B}$. Armed with (A.28) and (A.29), we can now write the angular part of

$\sigma_{kk'}(\hat{\epsilon}_q, \omega, \vec{B})$:

$$\begin{aligned}
\mathscr{A}_{k'kq}(\vec{B}) &= \langle k'(\vec{B})|\hat{\epsilon}_q \cdot \hat{r}|k(\vec{B})\rangle \\
&= \sum_{\substack{m_l' m_s' \\ m_l m_s}} a_{m_l m_s}(\vec{B}) b^*_{m_l' m_s'}(\vec{B}) \langle m_l' m_s'|\hat{\epsilon}_q \cdot \hat{r}|m_l m_s\rangle \\
&= \sum_{m_l m_s} (-1)^{l'-m_l-q} a_{m_l m_s}(\vec{B}) b^*_{m_l+q;m_s}(\vec{B}) \\
&\qquad \times \sqrt{max(l,l')} \begin{pmatrix} l' & 1 & l \\ -m_l-q & q & m_l \end{pmatrix} \delta_{l',l\pm1}\delta_{s's}
\end{aligned} \tag{A.30}$$

Thus we have successfully calculated the optical cross-section when the eigenstates of $\mathscr{H}$ are known in terms of an expansion of ls states.

For many, if not most atoms, we diagonalize a j basis Hamiltonian. In this case the eigenstates of $\mathscr{H}$ are known in terms of an expansion of j states. In this case the angular term must also take into account the relationship between $\vec{\mathbf{L}}$, $\vec{\mathbf{S}}$, and $\vec{\mathbf{J}}$. This calculation is performed in [25, §4.5.4]. The result is quoted here:

$$\begin{aligned}
\mathscr{A}_{k'kq}(\vec{B}) &= \sum_{\substack{j' m_j' \\ j m_j}} a_{j m_j}(\vec{B}) b^*_{j' m_j'}(\vec{B}) \langle j' m_j'|\hat{\epsilon}_q \cdot \hat{r}|j m_j\rangle \\
&= \sum_{j' j m_j} (-1)^{l'+s-m_j-q} a_{j m_j}(\vec{B}) b^*_{j';m_j+q}(\vec{B}) \sqrt{(2j+1)(2j'+1)} \\
&\qquad \times \begin{Bmatrix} s' & l' & j' \\ 1 & j & l \end{Bmatrix} \begin{pmatrix} j' & 1 & j \\ -m_j-q & q & m_j \end{pmatrix} \delta_{l',l\pm1}\delta_{s's}
\end{aligned} \tag{A.31}$$

The term in brackets is a Wigner 6-j symbol (described in [105, §5.1]). The 3-j symbol enforces the selection rules $j' \in \{j, j \pm 1\}$ and $m'_j = m_j + q$.

A.2.2 The polarization factor

The polarization factor is described in [57, pp. 151-154], but no expression for it is given. In this section we will derive the local polarization factor C_q for linearly polarized light fields.

First we'll set a Cartesian coordinate system based on the trap and on the polarization of the probe laser. Choose $\hat{\mathbf{x}}$ to be parallel to the laser polarization, $\hat{\mathbf{z}}$ to be along the trap axis, and $\hat{\mathbf{y}}$ to be orthogonal to $\hat{\mathbf{x}}$ and $\hat{\mathbf{y}}$. The origin is the trap center. At any point (x, y, z) in the trap,

$$\hat{\epsilon} = \hat{\mathbf{x}}. \tag{A.32}$$

We wish to project the laser polarization onto the local $\vec{\mathbf{J}}$. In the Cartesian coordinate system just defined, the local magnetic field is:

$$\hat{\mathbf{B}} = \sin\theta\cos\phi\hat{\mathbf{x}} + \sin\theta\sin\phi\hat{\mathbf{y}} + \cos\theta\hat{\mathbf{z}} \tag{A.33}$$

where

$$\theta \equiv \arccos\frac{B_z}{B} \tag{A.34}$$

$$\phi \equiv \arctan\frac{B_y}{B_x}. \tag{A.35}$$

Define C_0, C_1 and C_{-1} to be the projections of $\hat{\epsilon}$ onto Y_{10}, Y_{11} and Y_{1-1}, respectively. Symmetry or the Wigner-Eckart theorem can alternately be exploited to show

$$C_0 = \left|\left\langle \hat{\epsilon}\cdot\hat{\mathbf{J}}\right\rangle\right|^2 = \left|\left\langle \hat{\epsilon}\cdot\hat{\mathbf{B}}\right\rangle\right|^2 \tag{A.36}$$

Using this and $\sum_{q=-1}^{1} C_q = 1$:

$$\begin{aligned} C_0 &= \sin^2\theta\cos^2\phi \\ C_{\pm 1} &= \frac{1-\sin^2\theta\cos^2\phi}{2}. \end{aligned} \tag{A.37}$$

A.3 Integrating optical density

We would like to use light fields to measure properties of our trapped atoms. Typically we are interested in the number profile and temperature of the trapped atom distribution; we may also be concerned with the state distribution of the atom sample. All these parameters affect only the term $n_k(\vec{r})$ in equation (A.24).

Atoms will ergotically explore the spatial dimensions of the trap. If atom density is sufficiently large, collisions will maintain the atoms in translational thermal equilibrium. Thermal equilibrium will not be maintained between the quantum states of each atom, however. Because we are trapping on low-field seeking states, this is in fact a requirement for trapping; since high-field seeking states are of lower energy than low-field seeking states, thermalization of the quantum states will cause trap loss.

The density term $n_k(\vec{r})$ should be represented in a manner that reflects these thermal properties. The translational distribution will follow a Maxwell-Boltzmann distribution, while the state distribution will be strongly biased to trapped states. We'll let R_k represent the ratio of atom density in a ground state k at $\vec{r} = 0$, to the total atom density. Then the atom density is:

$$n_k(\vec{r}) = R_k n_0 e^{-(E_k(\vec{r}) - E_k(0))/k_B T} \tag{A.38}$$

Here n_0 is the atom density (integrated over all states) at $\vec{r} = 0$. $E_k(\vec{r})$ is the eigenenergy of state k at position $\vec{r}$, and T is the atom translational temperature. The total atom number

is just the integrated density over all states and positions:

$$N = \int \sum_k n_k(\vec{r}) d^3\vec{r} \tag{A.39}$$

We would like to use (A.24) to connect the measured transmission of a light beam through the trapped sample with the physical parameters of $n_k(\vec{r})$. How exactly this is done will depend on the experimental method used to measure transmission. Transmission can either be measured via absorption spectroscopy, or via laser induced fluorescence (which directly measures some geometry-dependent fraction of absorbed light). In this section we will consider specifically absorption spectroscopy, where the transmission of a narrow-line laser beam is measured using a spatially-insensitive detection device, typically a photomultiplier tube. The linewidth of the laser is narrow compared to the natural lifetime Γ of the transition. Because of this we may consider the laser to have a specific frequency ω. A beam splitter is used to divert part of the laser before it passes through the atom sample — this is used to measure the incident intensity I_0. After passing through the atom cloud the beam has intensity I. We divide the signal on the detector located after the atom sample (the "signal" detector) by the signal on the detector before the atom sample (the "reference" detector). This division is normalized to unity when no atoms are present; the normalized divided signal is then:

$$D = \frac{\int I(\omega, \vec{\rho}) d\vec{\rho}}{\int I_0(\omega, \vec{\rho}) d\vec{\rho}} \tag{A.40}$$

It will be useful to make some approximations. The first, and perhaps most egregious, is that the profile of the laser beam is a circular flat-top distribution, of diameter w. By this approximation, the reference signal is:

$$\int I_0(\omega, \vec{\rho}) d\vec{\rho} = I_0 \frac{\pi w^2}{4} \tag{A.41}$$

The second approximation is that the laser is linearly polarized. To some degree this can be ensured by running the beam through a polarizer before sending it to the

atom sample. However, if the beam passes through any birefringent elements between the polarizer and the detector, this polarization will be transformed to an elliptical polarization. In our experiment, the beam passed through three glass windows, and a sapphire window, twice, so the incoming beam certainly has elliptical polarization to some degree. If the beam is retroreflected through the atom sample, this polarization is inverted, and any effects of birefringence will be canceled out (assuming the laser is not significantly attenuated by either the atom sample or the retroreflecting mirror). This is done in our experiment, so the linear polarization approximation is valid. Because the beam is retroreflected, the integral in the exponential of (A.24) is performed twice, so the OD is doubled.

We will also assume that the optical depth for any one laser polarization q is small. This allows us to carry integrals through the exponential in (A.24). Note that, when the trap is on, we typically measure optical depths of 0.3 or less. An effect of this assumption is that atomic absorption does not change the polarization of the laser. Note that in solenoid or Helmholtz fields, the optical depth in one polarization can be quite large. In this case the atoms change the polarization of the laser; for instance a linearly polarized beam travelling through a sample of atoms in a field axial to the laser will become circularly polarized (in the non-adsorbing polarization) if the optical depth is large enough. As a consequence, the maximum absorption that can be measured in such a situation is 50%.

Putting all these approximations together, we can equate the measured divide with an integration over optical density. It will be useful to define the coordinate system of (A.24) such that the trap axis lies at $\vec{\rho} = 0$. For magnetic fields arising from axially aligned current loops, $|\vec{B}|$ does not depend on ϕ in this coordinate system. In this case $n_k(\vec{\rho}) = n_k(\rho, z)$, and $\sigma_{k'kq}(\omega, \vec{r}) = \sigma_{k'kq}(\omega, \rho, z)$. The only remaining component of OD that depends on the angle, ϕ, is the quantity $C_q(\vec{r})$.

The divide is:

$$\begin{aligned} D(\omega) &= \frac{4}{I_0 \pi w^2} \int I(\omega, \rho, \phi) \rho d\rho d\phi \\ &= \sum_q \int e^{-OD_q(\omega, \vec{\rho})} \rho d\rho d\phi \end{aligned} \tag{A.42}$$

Since $OD_q \ll 1$, we can bring the integral in ϕ through the exponential:

$$\begin{aligned} D(\omega) &= 2\pi \sum_q \int \exp\left(- \int OD d\phi / 2\pi \right) \rho d\rho \\ &= 2\pi \sum_q \int \exp\left(-\frac{1}{\pi} \int \int C_q(z, \rho, \phi) d\phi \sum_{k'k} n_k(\rho, z) \sigma_{k'kq}(\omega, \vec{B}(\rho, z)) dz \right) \rho d\rho \end{aligned} \tag{A.43}$$

This is done as a computational simplification. Because the quantity $\int C_q(\vec{r}) d\phi$ can be calculated analytically, this simplification removes one numerical integration from the problem. We shall define

$$\bar{C}_q(\rho, z) = \frac{1}{2\pi} \int C_q(\rho, z, \phi) d\phi. \tag{A.44}$$

Because the laser polarization does not change through the trap, $\bar{C}_q$ depends only on the initial polarization of the light, and the direction of the local magnetic field.

The optical density is now independent of ϕ:

$$OD_q(\omega, \rho) = 2 \int \bar{C}_q(\rho, z) \sum_{k'k} n_k(\rho, z) \sigma_{k'kq}(\omega, \vec{B}(\rho, z)) dz \tag{A.45}$$

The factor of 2 arises from the retroflection of the probe laser. There are now two integrals, one in ρ and one in z, remaining, as well as sums over states and polarizations. Unfortunately, because the cross-section (due to its narrow Lorentzian shape) is such a rapidly

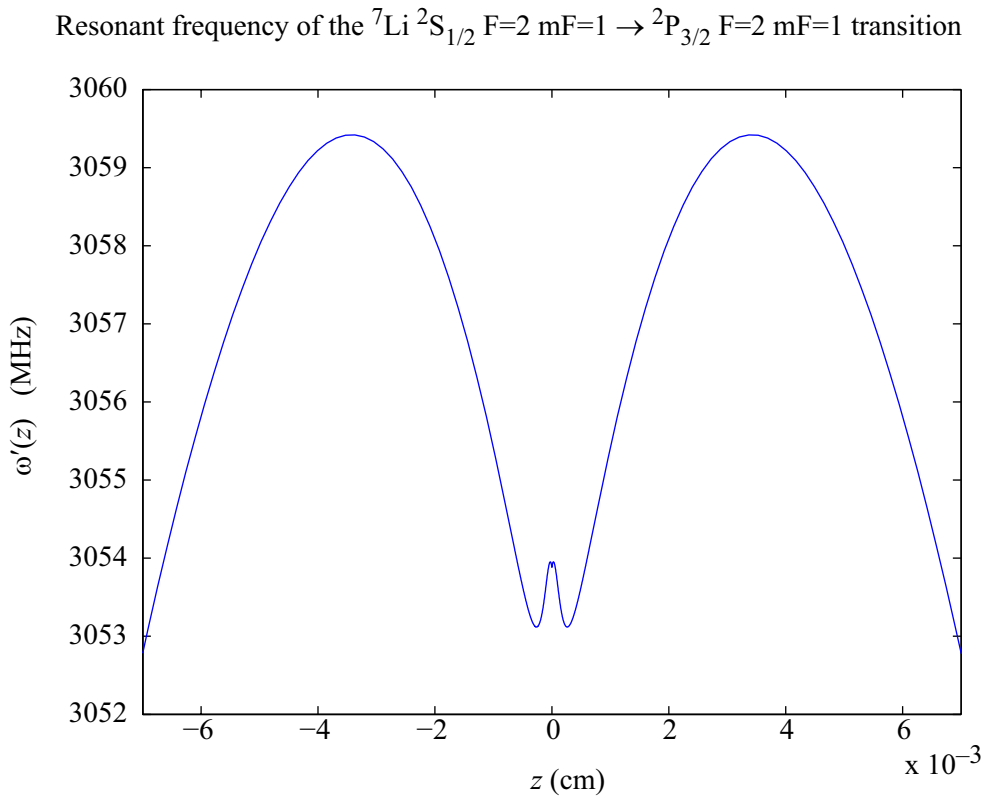

Figure A.1: Resonant frequency in an elliptical trap as a function of z for one transition in ^{7}Li, at $\rho = 0$. The states are indexed by their quantum numbers at zero field. The frequency shown is the detuning from the transition center of gravity frequency.

varying function of z, the step size for numerical integrations over z must be made very small to obtain accurate optical densities.

In his thesis [57], Weinstein shows how this integral in z, which must be performed with very small step sizes, may be removed from the problem. A summary of the procedure is given here, along with how we deal with potential pitfalls associated with using the procedure.

According to (A.26), the resonant frequency $\omega_{k'k}$ is a function of z. An example for a transition in ^{7}Li is shown in Fig. A.1. If the resonant frequency function is invertible, we can convert the integral in z in (A.45) to an integral over frequencies. In general, of

course, $\omega_{k'k}(z)$ is not invertible, such as in the lithium example shown. We can split the z domain of the function such that $\omega_{k'k}(z)$ is invertible over each subdomain of z.[2] Let d index each domain of z. For each domain d, we'll let $\omega'(z)$ represent the resonant frequency between states k' and k in that domain. Note that for every pair of states $k'k$ the set of domains will differ.

$$OD_q(\omega,\rho) = \frac{3\lambda^2}{\pi}\sum_{k'k}\sum_{d}\int \bar{C}_q(\rho,z(\omega'))n_k(\rho,z(\omega'))|\mathscr{A}_{k'kq}(\rho,z(\omega'))|^2$$

$$\times \frac{\Gamma^2/4}{(\omega-\omega')^2+\Gamma^2/4}\frac{dz}{d\omega'}(\omega')d\omega' \quad \text{(A.46)}$$

As of yet no computational simplification has been made — we still have an integral that requires very small step sizes for proper integration.

The simplification is made by realizing that, in the limit of small Γ, the Lorentzian in (A.46) becomes a δ-function. If Γ is very small, then the integrand is evaluated with $\omega' = \omega$:

$$OD_q(\omega,\rho) = \frac{3}{2}\lambda^2\Gamma\sum_{k'k}\sum_{d}\bar{C}_q(\rho,z(\omega))n_k(\rho,z(\omega))|\mathscr{A}_{k'kq}(\rho,z(\omega))|^2\left.\frac{dz}{d\omega_{k'k}}\right|_{\omega} \quad \text{(A.47)}$$

We pick up a factor of $\pi\Gamma/2$ in converting the Lorentzian to a δ-function. Note that the quantity $\Gamma\frac{dz}{d\omega_{k'k}}(\omega)$ has a very nice physical interpretation: it is the axial length, in each z domain, containing atoms that will absorb light of frequency ω.

This is a very convenient simplification. In order to use it, we must ask what we mean when we assume "Γ is very small". In the neighborhood of ω, the integrand $f(\omega')$ can be expanded in a Taylor series: $f(\omega') = \sum_p f_p(\omega'-\omega)^p$. Integrating $\int(\omega'-\omega)^p\frac{\Gamma/2}{(\omega-\omega')^2+\Gamma^2/4}d\omega'$ shows that the Lorentzian acts as a delta function for $p = 0, 1$, but

[2] In his thesis, Weinstein takes as domains the upper and lower halves of the trap (where there is a turning point in B). However, if $\omega_{k'k}(B)$ has a turning point for any field in the trap, the function must be split into additional domains.

becomes sensitive to values of the function off the Lorentzian peak for greater p.[3] Therefore we require that $f(\omega')$ is well approximated by a linear function in the neighborhood of ω (for a few natural linewidths on either side of ω). For most terms in (A.46), this is a good approximation; however, near the turning points of $\omega'(z)$, $dz/d\omega'$ rapidly becomes infinite. To deal with these points, we break up the integral near these turning points. We break the integral at the z points for which the resonant frequency is detuned by $\Gamma/2$ from the frequency ω_t at which a turning point occurs:

$$z_b = \begin{cases} z(\omega_t + \Gamma/2) & \text{Lower turning point at } \omega_t \\ z(\omega_t - \Gamma/2) & \text{Upper turning point at } \omega_t \end{cases} \tag{A.48}$$

In a given domain d, the integral in z ends at the turning point, z_t. The split integral is:

$$OD_q(\omega) = \frac{3\lambda^2}{\pi} \sum_{k'k} \sum_{d} \left[\int_{z \notin [z_b, z_t]} \bar{C}_q(z) n_k(z) |\mathscr{A}_{k'kq}(z)|^2 L(\omega, z, \Gamma) dz \right.$$

$$\left. + \int_{z \in [z_b, z_t]} \bar{C}_q(z) n_k(z) |\mathscr{A}_{k'kq}(z)|^2 L(\omega, z, \Gamma) dz \right] \tag{A.49}$$

$L(\omega, z, \Gamma)$ represents the Lorentzian of ω, resonant at $\omega'(z)$. The first term is dealt with identically to (A.46), with the exception that the δ-function integral is 0 for ω resonant with $z \in [z_b, z_t]$. We take this behavior into account by defining a function $\Delta(\omega, z, \Gamma)$ such that:

$$\Delta(\omega, z, \Gamma) = \begin{cases} 1 & \omega'(z) - \Gamma/2 < \omega < \omega'(z) + \Gamma/2 \\ 0 & \text{otherwise} \end{cases} \tag{A.50}$$

[3] For $p = 1$, the integration is performed for $p = 1 - \epsilon$, then evaluated in the limit $\epsilon \to 0$.

The first integral of (A.49) is just (A.47) multiplied by $1 - \Delta$:

$$\frac{\pi\Gamma}{2}\bar{C}_q(z(\omega))n_k(z(\omega))|\mathscr{A}_{k'kq}(z(\omega))|^2 \left.\frac{dz}{d\omega'_{k'k}}\right|_\omega (1 - \Delta(\omega, z_t, \Gamma)) .$$

The second integral of (A.49) is handled by realizing that the range $[z_b, z_t]$ is quite narrow. In this narrow range, we may approximate $\bar{C}_q(z)$ and $n_k(z)$ as constant functions. Additionally, $\omega'(z)$ (by definition of z_b) is approximately constant within this range. Approximating all these functions as constant turns the integral into a simple length. The result is:

$$\bar{C}_q(z_t)n_k(z_t)|\mathscr{A}_{k'kq}(z_t)|^2 L(\omega, z_t, \Gamma)|z_t - z_b|\Delta(\omega, z_t, \Gamma).$$

In order to combine the two terms, we will approximate $L(\omega, z_t, \Gamma)$ by a box function with the same average value: $L(\omega, z_t, \Gamma) \to \frac{\pi}{4}\Delta(\omega, z_t, \Gamma)$. After combining the terms, we have the total optical density:

$$\boxed{OD_q(\rho, \omega) = \frac{3}{2}\lambda^2 \sum_{k'k}\sum_d \bar{C}_q(\rho, \omega)\ n_k(\rho, \omega)\ |\mathscr{A}_{k'kq}(\rho, \omega)|^2\ l_d(\rho, \omega)} \tag{A.51}$$

where $l_d(\rho, \omega)$ is the local length occupied by atoms resonant with frequency ω:

$$l_d(\rho, \omega) = \begin{cases} 2|z_t - z_b| & \omega \in [\omega'(z_t) - \Gamma/2, \omega'(z_t) + \Gamma/2] \\ \Gamma \left.\frac{dz}{d\omega'_{k'k}}\right|_\omega & \text{otherwise} \end{cases} \tag{A.52}$$

Additionally, because the tails of the Lorentzian fall off only as $1/\omega^2$, we require that $f(\omega')$ not grow too large far from ω (for all ω' within the integration limits — note that these do not extend to infinity). Because $n_k(\omega')$ is essentially an exponential, it could grow very large at ω' far from ω. At some trap η, the integral of concern is[4]

$$\int_0^{\omega_{\max}} \exp(-\eta\omega'/\omega_{\max}) \frac{\pi\Gamma/2}{(\omega - \omega')^2 + \Gamma^2/4} d\omega'$$

[4]For a $q = 1$ or -1 transition.

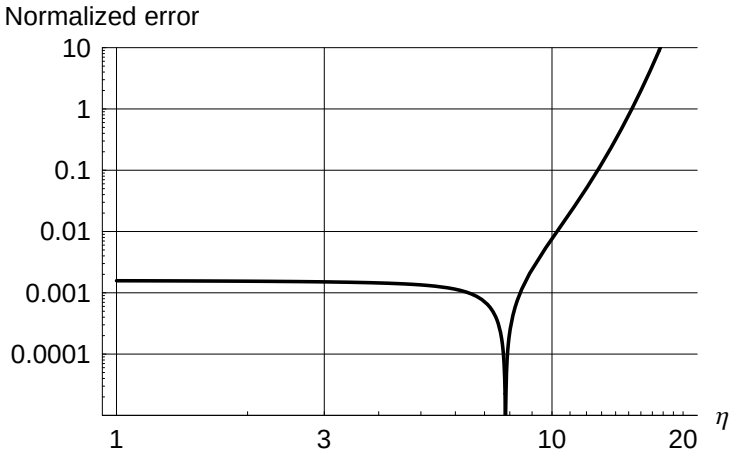

Figure A.2: The difference between the integral of $n_k(\omega')$ times a Lorentzian and the δ-function approximation $n_k(\omega)$. The result has been normalized to the δ-function approximation value. $\omega_{\max}$ was determined for a trap depth of 4 T; the natural linewidth used was 6 MHz. Note that the error becomes large at smaller η for larger linewidth.

The situation is worst when ω is close to $\omega_{\max}$. This integral was evaluated for a 4 T trap and 6 MHz linewidth, for various values of η. The error between this integration and the δ-function approximation is plotted versus η in fig. A.2. For these parameters, the normalized error becomes negligible for $\eta < 13$. The absolute error is $e^{-\eta}$ times the normalized error and is certainly negligible for all realistic η.

A.4 Code structure

In order to use a spectrum simulation with a least-squares routine efficiently, the run time of the model function must be made as short as possible. In our spectrum simulation code, the calculation is broken into four parts. The longest running portions of the simulation need only be run once or twice per fit, resulting in a simulation run time of between a few milliseconds to seconds, depending on the variables being fit. The simulation is calculated using MATLAB [106].

Runtimes of code subroutines are detailed below:

Code subroutine	Approximate runtime
Zeeman	10 s to 1 hr
Field	3 s
Optical interactions	1 s
Atomic distribution	5 ms

The Zeeman subroutine calculates the eigenenergies and quantum numbers of every energy level versus magnetic field in the ground and excited manifolds of the atom, as well as the transition probabilities between each state, as a function of magnetic field. This last calculation is necessary as the m_J quantum number of each state depends on magnetic field, especially if the atom exhibits hyperfine structure. For an atom such as cobalt, with 80 ground states and 96 excited states, this calculation can take upward of an hour over 1000 magnetic field points. Of course, this calculation is needed only once per atom.

The field subroutine determines the field at every r and z point in the probe beam, and is repeated whenever the beam position or size changes.

The optical subroutine performs the calculation described in §A.5 of Weinstein's thesis[57]. Note that in [57], the axial position of atoms resonant at a frequency ω is assumed to vary slowly with frequency. In practice this assumption is violated in the neighborhood of avoided level crossings, or for some $\Delta m_J = 0$ transitions, where line frequency is a constant versus magnetic field. The solution to this problem is described in §A.2 and §A.2.2. The output of this portion of the code is a matrix of optical transmission vs. spatial coordinates for each atomic line and vs. frequency. This section must be recalculated whenever any beam parameter (including polarization direction) is changed.

The atomic distribution subroutine merely multiplies the matrix returned by the optical section by the trap distribution of atoms at a given temperature, then integrates to determine optical depth as a function of frequency. This section of the code must be repeated for every spectrum simulation.

Appendix B

Fast cryogenic valves

One of the experimental challenges we faced in developing an apparatus for buffer gas removal with 1 μ_B species was the development of a fast, large-aperture, low-force, cryogenic valve. Due to constraints of our cryostat, and fear of damaging our dilution refrigerator, we could not use the high-force valve employed by Michniak *et al.* in a previous buffer gas experiment. In addition, because we had no direct line-of-sight between the top of our cryostat and our valve seal, we would need to design an actuation system that could actuate around corners. The design parameters we chose for our valve are shown in Table B.1.

The valve design occurred in two major stages. The first was the design of the valve seal, and the second stage was the design of the actuation system. Before describing our valve as we designed it, it is worth giving some background theory on valve seals.

B.1 Seal theory

An equation to describe the performance of seals (not restricted to only valve seals) is given by Roth [72]. Discarding the prefactors, the conductance is:

$$C_{\text{seal}} \propto \bar{v}\,\frac{R_s}{w_s}\,d_s^2\,e^{-\alpha F/2\pi R w}.. \tag{B.1}$$

Valve design parameters		
Parameter	Constraint	Description
τ_{pump}	30 ms	Cell pumpout time constant.
C_{open}	12 L/s	Open valve conductance to achieve τ_{pump} for our cell.
C_{closed}	$< 10^{-4}$ L/s	Closed valve conductance.
F	< 20 lbf	Valve sealing force.
R_v	≥ 0.7 in	Valve aperture radius to obtain C_{open} (in the molecular regime).
L_{open}	1.3 in	Distance traveled by opening valve.
$Q_{\text{actuation}}$	< 100 mJ	Frictive heat released by actuation.
t_{open}	40 ms	Time taken to open valve.
materials	nonmagnetic	
moving parts	nonmetallic	Prevents eddy current heating when opening valve.

Table B.1: Cryogenic valve design parameters

Here R_s is the radius of the seal, w_s is the thickness of the seal, F is the sealing force, d_s is the diameter of scratches or leak channels on the surface of the seal, and α is a property of the sealing materials (which can depend on temperature).

Three different approaches to material selection can be taken to reduce the conductance in (B.1). One tack is to use hard surfaces that can be highly polished, to minimize d_s. Materials to use would be transition metals or ceramics. Another approach is to use soft materials, to maximize α. Here one would use polymers or poor metals such as indium. These materials are typically difficult to polish well, and are easily scratched. One can also combine these two approaches, composing one sealing surface of a hard material and the other of a soft material. If the seal environment can be contaminated by particles, at least one soft material is typically required. Use of a soft material will allow the contaminant to become embedded in the soft surface. Otherwise this contaminant will prevent the valve from sealing, dramatically increasing d_s. These approaches to material selection are summarized in Fig. B.1. The "hard-soft" approach is the one most commonly found in commercial valve designs: The valve can be used in dirty environments, is somewhat

"Hard-hard": Engine cylinder valves

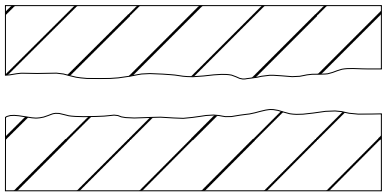

Sealing surfaces are flat, highly polished hard surfaces, e.g. metals, ceramics

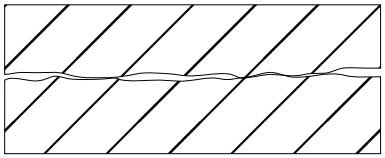

No deformation when closed; good surface flatness / polish necessary.

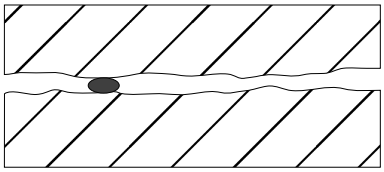

Hard grit keeps valve from sealing.

Good in extreme temperature, clean environments.

"Hard-soft": Plumbing valves

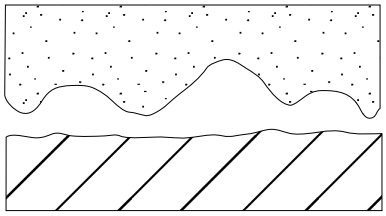

One surface is flat, highly polished hard surface, other is less tolerant soft elastomeric surface.

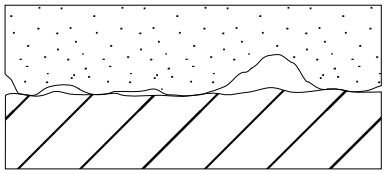

Elastomer conforms to hard surface on short length scales.

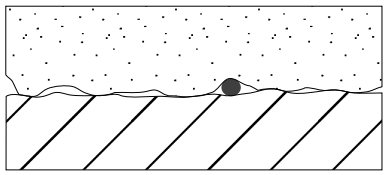

Small grit is embedded in elastomer surface.

Good in normal temperature, dirty environments

"Soft-soft": Pinch valves, biological valves

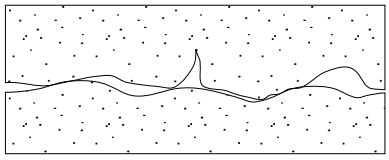

Two elastomeric surfaces. Twice as sensitive to scratches, long-range defects.

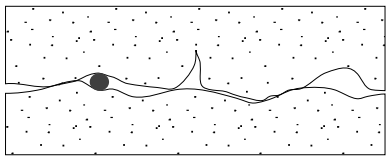

Both elastomers conform to grit.

Surfaces become damaged over time

Figure B.1: Varieties of valve seals.

less susceptible to damage than the "soft-soft" design, and the hard surface can be easily integrated into the body of the valve.

(B.1) gives two geometric regimes of low seal conductance. In the limit of large seal area, the path traveled by gas leaking through the seal is long. In this "large area" regime, the conductance is inversely proportional to the seal width. At very low seal width, the pressure on the seal at a given force grows very large, and the materials composing the seal conform to each other, eliminating leak paths. This "knife edge" limit can produce very small leaks; however, the seal can typically only be made once, as the materials will typically be damaged by the high sealing pressure. Note that although the transition w_s from the knife-edge to the large-area regime depends on F, larger F always leads to exponentially smaller leak rates at any w_s.

The shape of the seal can also affect the quality of the valve seal. If the two sealing surfaces are flat planes, the two surfaces must be compressed exactly normal to each other. If they are compressed at an angle, the closing force is concentrated at one side of the seal, leading to a macroscopic gap in extreme cases. If one surface is spherical and the other is conical or a rounded corner, the seal becomes insensitive to such angular misalignment. However, the seal is now sensitive to translational misalignment of the sealing faces. In addition, the spherical and corner/conical faces must be round to a very high degree (on the order of d_s). We have found that two very flat surfaces are much easier to achieve than two very round surfaces, in a typical machine shop. We have devised a mechanism to remove the problem of angular misalignment, which is described in the next section.

B.2 Seal design

Because the charcoal sorb in our cell can shed small motes of charcoal dust, we chose the "hard-soft" seal construction. At 100 mK, the softest materials are the fluoropolymers. In tests of our seal, we found that they all performed similarly well, with polytetrafluoroethylene (a.k.a. PTFE or Teflon) sealing marginally better than other varieties.[1] Because of the issues of dust and repeatable sealing, we chose a large sealing area. Because it is far easier to produce flat surfaces in the on-site machine shops, we use a flat-on-flat design. The outer diameter of the seal is chosen as large as possible, limited by clearance to the cell sorb.

The lower portion of the valve seal is static and includes the valve aperature; we call this the "valve seat". It is made from 99.9% alumina, green machined in ring form then fired. We polish the alumina seat using diamond polish on a lapping machine. The seat is lapped successively using 45 micron, 6 micron, and 0.5 micron suspensions. The polishing is limited by the grain structure of the alumina, and contains visible pitting, with pits on the order of a hundred microns.

The upper, moving portion of the valve seal we call the "valve boot". It is made from a 0.35 in thick cylindrical PTFE disk. To polish the boot, we first remove a few mil from the sealing face of the boot, using a lathe. The boot is then wet-sanded on a granite table using 600, 1200, and 1500 grit silicon carbide paper, progressively. After each paper is used, the face is inspected for scratches — if any are discovered the sanding process is repeated. The boot is then mounted on a lathe and the lathe is set to rotate at $\sim$ 2000 rpm. The 1500 grit paper is applied to the face for a couple passes. At this point the boot face should dully reflect overhead lights, and only fine circumferal scratches should be

[1] Specifically fluorinated ethylene-propylene (FEP), chlorotrifluoroethylene (Kel-F), and ethylene-tetrafluoroethylene (ETFE).

observable on the boot face. The face is finally polished on the lathe using Novus Heavy Scratch Remover plastic polish applied with a Texas Feathers microfiber polishing cloth. This polish is reapplied as needed for 5 minutes or so. The boot face should now reflect overhead lights optically, the fine circumferal scratches should be well-smoothed.

In order to deal with shaft misalignment preventing proper valve alignment, we include a shaft "alignment decoupler". The valve boot is attached to a short valve shaft. A ball is affixed to the top of this shaft. To close the valve, a piston pushes on this ball. Even if the piston does not close normally to the valve seat face, the ball ensures that the valve boot closes normally to the valve seat. In order to open the valve, the ball is trapped within a lower plate attached to the piston. When the piston retracts, it pulls this plate, opening the valve. The lower shaft runs loosely through a bushing (clearance 4 mil), ensuring that the valve boot does not stray off the valve seat.

The piston is attached to an upper shaft. This upper shaft runs through an upper bushing, that ensures the piston actuates normally to the valve seat face. To minimize friction and thermal conduction, both the upper and lower shafts are made from 40% graphite-filled Vespel polyimide (Vespel SP-22). The valve seat, boot, shafts, and alignment decoupler are depicted in Fig. B.2.

The valve as designed has a valve closed conductance of $< 10^{-5}$ L/s at 4 K, when closed with 20 lbf of force. Assuming the material properties are unaffected by further reductions in temperature, this conductance will decrease as $\sqrt{T}$ with decreasing temperature (due to reduced thermal velocity).

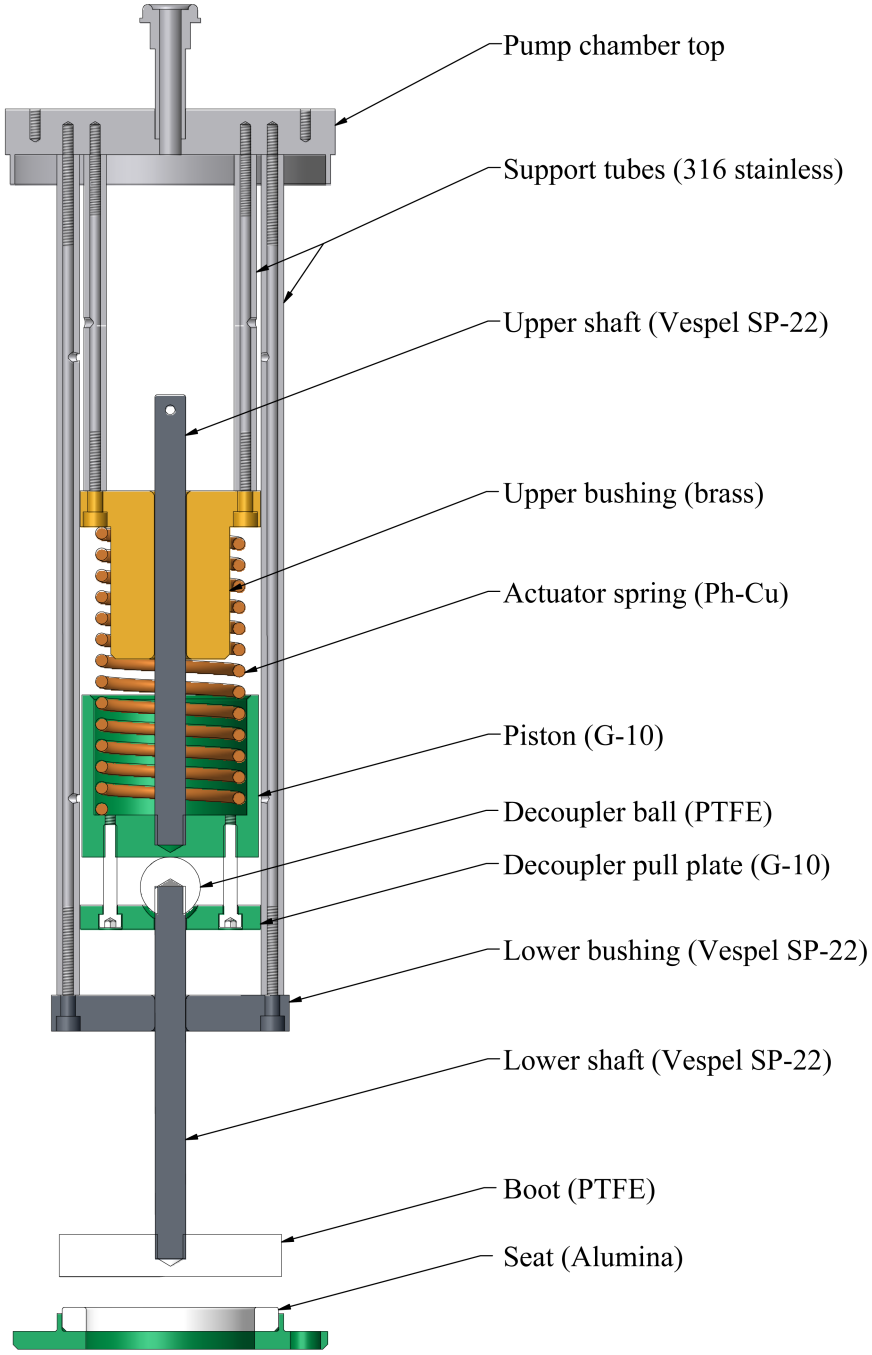

Figure B.2: The lower valve apparatus, including all valve apparatus within the cell. The cell walls are not shown.

B.3 Actuation design

The valve actuator uses a "string-and-spring" design paradigm. A spring near the valve seal provides the valve closing force. In our design the spring pushes against the piston (described in the previous section) from the upper shaft bushing. We desired a nonmagnetic spring, hence our spring is made from phosphor bronze. 316 stainless steel was not used, as the nonmagnetic austenitic phase can evolve into the magnetic martensitic phase with multiple spring compressions. The spring, manufactured by Southern Spring [107], has a spring constant of 13.7 lbf/in, a valve closed force of 20 lbf and a valve open force of 39 lbf. Given the mass of the valve shaft and boot, opening the valve in 30 ms requires an opening force just greater than 39 lbf. The ends of the spring are ground flat so that the spring pushes as evenly as possible on the piston.

The "string" in our design is a 3/64 in 316 stainless steel wire rope with 7x7 strand construction. This rope has a breaking strength of 270 lbf. The rope is attached to the upper valve shaft using an oval compression clip. The rope resides within a tube; this tube doubles as the pumping line for the cell pumping chamber. Because there is no line-of-sight between the pumping chamber and the top of the cryostat, this tube contains numerous bends. Originally the wire rope merely ran through a bent stainless steel tube. However, high friction between the rope and these bends caused the rope to stick in the tube, caused damage to the tube, and would have caused excessive heating in the valve actuation.

We therefore replaced the bends in the pull tube with pulleys. The pulleys were constructed using Barden SR6SSTB5 cryogenic non-lubricated ball bearings [108]. The pulley shaft and sheaves are constructed from 316 stainless steel to relatively high tolerances; the exact requirements are described in engineering literature supplied by Barden. The pulleys are contained within a "pulley box". The shafts of the pulleys are press fit into the

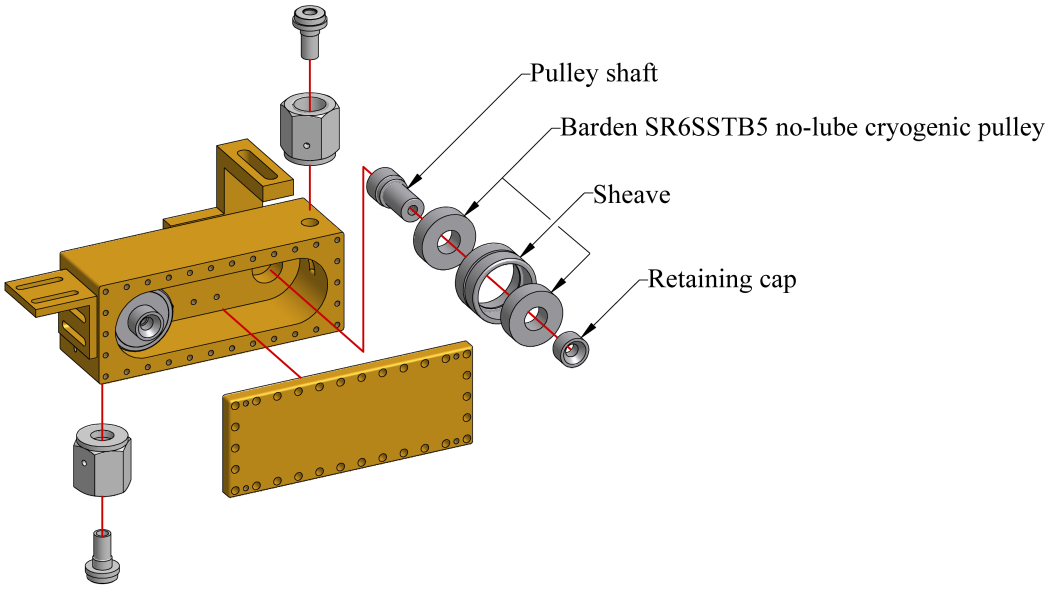

Figure B.3: The lower pulley box.

body of the box. Each pulley is made with two bearings and one sheave as depicted in Fig. B.3. The pulley is held together with a retaining cap attached with a flat-head screw; this cap is captured in a counterbore in the lid of the pulley box. This counterbore prevents the pulley shaft from torquing out of the pulley box. The sheave has a groove, slightly larger and as deep as the diameter of the wire rope; the wire rope runs in this groove. The clearance between the pulley and the pulley box body is significantly less than the diameter of the wire rope, preventing the rope from slipping off the sheave. The wire rope enters and leaves the pulley box through VCR glands aligned with the sheave groove and brazed into the pulley box. The wire rope is fed through the pulleys and the pulley box lid is attached with an indium seal.

The path traced by the valve pull line is shown in Fig. B.4. After passing through the lower pulley box, the wire rope travels up the side of the fridge to a feedthrough in the IVC top. The pull line between the pulley box and the IVC top is not rigid; instead the

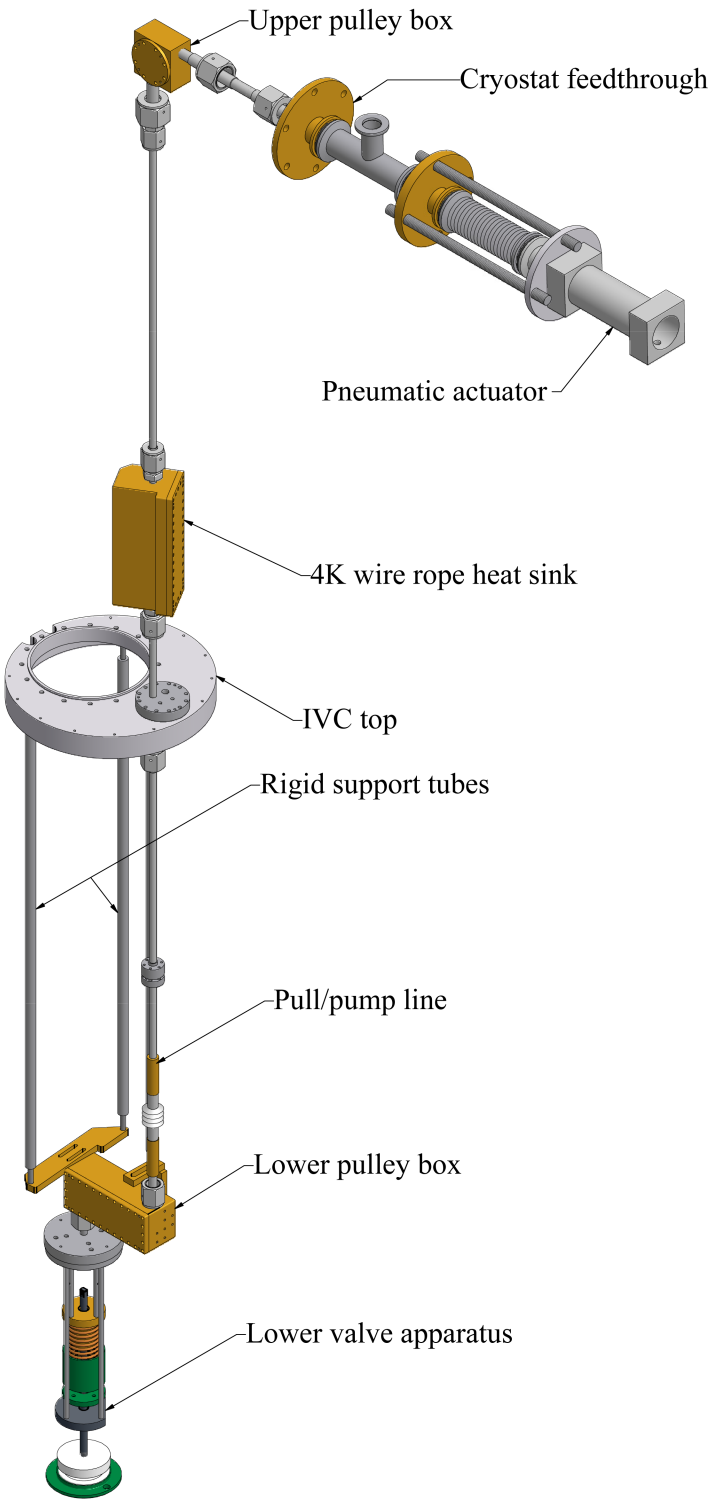

Figure B.4: Elements of the valve apparatus. Non-essential components including the cryostat walls, IVC walls, and cell walls have been removed. The third rigid support tube is hidden behind the pull line.

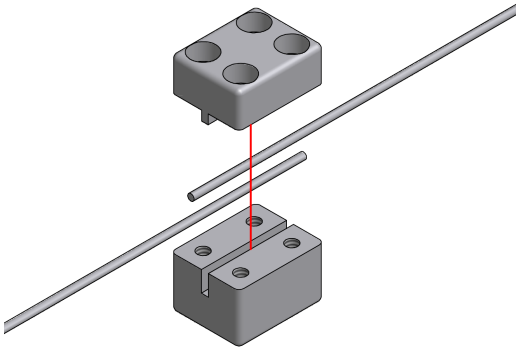

Figure B.5: Wire rope joining clip.

rigidity is provided by three support tubes to which the pulley box is attached. This system allows the cell to be positioned and aligned within the IVC extension, without attention to the length of the pull tube. The pull tube contains a hydroformed bellows to make up for adjustments in length and small translations. In order to protect the bellows from torquing when VCR joints are made, an indium seal with a rotating clamp is included between the bellows and the IVC feedthrough.

Above the IVC feedthrough the wire rope runs through a heat sink box, sealed like the pulley boxes with an indium seal. The wire rope is made of a lower and upper rope; these are joined using a homemade reusable wire-rope clip, shown in Fig. B.5. This wire-rope clip both allows the two ropes to be repeatably joined without damage to the ropes, unlike a typical Crosby clip, but also provides approximately three times the pull-out strength of a Crosby clip. The clip is attached to the interior of the heat sink box using a flexible copper rope. The box is in turn heat sunk to the top of our aluminum IVC with another copper rope.

After the heat sink box, the pull line travels to the top of the cryostat, makes a 90° bend in another pulley box, then exits the cryostat. A tee is inserted in the line for

pumping of the cell. The rope is attached to the end of our pneumatic actuator. Vacuum is preserved by attaching the end of this actuator to the pull tube with an edge-welded bellows.

Appendix C

Spin-rotation spin relaxation theory

This appendix describes the theory we use to predict spin relaxation between hydrogenlike atoms and noble gases. We consider two effects: the spin-rotation interaction and the contact hyperfine interaction.

Atoms in magnetic traps are trapped in metastable low-field seeking m_J levels. Any mechanism that changes the projection of $\vec{\mathbf{J}}$ on the magnetic field will therefore cause loss of the trapped atoms. For instance, if atoms move through a magnetic field zero, the projection axis is lost. This type of trap loss is described by Weinstein in his thesis [57].

We must also consider atomic collisions that change m_J. In S state atoms, the total electronic angular momentum is just the electronic spin. In the special case of S state atoms we call Zeeman state changing collisions spin-relaxing collisions. Because the electronic spin couples so weakly to the colliding atom, these spin-relaxing collisions will in general be rare. These collisions were originally studied in the context of optical pumping experiments of the alkali atoms [109].

These spin-relaxing collisions can be between the atoms themselves, or between the atoms and some atom of another species occupying the cell. In buffer gas experiments, this other atom will be the buffer gas, typically ^{3}He or ^{4}He. If the buffer gas density is high, atom-buffer gas relaxation will occur much more frequently than atom-atom relaxation, and we may consider only the atom-buffer gas mechanism. Because the noble gases are frequently used in optical pumping experiments (to increase the diffusion time of the atoms, and more recently to use spin relaxation to polarize the noble gases themselves), a great deal of theory has been performed to predict spin relaxation rates between alkalis and the noble gases. Because we are interested in 1 μ_B S state atoms, we can lift a large portion of the alkali-noble gas optical pumping relaxation theory to help predict the buffer gas induced spin relaxation of our trapped atoms. The important difference with which we must deal is the greatly different energy ranges of the experiments. Optical pumping experiments are typically conducted near room temperature, where the motion of the noble gas atoms may be regarded semiclassically. At the temperature of buffer gas trapping experiments, the motion is quantum mechanical, ranging over the first few partial waves. In this writeup I will give an overview of the existing applicable spin relaxation theory and describe how it is adapted to treat the quantum mechanical motion of the He atom.

The dominant relaxation mechanism in alkali-buffer gas optical pumping systems is due to coupling of the electronic spin with the rotation of the buffer gas atom about the atom nucleus. The theory was first investigated thoroughly by Herman [96] and more recently a very pedagogical examination of the problem was given for He buffer gas by Walker, Happer, and Thywissen [3]. The treatment in this last paper provides a simple formula by which even the experimentalist may determine the strength of the spin-rotation interaction.

We are looking for an interaction that couples the electronic spin anisotropically

to a variable in the He atom. In spin-rotation, this is accomplished in a three step process. First, the He atom distorts the ground state wavefunction of the electron. Because of this distortion the electron is no longer in a pure S state. If there is any $\vec{\mathbf{L}} \cdot \vec{\mathbf{S}}$ spin-orbit interaction in this distorted state, the spin will precess. However, at this stage we have not added any anisotropy; as the He atom moves away the mixing will be undone and no net rotation of $\vec{\mathbf{S}}$ will have occurred. The anisotropy emanates from the rotation of the He atom about the atom nucleus. Because of this rotation, the axis of distortion is rotated anisotropically in space as the He atom rotates about the atom nucleus. As $\vec{\mathbf{S}}$ follows the rotating $\vec{\mathbf{L}}$, a net rotation of $\vec{\mathbf{S}}$ in space occurs. An equivalent description, and one more useful for mathematical analysis, is that a Coriolis force is applied to the electron (in the rotating frame), this force couples $\vec{\mathbf{S}}$ to the He rotation.

C.1 The Spin-Rotation interaction

We will calculate the strength of the spin-rotation interaction by calculating the strength of each effect in this three-step process: considering the He-induced wavefunction distortion, then the Coriolis interaction, and finally the $\vec{\mathbf{L}} \cdot \vec{\mathbf{S}}$ interaction. This method is taken directly from the paper of Walker, Thywissen, and Happer [3]. Barring the description of how we calculate the distorted electron wavefunctions, this section is a paraphrase of that paper.

Because the strengths of these three effects are all small, we may calculate the spin-rotation interaction perturbatively. We choose as our reference frame that centered on the atom nucleus, and rotating with frequency

$$\vec{\omega}_N = \frac{\hbar \vec{\mathbf{N}}}{MR^2}. \tag{C.1}$$

Here $\vec{\mathbf{N}}$ is the nuclear rotation, with $\mathbf{N^2} = \hbar^2 N(N+1)$, M is the reduced mass of the

colliding system, and R is the internuclear separation. Note that we shall assume that R is a parameter, not an operator. This is true in the adiabatic limit; that is, the spin-rotation interaction can not affect R on a time scale short enough to "feed back" on the calculated spin-rotation effect. In exothermic collisions (i.e., from low-field seeker to high-field seeker), we can consider this to be true, as the exiting He atom simply does not contribute to further spin relaxation.

C.1.1 Wavefunction distortion

Within this reference frame we shall set z to lie along the internuclear axis. In this frame, the electron feels a potential that is the the free atomic potential, plus the potential from the He atom, with the helium atom located at $\vec{R} = R\hat{z}$. The electron feels the standard screened $1/r$ potential from the atomic nucleus. Because the He atom is neutral and deeply bound, the electron experiences only a weak polarization interaction from the He atom unless it is actually within the He core. The potential from the helium atom has the following $\vec{r}$ dependence:

$$V_{\mathrm{He}}(\vec{r},\vec{R}) = -\frac{\alpha}{\left|\vec{r}-\vec{R}\right|^4} - \frac{\beta}{\left|\vec{r}-\vec{R}\right|} e^{-|\vec{r}-\vec{R}|/\zeta}. \tag{C.2}$$

Here α and β are arbitrary constants representing the strength of each term. The $1/r^4$ term arises from the electron polarizing the He atom, and the screened term is the core interaction. The total potential is shown in Fig. C.1.

It has been shown [99, 110] that, for low scattering energies, the potential in (C.2) perturbs the electron to first order as a δ-function potential, and may be replaced by

$$V_{\mathrm{He}}(\vec{r},\vec{R}) = -\frac{2\pi\hbar^2 a_s}{m}\delta^3\left(\vec{r}-\vec{R}\right), \tag{C.3}$$

where a_s is the s-wave scattering length and m is the electron mass. This is known as the Fermi potential.

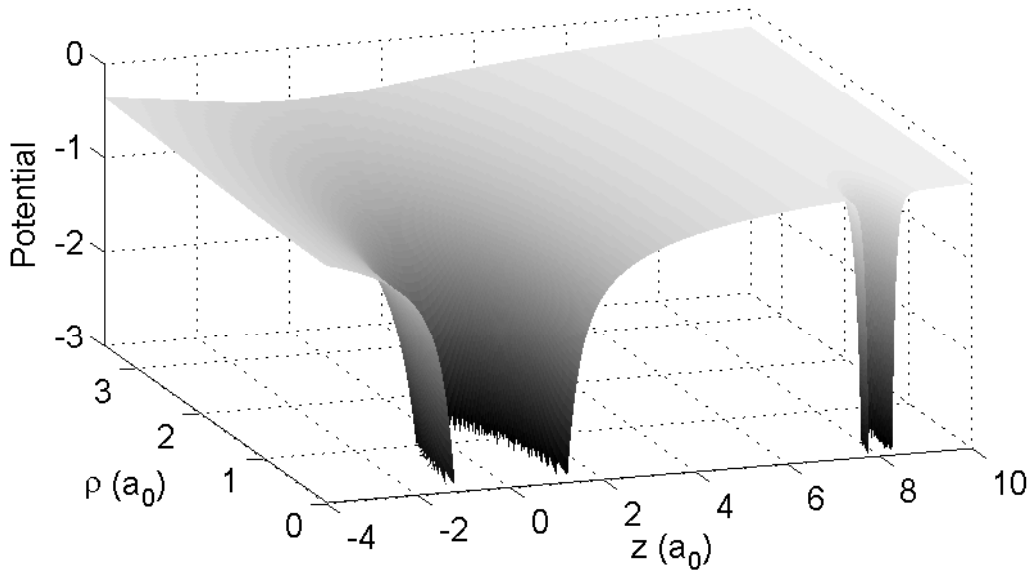

Figure C.1: Potential experienced by the s state valence electron. The atom nucleus is at $(z, \rho) = (0, 0)$, the He atom is at $(z, \rho) = (8, 0)$. The potential strengths are arbitrary.

Armed with this simple potential, we can easily calculate the electron wavefunction distortion. The unperturbed wavefunction is just the ground state atomic wavefunction. The Fermi potential will mix in wavefunctions from other atomic states, where the electronic wavefunction for a state with quantum numbers n, l, and m is

$$\psi_{nlm} = R_{nl}(r)Y_l^m(\theta,\phi). \tag{C.4}$$

Here $R_{nl}(r)$ is the radial part of the wavefunction and $Y_l^{m_l}(\theta,\phi)$ is the spherical harmonic for state l, m. Using first order perturbation theory [51], the distorted wavefunction is

$$\psi_1(\vec{r},\vec{R}) = \psi_0(\vec{r}) + \sum_{nlm_l} c_{nlm}(\vec{R})\psi_{nlm}(\vec{r}), \tag{C.5}$$

$$c_{nlm}(\vec{R}) = -\frac{\langle\psi_0|V_{\rm He}(\vec{R})|\psi_{nlm}\rangle}{E_{nlm}}. \tag{C.6}$$

Taking the matrix element of the δ-function in the He potential just evaluates the wavefunction at the He position, and the c_{nlm} reduce to

$$c_{nlm}(\vec{R}) = \frac{2\pi\hbar^2 a_s}{mE_{nlm}}\phi_0(R\hat{z})R_{nl}(R)Y_l^m(0,0). \tag{C.7}$$

$\phi_0(\vec{r})$ is the ground state s wave-function. Because we have defined the z axis along the internuclear axis, $\theta = 0$. Note that $Y_l^{m_l}(0,\phi)$ is nonzero only if $m_l = 0$. Because of this, the He atom will only mix in electronic states with $m_l = 0$.

We can take $\phi_0(R)$ from calculated Hartree-Fock radial wavefunctions [111]. For excited states, we can calculate $R_{nl}(r)$ from Coulomb approximation wavefunctions [112]. We assume that outside some radius r_0, similar to the size of the atomic core, the potential seen by the unperturbed electron is merely a $-2/r$ Coulomb potential. Outside of r_0, then, the wavefunction can be found by solving the radial Schrödinger equation using the Coulomb potential and the known energy of the atomic level:

$$\frac{d^2R}{dr^2} + 2\frac{dR}{dr} - \left(\frac{l(l+1)}{r^2} + V(r) - E\right)R = 0, \tag{C.8}$$

where r is in a_0 and $V(r)$ and E are in Rydbergs. Since R is generally large compared to the size of the atomic core, we will only need to know the wavefunction for $r > r_0$. The wavefunction is now determined up to a normalization constant. To determine the normalization constant we manufacture a wavefunction for $r < r_0$, and use it to normalize the entire wavefunction. An ersatz potential V_a is used to calculate this wavefunction for $r < r_0$. Let R_b be the unnormalized wavefunction for $r > r_0$ and R_a be the unnormalized solution for $r < r_0$. R_a is scaled such that

$$R_a(r_0) = R_b(r_0) \tag{C.9}$$

and r_0 is adjusted such that

$$\left.\frac{dR_a}{dr}\right|_{r_0} = \left.\frac{dR_b}{dr}\right|_{r_0}. \tag{C.10}$$

The normalization constant N_R satisfies:

$$1 = \int_0^{r_0} |rN_R R_a|^2 \, dr + \int_{r_0}^{\infty} |rN_R R_b|^2 \, dr, \tag{C.11}$$

and N_R can be easily determined by solving this equation. Note that the Y_l^m are assumed to be properly normalized already.

N_R does not depend strongly on the V_a used. I used a couple different box potentials, as well as various screened Coulomb potentials. All gave the same normalization constant. For the screened Coulomb potentials, I chose

$$V_a(r) = -\frac{2Z}{r} e^{-r/\zeta} \tag{C.12}$$

with Z the nuclear charge, and ζ chosen such that V_a was continuous with the Coulomb potential at r_0. Depending on the r_0 chosen, a certain number of additional nodes are added to the basic Coulomb wavefunction. To obtain the N used for the theory here, I chose r_0 such that the total number of nodes in the wavefunction was $n - l - 1$. This is the number of nodes in a hydrogen wavefunction with quantum numbers n and l.

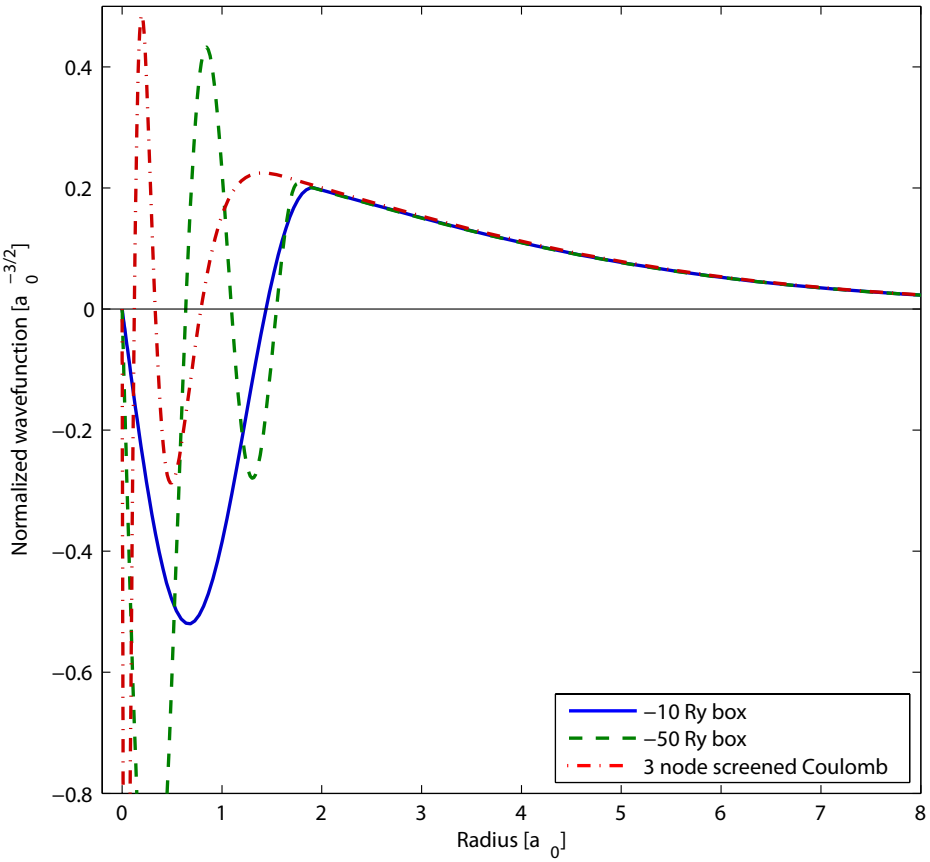

Figure C.2: Comparison of Coulomb approximation wavefunction normalizations for $5p$ Ag ($E_{5p} = -\mathrm{Ry}/1.883^2$). Shown are solutions for three different V_a. The first two are box potentials of different depths, the last is a screened Coulomb, with r_0 chosen to give a wavefunction with 3 nodes. The r_0 used are, respectively, 1.938, 1.770, and 1.755 a_0. Note that while the choice of V_a affects the wavefunction strongly for $r < r_0$, it has almost no affect on $R(r > r_0)$.

C.1.2 Coriolis interaction

The remaining perturbative terms in the spin-rotation interaction are the spin-orbit and Coriolis interactions. They may be dealt with in any order; mathematically it is simpler to deal with the Coriolis interaction first. The effective potential from the Coriolis interaction is [3]

$$V_C = -\hbar\vec{\omega_N}\cdot\vec{\mathbf{L}}. \tag{C.13}$$

Note that this Coriolis interaction will interact only with the $l \neq 0$ components of ψ_1. Applying perturbation theory once more yields an anisotropic component to the electron wavefunction:

$$\psi_2(\vec{r},\vec{R}) = \psi_1(\vec{r},\vec{R}) - \sum_{nl}\frac{\hbar^2 c_{nl0}(R)}{ME_{nl}R^2}\vec{\mathbf{N}}\cdot\vec{\mathbf{L}}. \tag{C.14}$$

C.1.3 Spin-orbit interaction

The probability of flipping the spin will be given by the energy difference between the projections of $\vec{\mathbf{S}}$ on $\vec{\mathbf{N}}$. The energy shift is given perturbatively by

$$\big\langle\psi_2\big|\xi(\vec{r})\vec{\mathbf{L}}\cdot\vec{\mathbf{S}}\big|\psi_2\big\rangle. \tag{C.15}$$

Here $\xi(\vec{r})$ is the fine-structure interaction at location $\vec{r}$. Note that $\langle\psi_{nl}|\xi(\vec{r})|\psi_{nl}\rangle$ is just the fine structure constant f_{nl}. The leading order term of the energy shift connects the waveform deformation of (C.5) with the Coriolis perturbation of (C.14). It is rather messy, but written out the energy shift is:

$$\sum_{nln'l'}\left\langle\frac{\hbar^2 c_{n'l'0}(R)}{ME_{n'l'}R^2}\vec{\mathbf{N}}\cdot\vec{\mathbf{L}}\psi_{n'l'0}\middle|\xi(\vec{r})\vec{\mathbf{L}}\cdot\vec{\mathbf{S}}\middle|c_{nl0}(R)\psi_{nl0}\right\rangle. \tag{C.16}$$

In Walker's paper [3], angular momentum vector identities are exploited to show that this results in a $\vec{\mathbf{S}}\cdot\vec{\mathbf{N}}$ interaction, with $n' = n$, considering only the $l = l' = 1$ case. The result can be shown for higher l by expanding all the momenta into their z, $+$, and $-$ components,

and using the fact that N is perpendicular to $\hat{z}$ and $m_l = 0$. Doing this yields an effective Hamiltonian term of

$$\boxed{H_{\text{eff}} = \gamma_a(R)\vec{\mathbf{S}}\cdot\vec{\mathbf{N}}}, \tag{C.17}$$

with

$$\boxed{\gamma_a(R) = \frac{8\pi^2\hbar^6 a_s^2}{Mm^2R^2}\phi_0^2(R)\sum_{nl}\frac{f_{nl}}{E_{nl}^3}R_{nl}^2(R)Y_{l0}^2(0,0)}. \tag{C.18}$$

This formula was used to calculate $\gamma_a(R)$ for colliding Ag-He. ϕ_0 was taken from tabulated Hartree-Fock wavefunction [111], and the ψ_{nl0} were calculated using the Coulomb approximation method described above. The excited state Ag energies were taken from [37]. The result is shown in Fig. C.3.

C.2 Semiclassical calculation

C.2.1 Spin-relaxation probability

We now must use this spin-relaxation interaction to calculate the probability of having a spin flip. In [3] this is done for high temperatures, by treating the He atom as a classical scatterer. R and N are taken as classical parameters. $R(t)$ is calculated from the radial molecular potential. N is obtained by identifying it with the classical orbital momentum, obtained from the collision energy E and the impact parameter b:

$$N = \sqrt{\frac{2MEb^2}{\hbar^2}}. \tag{C.19}$$

$R(t)$ can be obtained from the classical central force Hamiltonian:

$$E = \frac{M\dot{R}^2}{2} + \frac{\hbar^2N^2}{2MR^2} + V_{\text{mol}}(R). \tag{C.20}$$

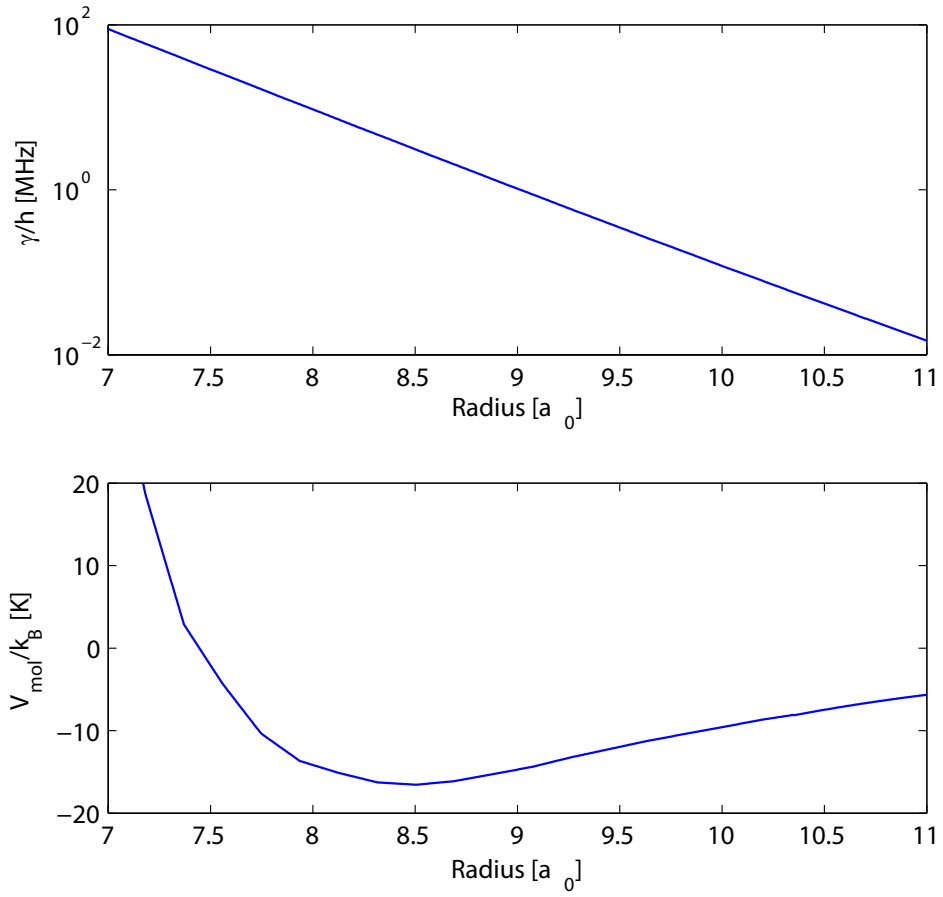

Figure C.3: The top plot shows the spin-rotation interaction energy $\gamma_a(R)$ for Ag-^{3}He, versus internuclear separation. See §C.1.3 for the sources of the wavefunctions used to calculate γ_a. The lower plot shows the internuclear Ag-He interaction energy, taken from [98]. At the allowed radii for the He atom, γ_R is an exponentially decreasing function of R. This is because the ground and excited state Ag wavefunctions are both exponentially decreasing in this range.

V_{mol} is the interaction energy between the atom of interest and the He atom in the ground electronic state of the XHe molecule (where X represents the atom of interest). The V_{mol} I used for colliding Ag-He is shown in Fig. C.3.

The probability of a spin flip can be found by tracking the evolution of the electronic wavefunction. We'll now set the reference frame such that the z-axis is along the local magnetic field. If the probability of a spin flip is small, the electronic wavefunction can be written

$$|\psi\rangle = |\phi_0(\vec{r})\rangle \Big(|\uparrow\rangle + \alpha(t) |\downarrow\rangle \Big), \tag{C.21}$$

where $\alpha(t)$ represents the probability amplitude to have undergone a spin flip by time t, and $|\uparrow\rangle$ and $|\downarrow\rangle$ are the (low-field seeking) spin up and (high-field seeking) spin down states, respectively. α is assumed to be small for all time. The probability of a spin flip is found by solving the time dependent Schrödinger equation,

$$i\hbar \frac{d}{dt} |\psi\rangle = H_0 |\psi\rangle + \frac{1}{2}\gamma(R) \left(2S_z N_z + S_+ N_- + S_- N_+\right) |\psi\rangle . \tag{C.22}$$

The time derivative of $|\phi_0\rangle |\uparrow\rangle$ cancels with $H_0 |\phi_0\rangle |\uparrow\rangle$, and likewise for the time derivative of $|\phi_0\rangle |\downarrow\rangle$. The only remaining component is the time derivative of α:

$$i\hbar |\phi_0\rangle \left(\frac{d\alpha(t)}{dt} |\downarrow\rangle \right) = \frac{1}{2}\gamma(R) |\phi_0\rangle \Big[(N_z + \alpha(t) N_-) |\uparrow\rangle + (-\alpha(t) N_z + N_+) |\downarrow\rangle \Big] \tag{C.23}$$

Because $\alpha(t)$ is small, we will ignore all terms on the right side where it appears. By collapsing the equation with $\langle\phi_0| \langle\downarrow|$, we obtain an integral equation for the spin flip probability amplitude:

$$\alpha(\infty) = -\frac{i\langle N_+\rangle}{2\hbar} \int_{-\infty}^{\infty} \gamma(R(t)) dt \tag{C.24}$$

Note that because $\vec{\mathbf{N}}$ is an external parameter, $\langle N_+\rangle$ has a nonzero expectation value for certain collisions. We may convert the time integral in (C.24) to a more manageable integral in R. To do this we change variables within the integral from t to R; $\dot{R}$ is obtained from

(C.20). The resulting integral over R is:

$$\alpha(\infty) = -\frac{i\langle N_+\rangle}{\hbar}\sqrt{\frac{M}{2E}}\int_{R_0}^{\infty}\frac{\gamma(R)}{\sqrt{1-b^2/R^2-V_{\rm mol}(R)/E}}dR. \tag{C.25}$$

Here R_0 is the minimum radial separation between the atomic and He nuclei. It can be calculated by solving (C.20) with $\dot{R} = 0$. Note that if E is less than the height of the centrifugal barrier, the He atom will never penetrate classically within the centrifugal barrier. We therefore expect this semiclassical method to underestimate the amount of spin relaxation, with the degree of error increasing in the cold regime.

C.2.2 Relaxation cross-section

To find the cross-section, we merely find the spin flip probability (the square norm of the probability amplitude), and integrate over all possible values of N. This is equivalent to integrating over all possible impact parameters b. Note that the phase space density of impact parameters goes as $2\pi b$. $|\langle N_+\rangle|^2$ is taken from [3]. The result for the cross-section is given in [3]:

$$\boxed{\sigma_{Rc}(E) = \frac{8\pi M^2}{3\hbar^4}\int_0^{\infty} b^3\left|\int_{R_0}^{\infty}\frac{\gamma(R)}{\sqrt{1-b^2/R^2-V_{\rm mol}(R)/E}}dR\right|^2 db}. \tag{C.26}$$

C.3 Quantum mechanical treatment

At low temperatures we expect the semiclassical treatment above to fail. This is because the behavior of the He atom within the centrifugal barrier becomes important. Fortunately we can use most of the results up to §C.2.1 to perform the fully quantum mechanical calculation. There are two salient differences in this calculation. First, we shall no longer take $\vec{\mathbf{N}}$ from a classical parameter, but treat it as a quantum operator. Second,

the motion of the He atom will no longer be determined from the classical Hamiltonian in (C.20), but will be obtained by solving a Schrödinger equation.

By treating the He atom quantum mechanically, we can also determine the elastic scattering cross-section from $V_{\rm mol}(\vec{R})$. This will allow us to predict the ratio of transport to inelastic scattering cross-sections.

To calculate either the elastic or relaxation cross-sections, we must calculate the wavefunctions of the He atom in the scattering potential $V_{\rm mol}$. Let $|\Psi\rangle$ represent the wavefunction of the He atom. Like the electronic wavefunction, it is separable into a radial and an angular component:

$$\Psi(R,\theta,\phi) = \mathscr{R}_N(E;R)Y_N^{m_N}(\theta,\phi). \tag{C.27}$$

The angular components $Y_N^{m_N}$ are again the standard spherical harmonics. The radial part $\mathscr{R}_N(E;R)$ is obtained by integrating the radial Schrödinger equation, (C.8), with $V_{\rm mol}(R)$ as the potential. For positive energies, there is a continuum of solutions to the radial Schrödinger equation. We can therefore find $\mathscr{R}_N(E;R)$ at any energy by solving the Schrödinger equation numerically. To perform this numerical solution, we start at some R_i deep within the energetically forbidden region (where $V_{\rm mol}(R) \gg E$). We choose the following initial values for the radial wavefunction: the wavefunction is set to 0 at R_i and its first derivative is set to unity. We then use an adaptive Runge-Kutta routine to solve $\mathscr{R}$ out to large R. The normalization is somewhat arbitrary, as the wavefunction oscillates out to infinity. Fortunately, we will not need the normalized wavefunction in order to calculate scattering cross-sections, as these cross-sections are always calculated from wavefunction ratios. An example of this calculation, for 1 K Ag-He with $N = 2$, is depicted in Fig. C.4.

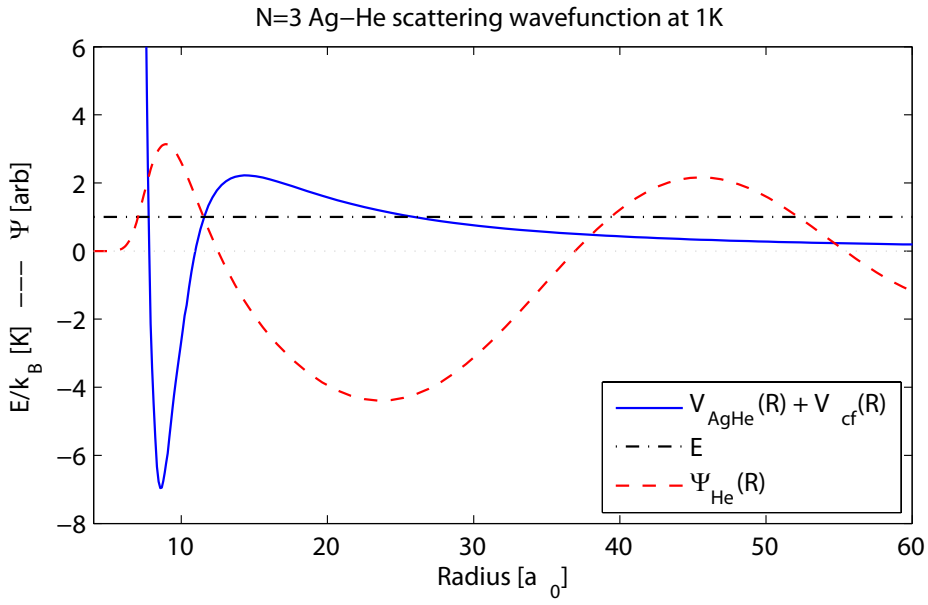

Figure C.4: An example calculation of the ^{3}He wavefunction in the Ag-He potential [98]. Here we have chosen $E = 1$ K and $N = 3$. The real component of the wavefunction is plotted versus He radius. The Ag nucleus position is fixed at the origin.

C.3.1 Relaxation cross-section

To find the probability of a spin-flip in this fully quantum mechanical treatment, we will again follow the evolution of the wavefunction, as we did in §C.2.1. However, we may no longer take the trajectory of the He atom from classical mechanics. In taking R as a parameter, we shall let the amount of time the He atom spends in a range R_1 to R_2 be proportional to the integrated probability for the He atom to be located in that same range. At R far away from the scattering center, this time must match the classical time the atom spends in this range, which is given by the atom velocity $v = \sqrt{2E/M}$.

At large R the classical time T spent in a range R_1 to R_2 is

$$T_{\text{classical}}(R_1, R_2) = \frac{|R_1 - R_2|}{\sqrt{2E/M}}. \tag{C.28}$$

In the quantum calculation, T is proportional to the integrated probability to find the He

atom in this range:

$$T(R_1, R_2) = \xi \int_{R_1}^{R_2} |\mathscr{R}_N(E;R)|^2 R^2 \; dR. \tag{C.29}$$

Here ξ is an unknown constant of proportionality. We can find T at large R simply by writing down the He wavefunction far from the scattering center [51]:

$$\mathscr{R}(R) \sim A_N \frac{e^{ikR}}{R} + B_N \frac{e^{-ikR}}{R}. \tag{C.30}$$

Note that $|A_N|^2 + |B_N|^2$ is the wavefunction normalization. $\hbar k = \sqrt{2EM}$ is the He momentum. At large R, the classical expression for T in (C.28) should agree with the quantum calculation of T in (C.29). We can use this to solve for ξ:

$$\frac{|R_1 - R_2|}{\sqrt{2E/M}} = \xi \int_{R_1}^{R_2} \left| A_N \frac{e^{ikR}}{R} + B_N \frac{e^{-ikR}}{R} \right|^2 R^2 \; dR. \tag{C.31}$$

If the range R_1 to R_2 covers many wavefunction oscillations, the oscillating components of the integrand may be ignored, and we have

$$\xi = \sqrt{\frac{M}{2E}} \; \frac{1}{|A_N|^2 + |B_N|^2}. \tag{C.32}$$

We now have a quantum mechanical expression for T, valid at all R. We use this expression for T to change variables from t to R in (C.24). When we do this, we must include dT/dR in our integral equation for the spin-flip probability. After changing variables we have:

$$\alpha(\infty) = -\frac{i\langle N_+ \rangle}{\hbar} \sqrt{\frac{M}{2E}} \int_0^\infty \gamma(R) \; \frac{|\mathscr{R}_N(E;R)|^2}{|A_N|^2 + |B_N|^2} \; R^2 dR. \tag{C.33}$$

Note that the normalization of $\mathscr{R}$ cancels in the equation for α. Also, this equation reduces to (C.24) when the integral is performed only over large R.

To obtain the relaxation cross-section, we sum the spin flip probability over all N. In expanding the incoming He plane wave in spherical harmonics, we obtain a prefactor of

$(2N+1)^2 P_N(\cos\theta)/k$ for each N, where P_N is the Nth Legendre polynomial [51, p. 234]. After integrating over all outgoing He angles, we have

$$\boxed{\sigma_R(E) = \frac{2\pi}{3E^2} \sum_{N=0}^{\infty} N(N+1)(2N+1) \left| \int_0^{\infty} \gamma(R) \, \frac{|\mathscr{R}_N(E;R)|^2}{|A_N|^2 + |B_N|^2} \, R^2 dR \right|^2}. \qquad \text{(C.34)}$$

Note that this expression agrees with (C.26) up to a factor of 2, if we perform the integrals only over large R, and we take the classical approximations $\hbar N \rightarrow mvb$ and $1/k \rightarrow db$ (cf. [51, p. 235]).

C.3.2 Transport cross-section

Once we have the He wavefunction, we may also readily calculate the elastic scattering cross-section. This is covered in almost any quantum mechanics text, so I will only describe the procedure briefly here. The cross-section is determined by comparing the He wavefunction to the asymptotic form of the wavefunction at large R, where $V_{\text{mol}} \rightarrow 0$. We can rearrange the asymptotic form (C.30), and write

$$\mathscr{R} \sim A_N \frac{\sin(kR - N\pi/2)}{R} + B_N \frac{\cos(kR - N\pi/2)}{R}. \qquad \text{(C.35)}$$

In the absence of any scattering, A_N is finite and $B_N = 0$. The scattering induces a phase shift of the free space sine wave, such that $B_N \neq 0$. This phase shift δ_N determines the degree of elastic scattering. The phase shift is [51]:

$$\tan\delta_N = -B_N/A_N. \qquad \text{(C.36)}$$

In the limit of no scattering, δ_N will be an integer multiple of π. δ_N is extracted from the wavefunction by simply comparing the value of the wavefunction at a node of the sin wave with the value at a node of the cosine wave:

$$\tan\delta_N = -\frac{\mathscr{R}\big(\pi(n + N/2)/k\big)}{\mathscr{R}\big(\pi(n + 1/2 + N/2)/k\big)} \qquad \text{(C.37)}$$

Here n is some large integer, such that $\pi n/k$ is far from the scattering well. Note that the normalization of $\mathscr{R}$ drops out in the ratio.

The transport cross-section σ_D is calculated from the phase shift δ_N [51, 70, 113]:

$$\boxed{\sigma_D(E) = \frac{2\pi\hbar^2}{ME}\sum_N (2N+1)\sin^2\left(\delta_{N+1}(E) - \delta_N(E)\right)}. \tag{C.38}$$

The transport cross-section discounts small angle scattering, and is the appropriate cross-section for calculation of transport phenomena; e.g. diffusion lifetimes. It can be compared with the total elastic cross-section, which is the cross-section for scattering into any angle.

$$\sigma_E(E) = \frac{2\pi\hbar^2}{ME}\sum_N (2N+1)\sin^2\delta_N(E). \tag{C.39}$$

In the s-wave scattering limit, all scattering is isotropic, and the transport and total elastic cross-sections are identical. In fact, if only one partial wave is involved in scattering at an energy E (that is, $\delta_N(E)$ is a multiple of π for all but one N), the two cross-sections will always be identical.

If multiple partial waves contribute to the scattering, the scattering will be biased toward small-angle scattering, and the diffusion cross-section will grow small compared to the total elastic cross-section. In the somewhat contrived case where n_N consecutive partial waves contribute and all $\delta_N(E)$ for these waves are identical, the ratio of total elastic to diffusion cross-sections is less than n_N. Note that in the energy ranges dealt with in buffer gas cooling experiments, only at most a few partial waves will contribute, and usually the transport cross-section will be within a factor of unity of the total elastic cross-section.

C.4 Thermally averaged cross-sections

To obtain the scattering cross-section for a thermal distribution of atoms, we average the inelastic scattering *rates*, with scattering energies distributed according to the

Maxwell-Boltzmann distribution. The thermally averaged cross-section is [66]

$$\boxed{\bar{\sigma}(T) = \frac{1}{(k_B T)^2} \int E\, \sigma(E) e^{-E/k_B T} dE}. \tag{C.40}$$

An important feature of (C.40) is that the thermal average preserves power laws. That is, if $\sigma(E) \sim E^a$, then we find $\bar{\sigma}(T) \sim T^a$.

We may also ask what form (C.40) takes when $\sigma(E)$ is a δ-function. This is approximately the case when we have a scattering resonance, as long as the width of the scattering resonance ΔE is much smaller than the width of the thermal distribution. The δ-function approximation gives a thermally averaged cross-section of $\bar{\sigma}(T) \sim (1/k_b T)^2 \exp(-E_0/k_B T)$, where E_0 is the resonance energy, with the expression holding for $T \gg \Delta E$. For small T, then, we can see exponential increases in $\bar{\sigma}(T)$. However, for large T, we will always see a temperature dependence weaker than T^{-2}. This behavior is confirmed by numerical integration of a scattering resonance. In the location of a resonance, $\sigma(E)$ is represented by the Breit-Wigner function [51]:

$$\sigma(E) \sim \frac{1}{E} \frac{\Delta E^2}{4(E - E_0)^2 + \Delta E^2}. \tag{C.41}$$

We substitute this expression into (C.40) and integrate numerically. The result is shown in Fig. C.5, confirming the analytic analysis here.

C.5 Results

To make a prediction for the Ag-He spin-relaxation scattering cross-section, I first calculated γ_a out to $R = 400\, a_0$. The result of this calculation is depicted in Fig. C.3. Next, using the AgHe potentials found in [98], I calculated Ψ_{He} for this same range, for E/k_B between 20 mK and 2 K, and for all N up to 6. Using these scattering potentials gives a scattering resonance for $N = 5$ at $E/k_B = 800$ mK. Beyond $N = 6$, the low-energy elastic

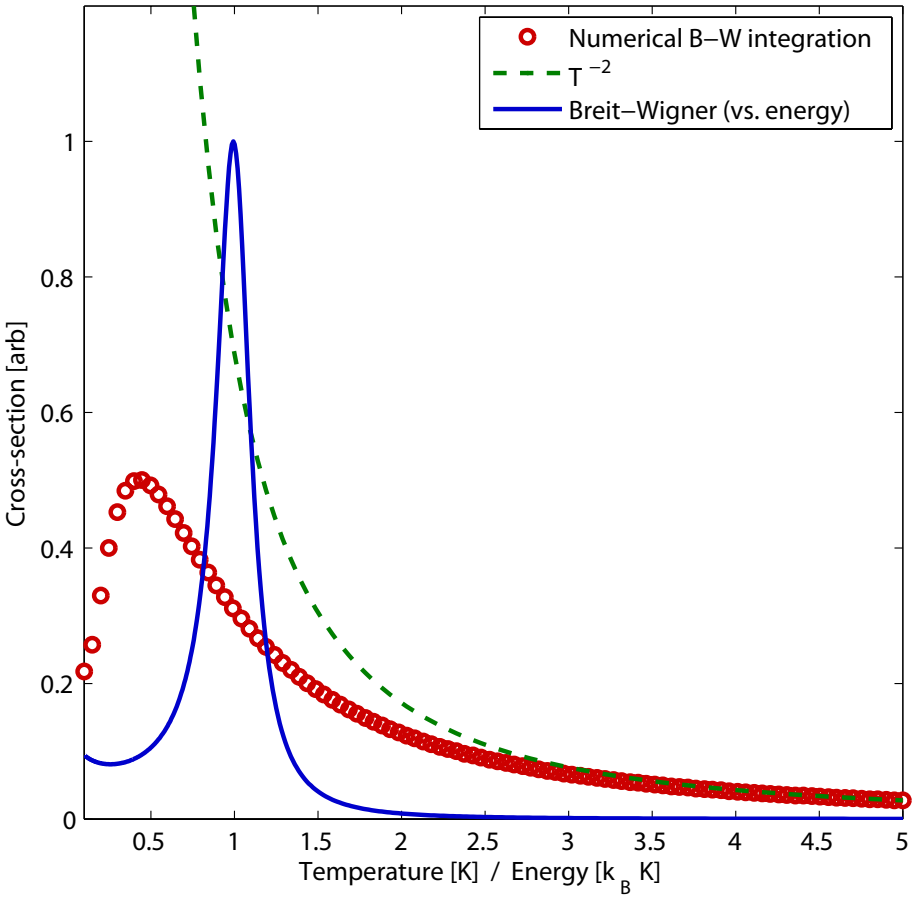

Figure C.5: Thermal average of the Breit-Wigner cross-section. The thermally averaged cross-section $\bar{\sigma}(T)$ is plotted vs. temperature in the red circles. The dashed green line shows the limiting T^{-2} high temperature law, and the solid blue line depicts $\sigma(E)$, plotted vs. energy.

scattering behavior becomes inaccurate. This is because the low-energy term is determined by dividing two terms very close to 0 ($\sin^2 \delta_N / k^2$). As N becomes large, small errors in δ_N at low energies create large errors in the scattering cross-sections.

Elastic cross-sections were calculated using (C.39) and relaxation cross-sections were calculated from (C.34). Each cross-section was then thermally averaged, for temperatures between 200 mK and 700 mK. The ratio is plotted in Fig. C.6. Note that if the scattering resonance in the $N = 5$ scattering channel is removed, we find a cross-section ratio of $\sim 10^9$, decreasing linearly with temperature.

It is worth noting that the location of scattering resonances can be very sensitive to details of the scattering potentials. We have no reason to believe our Ag-He scattering potential is at all precise enough to accurately predict scattering resonances. In fact, because the potential was pulled from a rather coarse plot, significant errors are almost guaranteed. It is perhaps more useful to note that two behaviors are possible: the 10^9 linearly decreasing scattering ratio in the absence of a resonance, and a cross-section ratio behaving in a manner only generally similar to the behavior calculated using the Takami Ag-He potentials. Note that we expect power law behaviors stemming from a resonance to agree with our calculated behavior. Where our prediction might fail is in predicting the magnitude of resonance behavior and the position of the cross-section maximum.

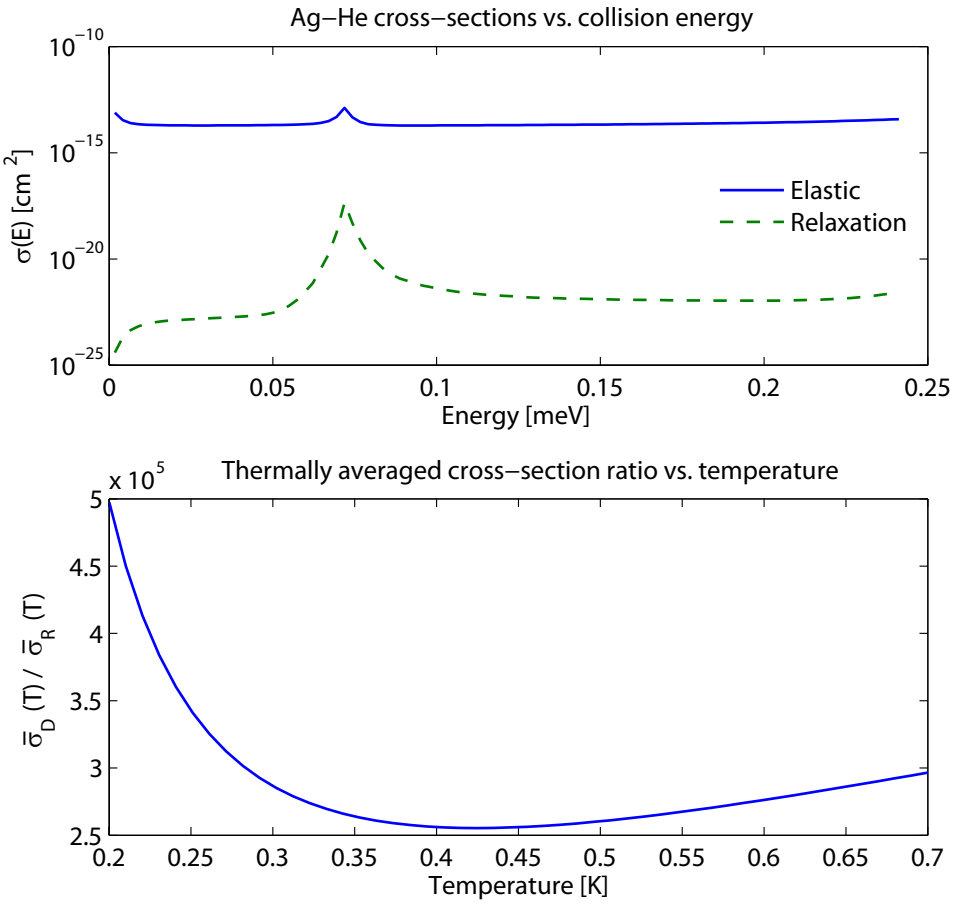

Figure C.6: The upper plot shows calculated elastic and spin-relaxation cross-sections for Ag-^{3}He. Note the prominent scattering resonance at 0.07 meV. The magnitude and thermal dependence of the thermally averaged cross-section ratio, depicted in the lower plot, is due entirely to this resonance. If it is removed, we find a cross-section ratio $\sim 10^9$, decreasing linearly with temperature.

Bibliography

[1] R. deCarvalho, N. Brahms, B. Newman, J. M. Doyle, D. Kleppner, and T. Greytak, Can. J. Phys. **83**, 293 (2005).

[2] N. Brahms, B. Newman, C. Johnson, T. Greytak, D. Kleppner, and J. Doyle, arXiv:0804.0766v1 [physics.atom-ph].

[3] T. G. Walker, J. Thywissen, and W. Happer, Phys. Rev. A **56**, 2090 (1997).

[4] A. L. Migdall, J. V. Prodan, W. D. Phillips, T. H. Bergeman, and H. J. Metcalf, Phys. Rev. Lett. **54**, 2596 (1985).

[5] D. E. Pritchard, Phys. Rev. Lett. **51**, 1336 (1983).

[6] C. V. Heer, Rev. Sci. Instrum. **34**, 532 (1963).

[7] M. H. Anderson, J. R. Ensher, M. R. Matthews, C. E. Wieman, and E. A. Cornell, Science **269**, 198 (1995).

[8] C. C. Bradley, C. A. Sackett, J. J. Tollett, and R. G. Hulet, Phys. Rev. Lett. **75**, 1687 (1995).

[9] D. G. Fried, T. C. Killian, L. Willmann, D. Landhuis, S. C. Moss, D. Kleppner, and T. J. Greytak, Phys. Rev. Lett. **81**, 3811 (1998).

[10] B. DeMarco and D. S. Jin, Science **285**, 1703 (1999).

[11] R. Onofrio, C. Raman, J. M. Vogels, J. R. Abo-Shaeer, A. P. Chikkatur, and W. Ketterle, Phys. Rev. Lett. **85**, 2228 (2000).

[12] S. Jochim, M. Bartenstein, A. Altmeyer, G. Hendl, S. Riedl, C. Chin, J. H. Denschlag, and R. Grimm, Science **302**, 2101 (2003).

[13] M. W. Zwierlein, C. A. Stan, C. H. Schunck, S. M. F. Raupach, S. Gupta, Z. Hadzibabic, and W. Ketterle, Phys. Rev. Lett. **91**, 250401 (2003).

[14] M. Greiner, O. Mandel, T. Esslinger, T. W. H. ansch, and I. Bloch, Nature **415**, 39 (2002).

[15] D. Jaksch, C. Bruder, J. I. Cirac, C. W. Gardiner, and P. Zoller, Phys. Rev. Lett. **81**, 3108 (1998).

[16] T. Zelevinsky, M. M. Boyd, A. D. Ludlow, S. M. Foreman, S. Blatt, T. Ido, and J. Ye, Hyperfine Interactions **174**, 55 (2007).

[17] L. V. Hau, S. E. Harris, Z. Dutton, and C. H. Behroozi, Nature **397**, 594 (1998).

[18] K. R. Hansen and K. Mølmer, Phys. Rev. A **75**, 065804 (2007).

[19] C. Liu, Z. Dutton, C. H. Behroozi, and L. V. Hau, Nature **409**, 490 (2001).

[20] J. G. E. Harris, W. C. Campbell, D. Egorov, S. E. Maxwell, R. A. Michniak, S. V. Nguyen, L. D. van Buuren, and J. M. Doyle, Rev. Sci. Inst. **75**, 17 (2004).

[21] R. deCarvalho, J. M. Doyle, B. Friedrich, T. Guillet, J. Kim, D. Patterson, and J. D. Weinstein, Eur. Phys. J. D **7**, 289 (1999).

[22] H. L. Bethlem, A. J. A. van Roij, R. T. Jongma, and G. Meijer, Phys. Rev. Lett. **88**, 133003 (2002).

[23] T. W. Hänsch and A. L. Schawlow, Opt. Commun. **13**, 68 (1975).

[24] W. M. Itano and D. J. Wineland, Phys. Rev. A **25**, 35 (1982).

[25] H. J. Metcalf and P. van der Straten, *Laser Cooling and Trapping* (Springer, 1999).

[26] A. S. Bell, J. Stuhler, S. Locher, S. H. J. Mlynek, and T. Pfau, Europhys. Lett. **45**, 156 (1999).

[27] J. M. Doyle, B. Friedrich, J. Kim, and D. Patterson, Phys. Rev. A **52**, R2515 (1995).

[28] C. I. Hancox, S. C. Doret, M. T. Hummon, L. Luo, and J. M. Doyle, Nature (London) **431**, 281 (2004).

[29] J. D. Weinstein, R. deCarvalho, T. Guillet, B. Friedrich, and J. M. Doyle, Nature **395**, 148 (1998).

[30] J. D. Weinstein, R. deCarvalho, J. Kim, D. Patterson, B. Friedrich, and J. M. Doyle, Phys. Rev. A **57**, R3173 (1998).

[31] J. Kim, B. Friedrich, D. P. Katz, D. Patterson, J. D. Weinstein, R. DeCarvalho, and J. M. Doyle, Phys. Rev. Lett. **78**, 3665 (1997).

[32] S. V. Nguyen, S. C. Doret, C. B. Connolly, R. A. Michniak, W. Ketterle, and J. M. Doyle, Phys. Rev. A **72**, 060703 (2005), URL `http://link.aps.org/abstract/PRA/v72/e060703`.

[33] C. I. Hancox, M. T. Hummon, S. V. Nguyen, and J. M. Doyle, Phys. Rev. A **71**, 031402 (2005), URL `http://link.aps.org/abstract/PRA/v71/e031402`.

[34] M. T. Hummon, W. C. Campbell, H.-I. Lu, E. Tsikata, Y. Wang, and J. M. Doyle (2008), URL `http://arxiv.org/abs/0802.1662`.

[35] W. C. Campbell, E. Tsikata, H.-I. Lu, L. D. van Buuren, and J. M. Doyle, Phys. Rev. Lett. **98**, 213001 (2007), URL `http://link.aps.org/abstract/PRL/v98/e213001`.

[36] H. E. Hess, Phys. Rev. B **34**, 3476 (1986).

[37] Y. Ralchenko, F.-C. Jou, D. E. Kelleher, A. E. Kramida, A. Musgrove, J. Reader, W. L. Wiese, and K. Olsen, *NIST atomic spectra database* (version 3.1.2), [Online] (2007), URL `http://physics.nist.gov/asd3`.

[38] M. G. Boshier, P. E. G. Baird, C. J. Foot, E. A. Hinds, M. D. Plimmer, D. N. Stacey, J. B. Swan, D. A. Tate, D. M. Warrington, and G. K. Woodgate, Nature **330**, 463 (1987), URL `http://dx.doi.org/10.1038/330463a0`.

[39] H. F. Hess, G. P. Kochanski, J. M. Doyle, N. Masuhara, D. Kleppner, and T. J. Greytak, Phys. Rev. Lett. **59**, 672 (1987).

[40] J. K. Steinberger, Ph.D. thesis, MIT (2004).

[41] A. Huber, T. Udem, B. Gross, J. Reichert, M. Kourogi, K. Pachucki, M. Weitz, and T. W. Hänsch, Phys. Rev. Lett. **80**, 468 (1998).

[42] R. G. H. Robertson, T. J. Bowles, G. J. Stephenson, D. L. Wark, J. F. Wilkerson, and D. A. Knapp, Phys. Rev. Lett. **67**, 957 (1991).

[43] T. Badr, M. D. Plimmer, P. Juncar, and M. E. Himbert, Phys. Rev. A **74**, 062509 (2006).

[44] M. B. Gaarde, R. Zerne, L. Caiyan, J. Zhankui, and J. L. ans S. Svanberg, Phys. Rev. A **50**, 209 (1994).

[45] G. Uhlenberg, J. Dirscherl, and H. Walther, Phys. Rev. A **62**, 063404 (2000).

[46] J. Cubizolles, T. Bourdel, S. J. J. M. F. Kokkelmans, G. V. Shlyapnikov, and C. Salomon, Phys. Rev. Lett. **91**, 240401 (2003).

[47] A. J. Kerman, J. M. Sage, S. Sainis, T. Bergeman, and D. DeMille, Phys. Rev. Lett. **92**, 033004 (2004).

[48] W. Campbell, Ph.D. thesis, Harvard (2008).

[49] J. Kim, Ph.D. thesis, Harvard (1997).

[50] S. J. Maxwell, Ph.D. thesis, Harvard (2007).

[51] E. Merzbacher, *Quantum Mechanics* (J. Wiley & Sons, 1970), 2nd ed.

[52] F. Pobell, *Matter and Methods at Low Temperatures* (Springer, 1996), 2nd ed.

[53] E. R. Grilly, Cryogenics **2**, 226 (1962).

[54] Y. H. Huang and G. B. Chen, Cryogenics **46**, 833 (2006).

[55] S. Maxwell, N. Brahms, R. deCarvalho, D. Glenn, J. Helton, S. Nguyen, D. Patterson, J. Petricka, D. DeMille, and J. Doyle, Phys. Rev. Lett. **95**, 173201 (2005).

[56] T. V. Tscherbul and R. V. Krems, Physical Review Letters **97**, 083201 (2006), URL `http://link.aps.org/abstract/PRL/v97/e083201`.

[57] J. D. Weinstein, Ph.D. thesis, Harvard (2001).

[58] R. Michniak, Ph.D. thesis, Harvard (2004).

[59] W. Ketterle, D. S. Durfee, and D. M. Stamper-Kurn, in *Proceedings of the 1998 Enrico Fermi Summer School* (1998).

[60] C. Johnson, Ph.D. thesis, MIT (2008).

[61] R. deCarvalho, Ph.D. thesis, Harvard (2003).

[62] W. Ketterle and N. Druten, in *Advances in Atomic, Molecular and Optical Physics*, edited by B. Bederson and H. Walther (Elsevier, 1996), vol. 37, pp. 181–236.

[63] R. Chapman, Phys. Rev. A **12**, 2333 (1975).

[64] R. V. Krems and A. A. Buchachenko, J. Chem. Phys. **123**, 101101 (2005).

[65] N. W. Ashcroft and N. D. Mermin, *Solid State Physics* (Harcourt Brace, 1976).

[66] J. B. Hasted, *Physics of Atomic Collisions* (Butterworth, 1972).

[67] M. Abramowitz and I. Stegun, *Handbook of Mathematical Functions* (Dover, 1965), 9th ed.

[68] F. A. Franz, Phys. Rev. **139**, A603 (1965).

[69] E. R. I. Abraham, W. I. McAlexander, C. A. Sackett, and R. G. Hulet, Phys. Rev. Lett. **74**, 1315 (1995).

[70] A. Dalgarno, private communication.

[71] B. Newman, Ph.D. thesis, MIT (2008).

[72] A. Roth, *Vacuum Technology* (North Holland, 1990), 3rd ed.

[73] J. M. Gerton, C. A. Sackett, B. J. Frew, and R. G. Hulet, Phys. Rev. A **59**, 1514 (1995).

[74] R. Côté, M. J. Jamieson, Z.-C. Yan, N. Geum, G.-H. Jeung, and A. Dalgarno, Phys. Rev. Lett. **84**, 2806 (2000).

[75] Wolfgang Demtröder, *Absorption Spectroscopy* (Springer, 2002), 3rd ed.

[76] New Focus, 2584 Junction Avenue, San Jose, CA 95134, URL `http://www.newfocus.com`.

[77] Optics for Research, Inc., PO Box 82, Caldwell, NJ 07006, URL `http://www.ofr.com`.

[78] Coherent, Inc., 5100 Patrick Henry Drive, Santa Clara, CA 95054, URL `http://www.coherent.com`.

[79] Hamamatsu Corp., 360 Foothill Rd, Bridgewater, NJ 08807, URL `http://sales.hamamatsu.com`.

[80] C. J. Sansonetti, B. Richou, R. Engleman, and L. J. Radziemski, Phys. Rev. A **52**, 2682 (1995).

[81] Oxford Instruments, 300 Baker Avenue, Suite 150, Concord, MA 01742, URL `http://www.oxford-instruments.com`.

[82] American Magnetics, Inc., Oak Ridge, TN 37830, URL `http://www.americanmagnetics.com`.

[83] 3150 Central Expressway, Santa Clara, CA 95051, URL `http://www.continuumlasers.com`.

[84] D. W. Sedgley, A. G. Tobin, T. H. Batzer, and W. R. Call, J. Vac. Sci. Technol. A **5**, 2572 (1987).

[85] T. J. Glover, *Pocket Ref* (Sequoia Publishing Co., 2002).

[86] Janis Research Co., 2 Jewel Drive, Wilmington, MA 01887, URL `http://www.janis.com`.

[87] S. Nguyen, Ph.D. thesis, Harvard (2006).

[88] P. L. Bender, J. L. Hall, R. H. Garstang, F. M. J. Pichanik, W. W. Smith, R. L. Barger, and J. B. West, Bull. Am. Phys. Soc. **21**, 599 (1976).

[89] R. V. Krems, J. Klos, M. F. Rode, M. M. Szczesniak, G. Chalasinski, and A. Dalgarno, Phys. Rev. Lett. **94**, 013202 (2005).

[90] C. I. Hancox, S. C. Doret, M. T. Hummon, R. V. Krems, and J. M. Doyle, Phys. Rev. Lett. **94**, 013201 (2005).

[91] A. O. Sushkov and D. Budker, Phys. Rev. A **77**, 042707 (2008).

[92] H. Dahmen and S. Penselin, Z. Phys. A **200**, 456 (1967).

[93] G. Wessel and H. Lew, Phys. Rev. **92**, 641 (1953).

[94] S. Song, G. Wang, A. Ye, and G. Jian, J. Phys. B **40**, 475 (2007).

[95] L. Cai, B. Friedrich, and J. M. Doyle, Phys. Rev. A **61**, 033412 (2000).

[96] R. M. Herman, Phys. Rev. **136**, A1576 (1964).

[97] Z. Wu, T. G. Walker, and W. Happer, Phys. Rev. Lett **54**, 1921 (1985).

[98] Z. J. Jakubek and M. Takami, Chem. Phys. Lett. **265**, 653 (1997).

[99] E. Fermi, Nuovo Cimento **11**, 157 (1934).

[100] B. E. Sauer, J. Wang, and E. A. Hinds, Phys. Rev. Lett. **74**, 1554 (1995).

[101] L. Cai, B. Friedrich, and J. Doyle, Physical Review A **61**, 033412 (2000).

[102] N. Ramsey, *Molecular Beams* (Oxford Science Publications, 1985), paperback ed.

[103] R. Telfer, URL `http://www.pha.jhu.edu/ rt19/hydro/node9.html`.

[104] C. Cohen-Tannoudji, J. Dupont-Roc, and G. Grynberg, *Atom-Photon Interactions; Basic Processes and Applications* (Wiley, 1992).

[105] R. D. Cowan, *Theory of Atomic Structure and Spectra* (University of California Press, 1981).

[106] The MathWorks, Inc., 3 Apple Hill Drive, Natick, MA 01760, URL `http://www.mathworks.com`.

[107] Southern Spring Mfg., Inc., 915 Pinemont, Houston, TX 77018, URL `http://www.southernspring.net/`.

[108] The Barden Corporation, FAG Aerospace and Super Precision Division, 200 Park Avenue, Danbury, CT USA 06813, URL `http://www.bardenbearings.com/`.

[109] W. Happer, Rev. Mod. Phys. **44**, 169 (1972).

[110] E. Roueff, Astron. Astrophys. **7**, 4 (1970).

[111] E. Clementi and C. Roetti, Atom. Data Nucl. Data Tables **14**, 177 (1974).

[112] M. J. Seaton, Proc. Royal Astron. Soc. **118**, 504 (1958).

[113] A. Arthurs and A. Dalgarno, Proc. R. Soc. A **256**, 540 (1960).

Glossary of Symbols

C_{seal}	Conductance of a vacuum seal . . . 132
$\overline{dE}$	Elastic energy transfer, averaged over collision angles . . . 8
E	Collision energy . . . 152
f	Fine structure coefficient . . . 109
f_b	Fraction of orbits in the Maxwell-Boltzmann distribution that are lost from the trap . . . 23
f_j	Energy shift of state j . . . 108
D	Diffusion constant . . . 27
g	2-body loss coefficient . . . 13
g_{cyl}	Geometry factor for diffusion in a cylinder . . . 28
g_J	Landé g-factor . . . 14
G_p	Generalized loss coefficient . . . 13
$\mathscr{H}$	Atomic Hamiltonian . . . 107
i	Nuclear spin quantum number . . . –
$\vec{\mathbf{I}}$	Nuclear spin . . . –
I	Probe beam intensity . . . 122
I_0	Incident probe intensity . . . 122
k_B	Boltzmann constant . . . –
j	Total electronic angular momentum quantum number . . . –
$\vec{\mathbf{J}}$	Total electronic angular momentum . . . –
l	Orbital angular momentum quantum number . . . –
$\vec{\mathbf{L}}$	Orbital angular momentum . . . –
m	Background gas mass . . . 23
	in App. C, electron mass . . . 146
m_J	Projection of total electronic angular momentum, typically along $\vec{B}$ . . . 14
m_{LFS}	Most low-field seeking m_J level . . . 32
M	Trapped atom mass . . . 23
	in App. C, reduced mass of the collision system . . . 145
n	Local atom density . . . 13
n_0	Atom density at $\vec{r} = \vec{0}$ . . . 15
n_b	Local background gas density . . . 17
N	Total trapped atom number . . . 13
	also, molecular rotation quantum number . . . 145
$\vec{\mathbf{N}}$	Molecular rotation angular momentum . . . 145
N_0	Total atom number at $t = 0$ . . . 16
OD	Optical density . . . 50, 116
P_{laser}	Probe laser power . . . 48
$\vec{r}$	Spatial coordinate . . . 13
r	Radial coordinate . . . –
R	Radial distance from the trap center to the nearest evaporation surface . . . 15
	also, internuclear separation . . . 146
R_{cell}	Radius of the cell, typically $= R$ . . . 17
R_k	Atomic state distribution coefficient . . . 121
s	Electron spin quantum number . . . –

$\vec{\mathbf{S}}$	Electron spin	–
t	Time	–
t_{col}	Mean elastic atom-background gas collision time	26
t_{orbit}	Trap orbit period	21
T	Temperature (typically of the atom cloud)	15
T_b	Temperature of the background gas	23
T_{wall}	Cell wall temperature	41
U	Atom potential energy	14
U_{trap}	Trap depth	7
$\langle U \rangle$	Average atom potential energy	21
$\bar{v}_\mu$	Average collision velocity	23
$\bar{v}_b$	Thermal buffer gas velocity	39
v_{drift}	Diffusion drift velocity	27
V_a	Atomic potential	149
V_{cell}	Trapping cell volume	39
V_{mol}	Internuclear potential	154
V_p	p-body effective trap volume	15
w	Probe beam waist	122
Y_m^l	Spherical harmonic	148
z	Axial coordinate	–

Index